LONGPATH
TECHNOLOGIES

Supporting Documentation:

Publications and Reports

Request for Alternative Test Method

Methane Detection Technology

§60.5398b(b) Periodic Screening

The Environmental Protection Agency

Emission Measurement Center

https://www.epa.gov/emc/oil-and-gas-alternative-test-methods

LongPath Technologies

https://www.longpathtech.com

Table of Contents

Long Distance Continuous Methane Emissions Monitoring with Dual Frequency Comb Spectroscopy: deployment and blind testing in complex emissions scenarios

Authors:
Sean Coburn[1,*]; Caroline B. Alden[1,2]; Robert Wright[1], Griffith Wendland[1]; Alex Rybchuk[1]; Nicolas Seitz[1]; Ian Coddington[3]; and Gregory B. Rieker[1]

Affiliations:
[1]University of Colorado Boulder, Boulder, Colorado, USA
[2]Cooperative Institute for Research in Environmental Sciences, Boulder, Colorado, USA
[3]National Institute for Standard and Technology, Boulder, Colorado, USA
*Corresponding author: coburns@colorado.edu

Abstract
Continuous monitoring of oil and gas infrastructure is of interest for improving emissions and safety by enabling rapid identification and repair of emission sources, especially large sources that are responsible for the bulk of total emissions. We have previously demonstrated dual frequency comb spectroscopy coupled with atmospheric modeling and inversion techniques (the DCS Observing System) as a viable and accurate approach for detection, attribution and quantification of methane emissions at distances of more than 1 km under controlled, steady emissions scenarios. Here, we present the results of validation testing designed to mimic the complexity of operational well pad emissions from oil and gas production, and the first field measurements at an active oil and gas facility. The validation tests are performed single-blind (the measurement and data analysis team are not given information about the emissions) at the METEC test facility. They consist of a series of scenarios ranging from a single, steady-rate emission point to multiple emission points that include intermittent releases (the METEC "R2" tests). Additionally, we present field measurements at an active natural gas facility demonstrating that the system can remotely and autonomously monitor methane emissions in a true industrial setting. This field verification is in a configuration designed for continuous and long-term characterization of operational and fugitive emissions. These demonstrations confirm that the DCS Observing System can provide high-confidence continuous monitoring of emissions from complex, operational facilities among natural gas infrastructure.

Introduction
Methane is a potent greenhouse gas with a 20-year global warming potential (GWP) approximately 85 times greater than CO_2, and anthropogenic sources of methane contribute up to 65% of total global emissions [1]. Recent studies suggest that emissions from oil and gas production are higher than previously estimated, and demonstrate a "fat tail" distribution in which a relatively small number of large emitters contribute most of the overall methane loss to the atmosphere [2–5]. However, the variability of emissions in time is not well understood, which poses a challenge for both accurately assessing total emissions and understanding their associated safety and health risks. Emissions variability also introduces a challenge for differentiating process emissions (vents) and fugitive events (leaks), complicating efforts to find and fix large leaks efficiently. These gaps in our understanding and capabilities are due, in part, to limitations inherent to current detection technologies and approaches, which provide snapshot-in-time data, often on an infrequent basis. For example, current leak detection and repair

(LDAR) work practice involves costly site visits with handheld devices [6]. Truck-, aircraft- or drone-mounted sensors [7–13] can offer a faster alternative, but still cannot cost-effectively provide, continuous monitoring of infrastructure. Continuous monitoring would enable rapid find and fix capabilities for the largest emitters and is critical for accurate characterization of sector-wide emissions, given observed intermittency, unpredictability, and even seeming stochasticity in large emitters [14–16]. Fixed ground-based sensors hold the capability to enable continuous observations which would fill this critical information gap [17–26].

Dual frequency comb spectroscopy (DCS) in conjunction with atmospheric modeling and inversion methods (the DCS Observing System) provide accurate and continuous detection, attribution and quantification of methane emissions from oil and gas equipment [24–26], offering a promising solution to this problem. This spectrometer consists of a single, centralized DCS that samples the surrounding region via an optical transceiver that sends laser light over long, open atmospheric paths to an array of strategically positioned retroreflectors. This approach can provide continuous measurements of specific emissions sources across areas of 10 m^2 to 10 km^2 with a single instrument. The system operates autonomously, and due to its use of an active laser source, is capable of operation day and night in all temperatures and in all ground and sky cover conditions, except for dense falling snow, rain or fog. In addition, the large range of coverage offers the possibility for cost-effective deployment, since a single unit can observe many sites within a region. These characteristics together make for cost-effective continuous monitoring and rapid identification of emissions in operational scenarios and enable characterization of the time variability of emissions in fundamental studies.

Previous testing of the DCS Observing System at the Methane Emissions Technology Evaluation Test Center (METEC) demonstrated high-accuracy steady emission detection and characterization [25]. In a series of 18 single steady-leak tests (emission rates ranged from 0 to 10.7 g min^{-1} [0-34.7 scfh]), the DCS Observing System successfully identified all emissions and quantified emission rates to within 27% on average. However, limitations of that study for applicability of the system to "real-world" emission scenarios included the use of: 1) steady emission rates, whereas intermittent or episodic emissions are observed in oil and gas operational environments (e.g., liquid unloading events [27]), and 2) single point source emissions at a time, whereas at real oil and gas facilities many components have the potential to emit simultaneously. Here we validate the DCS Observing System's performance under time-varying and multi-point source emissions scenarios and demonstrate autonomous emission retrievals in a true industrial setting.

Validation was accomplished through a set of blind tests of complex "operational" emission scenarios. The validation tests were again conducted at the METEC facility using their "R2" protocol, which included emissions that vary with time and simultaneous emissions from multiple source locations. Additionally, the site and equipment being monitored during the tests were configured to more closely match modern upstream oil and natural gas facility layouts, in terms of the size of the monitored area, and the count and spacing of emission sources. We also present data collected at an operational natural gas storage facility during a transient emission event. These measurements represent the first set of results from a long-term study of this facility and demonstrate the capability and utility of the DCS Observing System in providing time-resolved emission measurements over extended periods of time.

Methods

Frequency combs are laser sources that emit a large number of discrete, evenly spaced, wavelengths (comb teeth), which can be used to measure the concentration of gases in the atmosphere. This is done by transmitting comb light across an open path and detecting the wavelength-dependent absorption fingerprints of the molecules present in the path. We use dual frequency comb spectroscopy (DCS), a technique in which two carefully prepared frequency combs are interfered on a single photodiode allowing for broadband, high-resolution spectroscopy with a simple detection scheme [28,29]. In the implementation here, the frequency combs are mode-locked erbium fiber lasers that are spectrally broadened and then optically filtered to 40 nm [~4.5 THz] to match the methane absorption fingerprint at 1.65 μm. The combs provide > 22 000 distinct spectral elements in this band at a very close 1.8 pm spacing. This enables trace gas spectroscopy over long pathlengths with high precision and stability [30,31]. The DCS used for this work has been engineered to support stable operation in field deployment [24,32].

To observe the surrounding environment, DCS light is fiber coupled to an optical telescope transceiver that launches the laser light over long atmospheric paths (typically several hundred meters to multiple kilometers) to a retroreflector, which returns the laser light back to the transceiver, where it is coupled onto a 150 MHz InGaAs photodetector. The transceiver is mounted on a gimbal that cycles the beam over multiple paths across a region, enabling the measurement of path-integrated methane concentrations over multiple-square-kilometer regions. The DCS observing system is configured such that each beam path is queried autonomously during active measurement periods. A more detailed description of the fielded DCS observing system can be found in [24,25].

To quantify emission sources the path-integrated methane concentration measurements are incorporated into an atmospheric model and inversion algorithm allowing determination of emission location and rate. The inversion model also incorporates local wind measurements collected by a 3D sonic anemometer as well as geospatial information including retroflector locations, the DCS location, and locations of potential sources. A gaussian plume model is used to create source-receptor relationships which are then fit to the measured methane concentrations using a least-squares-based inversion approach providing the emission location and rate. Further detail can be found in [26].

Blind validation testing under “operational” conditions

At the time of testing, the Methane Emissions Technology Evaluation Center (METEC), located in Fort Collins, CO (https://energy.colostate.edu/metec/), had recently upgraded their testing profile for more complex emissions meant to more accurately simulate realistic oil and gas operational conditions. This evaluation followed the “R2” testing procedure and consisted of 15 single-blind emission scenarios administered by METEC (each lasting ~4 hours resulting in 2 tests/day) in three “difficulty” categories:

- **Difficulty A:** Single steady emission (6 tests)
- **Difficulty B:** Multiple steady emissions (6 tests)
- **Difficulty C:** Multiple emissions that may be steady or intermittent, i.e. the rate is variable in time (3 tests)

All emission points for these tests originate from a 50 m × 60 m mock production pad containing three equipment batteries (a battery of 5 wellheads, a battery of 4 separators, and a battery of 3 tanks – where "battery" is defined here as an equipment grouping of the same type). Figure 1 shows an overhead view of the emission test site relative to the DCS location > 1 km away at the Colorado State University Foothills campus (panel a) and a more detailed view of the METEC site contained within the inset.

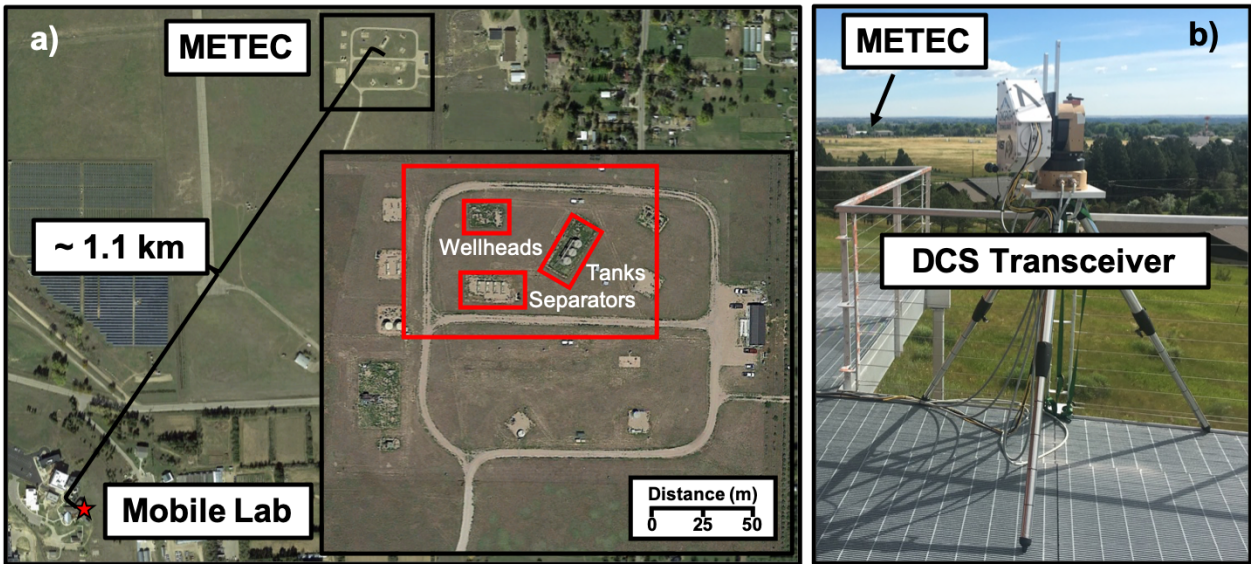

Figure 1: Overview of the METEC test site and the DCS sampling location (panel a) and a photo of the DCS transceiver (panel b). Panel a) the red star indicates the position of the DCS at the foothills campus of Colorado State University, which is ~1.1 km away from the METEC site. The inset includes a closer view of METEC, with the red squares highlighting the different potential source regions: 1) a battery of 5 wellheads; 2) a battery of 4 separators; and 3) a battery of 3 tanks. Panel b) contains a picture of the DCS transceiver with the METEC site noted in the background. The larger red square in the inset corresponds with the region shown in figure S1. panel a.

In the results presented here, we distinguish between the values measured by the DCS system in single-blind testing as "measured" and the values controlled by METEC as "true". For each test, we describe our success in emissions characterization in terms of detection, attribution and quantification. First, we report our success in estimating the presence and absence of emissions at each battery (detection). Second, we report our success in attributing detected emissions to the battery level (and not, for example, to individual pieces of equipment). For inversion results where > 1 emission point is detected at a given battery, the rates are summed and the average location is reported (noted in figure 2 with the cross symbol). To aid in comparison of measured with true results, we treat true results in the same way (i.e., the locations for multiple emissions from a single battery are summed and noted in figure 2 with an asterisk symbol). Finally, we report our success in estimating the emission rate for each battery (quantification), following the steps above in cases of multiple emissions. For intermittent emission profiles, the true average emission rate is calculated following Eq. 1.

$$Rate_{avg} = Rate_{cal} * (\frac{t_{on}}{t_{total}}) \quad \text{(Eq. 1)}$$

Where $Rate_{cal}$ is the flow rate as measured by METEC operators during a calibration period conducted prior to each test, t_{on} is the total time the emission is active, and t_{total} is the total test duration.

Figure 2 is a graphical table overview of the testing results with respect to detection and attribution. In all, the system successfully detects 22 of the 25 individual emission events (dark green) from a distance > 1 km with 3 missed emissions (orange) and 6 false positives (red) - all of which were below 1.65 g min^{-1} (5 standard cubic feet per hour [scfh]). In this figure, emissions are grouped by battery along the y-axis and in increasing emission strength (from any battery for each test) along the x-axis. Additionally, the black dots indicate a test/battery combination that did not have any emissions and was correctly identified as such. A more detailed overview of the results from one of the tests (Test ID #10 from figure 2) is presented in the supplementary information.

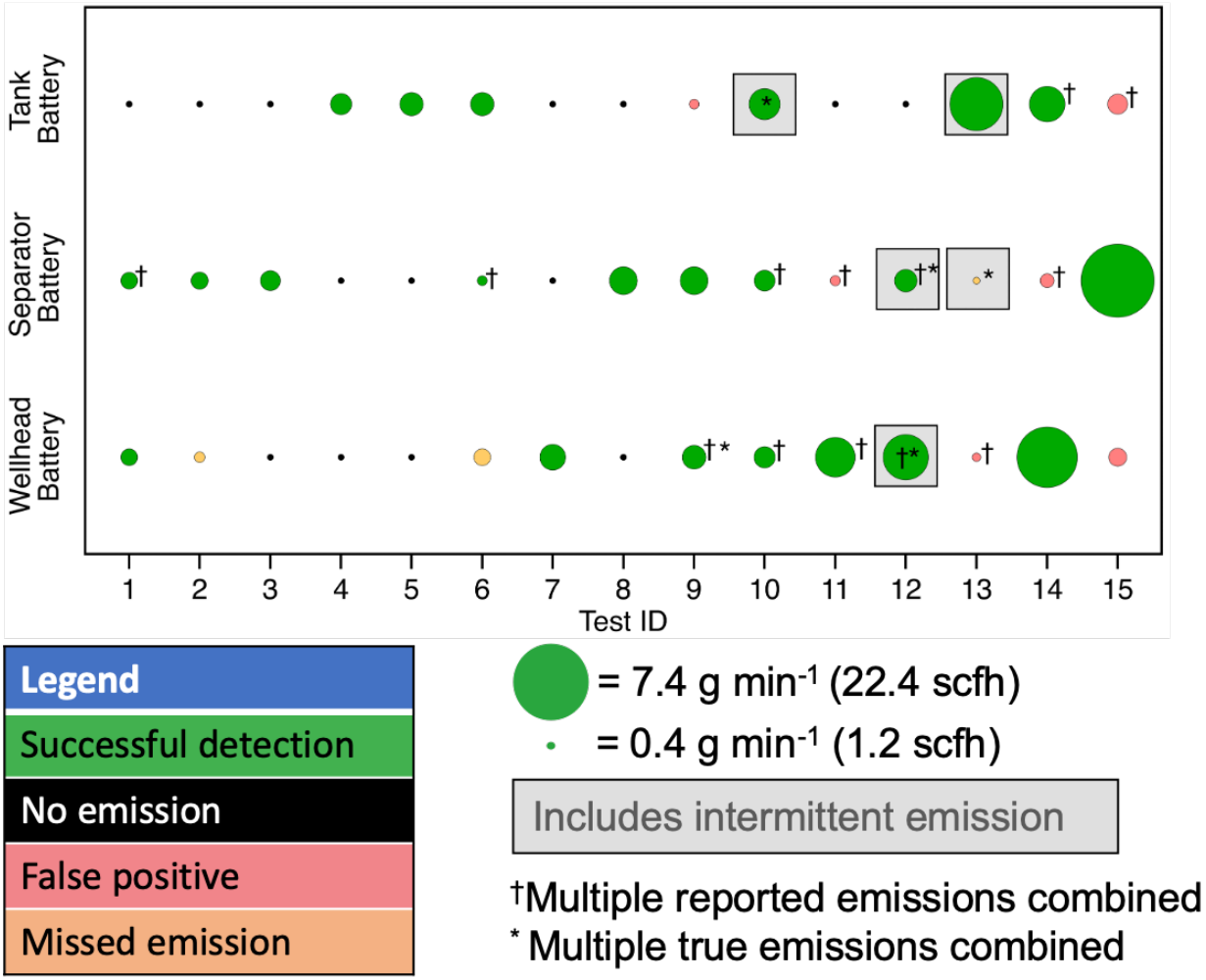

Figure 2: Overview of the METEC testing results. Each test is represented by a column in the figure and differentiated by a "Test ID" (ordered by the emission rate of the largest emission). Each row represents emissions at the battery level for a particular test. The shading of each marker represents different outcomes where: 1) dark green represents a successfully detected

emission point(s); 2) black indicates successful exclusion of a non-emitting source; 3) light red indicates a reported emission when none was present (false positive); and 4) light orange indicates an undetected true emission point. The size of the marker corresponds to the size of the true emission rate for each test; except for the false positive scenarios where the size corresponds to the DCS measured rate. Additionally, tests that included intermittent emission profiles are distinguished with a gray box around the marker.

Figure 3 shows a comparison between the measured and true emission rates (quantification), grouped at the battery level, for all detected emissions. Accurate quantification of emissions to within 1.65 g min^{-1} (5 scfh) is achieved in 82% of tests, and 91% of the emissions are accurately quantified to within 2.3 g min^{-1} (10 scfh). Of the four tests that do not achieve 1.65 g min^{-1} quantification, three include intermittent emission profiles. It should also be noted that the largest of the tested emission profiles reaches just over 7 g min^{-1}, which is far lower than the individual emission rates that are estimated to account for the majority of total emissions based on past field studies [3]. To understand why the intermittent emission tests are not quantified as well as the other tests, we perform a series of synthetic tests (see supplemental information), and find that monitoring for longer periods of time (~10-12 hours compared to the 4-hour duration of each test here) would likely have resulted in accurate quantification of these emissions. The need for longer monitoring times to accurately quantify intermittent emissions arises because the duration of some intermittent bursts tested by METEC was below our system averaging time. It is worth noting that many intermittent emissions described in the literature are longer in duration and would not pose this need [27,33]. Even with the potential offset between the timing of intermittent emissions and the system samples, the ability to provide some level of quantification is retained due to the continuous monitoring capability of the system.

Figure 4 summarizes differences in the measured versus true emission locations for the 22 detected battery-level emission events – this is calculated as the two-dimensional difference (in the ground plane or footprint), excluding heights. 60% of the emissions are attributed to within 4 m of the true location, which roughly corresponds to attribution of the emission point to one half of the equipment battery. All emissions locations are correctly estimated to within 7 m of the true emission point (equipment battery level). The level of granularity in localization from this system is correlated with the number and placement of individual beam paths; in this scenario, the level of attribution is achieved with only a single set of beam paths parsing each battery. As shown in [25], higher levels of detail can be attained for attribution through the use of more beams. Additionally, if a large enough number of unique wind vectors are sampled, attribution between multiple potential sources within a particular beam pair becomes possible due to more robust model fits in the inversion algorithm. The number of unique wind vectors can, but does not necessarily, increase with increasing measurement time on a single beam pair.

The single-blind tests presented here highlight the viability of the dual comb system as a robust emission monitoring method for real-world emission scenarios. The emission profiles were specifically designed by METEC personnel to be representative of those observed at operational facilities. These results demonstrate several key strengths and limitations of the dual comb system. For example, whereas extremely precise detection, attribution, and quantification of very small emissions (< 2 g min^{-1}) can be achieved under operational conditions from a long distance, a limitation of the system is that accurate quantification of intermittent emissions requires longer

duration of monitoring. As we describe in the following section, real-world monitoring with the DCS system can leverage monitoring durations that are continuous for days to weeks or longer, and therefore reduces issues of quantification under short-duration tests.

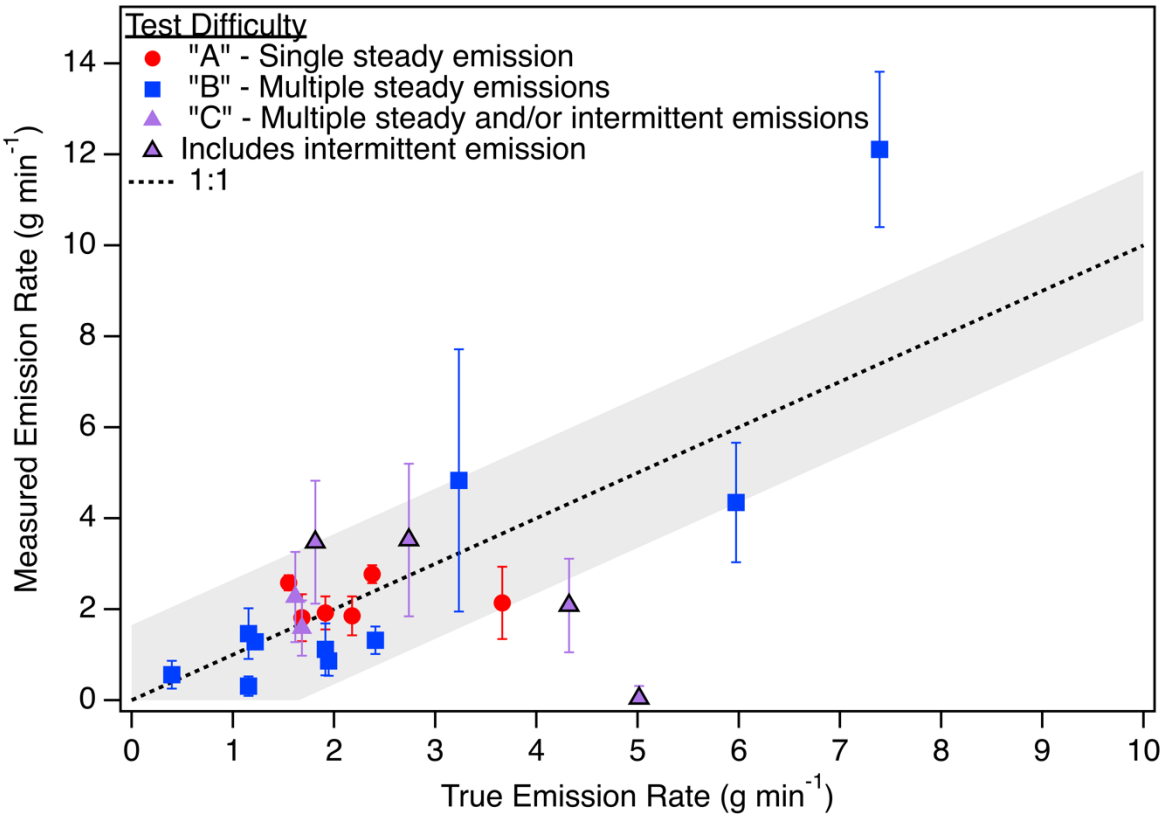

Figure 3: Scatter plot of the measured emission rate vs the true emission rate at the battery level for each detected emission. Data points are grouped by test difficulty (see main text): A – red circles; B – blue squares; and C – purple triangles. Further, the C level emissions which included intermittent emission profiles are denoted with a black outline around the marker. The shaded region around the 1:1 line shows +/- 1.65 g min^{-1} (5 scfh).

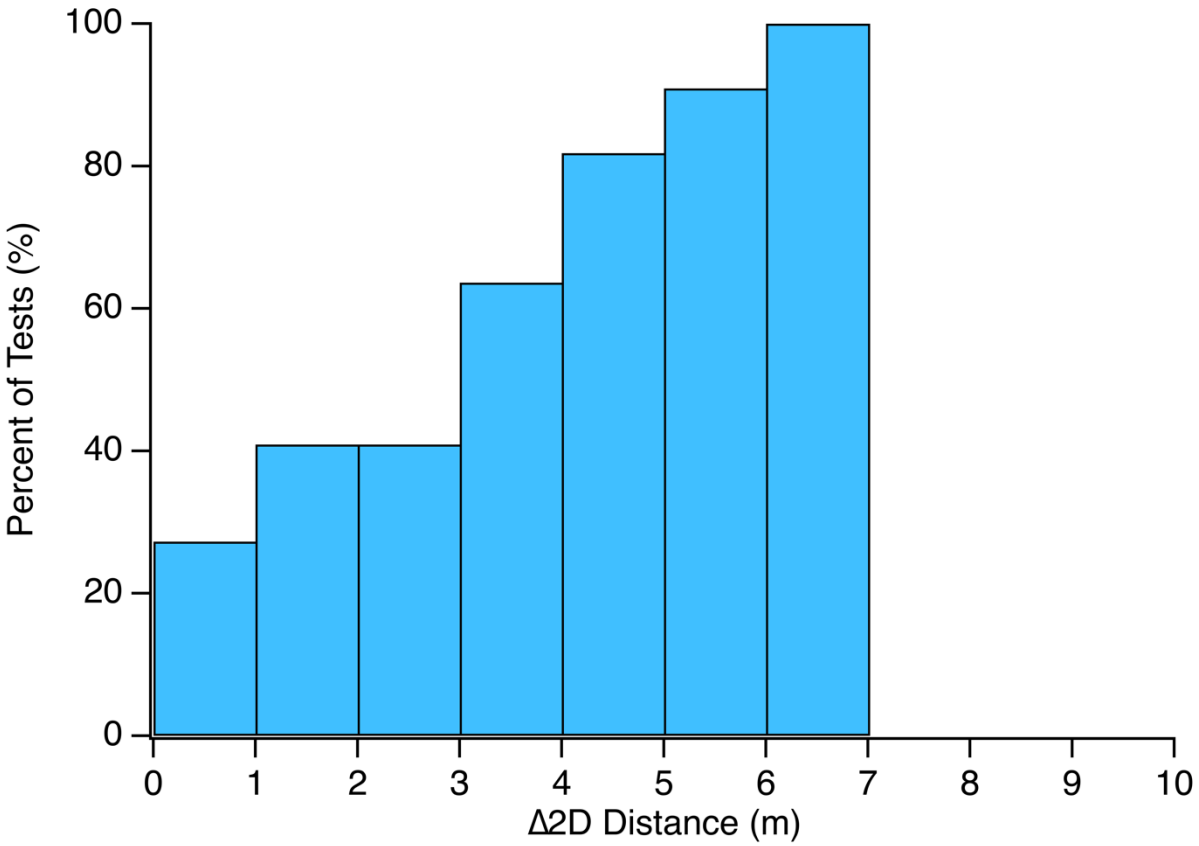

Figure 4: Cumulative histogram of the distance offset between the reported and true emission locations. For each distance (x-axis), the y-axis denotes the cumulative percentage of tests which were at or below each distance bin. This demonstrates that 100% of the tests were located to within 7 m of the true emission locations.

Natural Gas Storage Site Deployment

Currently, four DCS systems are deployed with industrial partners in the production and storage sectors. All deployments are planned to be "long-term" (6-18 months) in order to observe daily, monthly, and seasonal variability in emissions; future publications will cover in detail the deployments, measurements, and results. Here, we focus on the demonstration of the DCS Observing System for one of the natural gas storage sites as an example of how this system can be employed in a real industrial site as well as an example of the system's ability to operate autonomously and handle large changes in background methane level common at oil and gas sites.

The natural gas storage site is a moderate-size facility with several different potential sources of emissions (figure 5). Additional details about the storage site are omitted to maintain anonymity of the partner. The DCS measurements are configured to provide monitoring coverage for injection/withdrawal wells and a large natural gas-handling platform located on the facility.

The DCS is housed in a trailer located on the site with the gas-handling platform (GHP). This location is chosen to meet the goal of isolating and understanding emissions from the GHP and the two co-located banks of injection/withdrawal wells from the rest of the facility. A total of 8

beam paths are configured around the GHP - four paths per side (east/west) (figure 5). Three additional beam paths (not shown in figure 5) monitor three satellite wells that are within 800 m of the DCS system. Sampling times for each of the beam paths vary between 120-180 s depending on conditions and system performance (e.g., precipitation, condensation, etc.). The optical transceiver for the system is placed on a short (1.2 m) platform located on top of the trailer. The transceiver gimbaling system is a commercially available astronomical telescope mount. The system runs autonomously with periodic (~once per day), brief remote check-ins from Boulder, CO.

Figure 5 shows a series of DCS system measurements over a ~19 hr time frame that spans a period of variable emissions. Significant enhancements of CH_4 along beam paths downwind of the GHP are consistent under multiple changing wind directions (for example the 180º shift that occurs at ~15:30). The time-resolved emission rate is retrieved through the inversion process utilizing 3-hr measurement periods (chosen to match the time frame of the DCS Observing System validation tests at METEC). The system is capable of realizing other (higher or lower) temporal resolutions by incorporating more or fewer individual measurement samples in the inversion, generally trading higher uncertainty for higher time resolution, as discussed later. Additionally, it should be noted that the relationship between concentration enhancements and the resulting emission rate is non-linear due to atmospheric dispersion and advection of the plumes; i.e., similar concentration enhancement values can be attributed to different emission rates depending on atmospheric stability and wind characteristics. The inversion algorithm accounts for these meteorological characteristics when determining the emission rate.

The wind conditions and beam pattern are such that full characterization of the facility area is achieved through a majority of the day. During most 3-hour periods, emissions remain relatively steady at approximately 10 kg hr^{-1}. Between 09:00 - 12:00, the emission rate increases to 20 - 40 kg hr^{-1} and remains higher for ~9 hrs, until returning to a lower rate between 15:00 – 18:00. Several individual, highly elevated concentration measurements reaching up to 6 – 8 ppm (path-averaged) are noted through the measurement period. These measurements can be caused by rapid, short increases in the emission rate, or by variations in atmospheric mixing. A rapid increase in emissions is most likely the cause of three of the elevated measurements given the stability of the winds during and around the time of these particular measurements. Wind speeds are low and variable around the time of the fourth elevated concentration, which may lead to variability in localized methane mixing/pooling. If these effects are not captured by the gas transport model in the inversion, there is more uncertainty in whether rapid changes in the concentration during these types of wind conditions are due to emissions changes or variability in atmospheric mixing. Thus, due to variability in emissions, atmospheric mixing and meteorological conditions, using a limited number of observations collected during a short period in the inversion may not accurately reflect the actual time average of emissions. Therefore, continuous observations over extended time frames, such as those shown here, offer the capability of determining a more representative average emission rate for a particular monitoring time period.

The timeseries of atmospheric observations in figure 5shows that the background methane concentration can vary by up to several parts per million (ppm) throughout the day. A highly variable background signal was also observed in METEC testing. These fluctuations are likely

due to atmospheric transport of near-field and far-field emission sources that are outside the monitoring domain. Rapid background changes can present issues for monitoring approaches that have lower temporal resolution or do not account for this type of rapid background fluctuation.

Attribution of emission sources to different locations/equipment (the GHP, wells and tanks, figure 5 (a)) varies throughout the monitoring period with the largest emissions (between 10:30 and 13:30) coming from the southeast side of the GHP. However, further attribution of emissions to a single bank of equipment under this measurement configuration is hindered by the layout at this site, in which many pieces of equipment are tightly grouped. A more thorough analysis of long-term emissions will be presented in a follow-up publication (Alden et al., in prep).

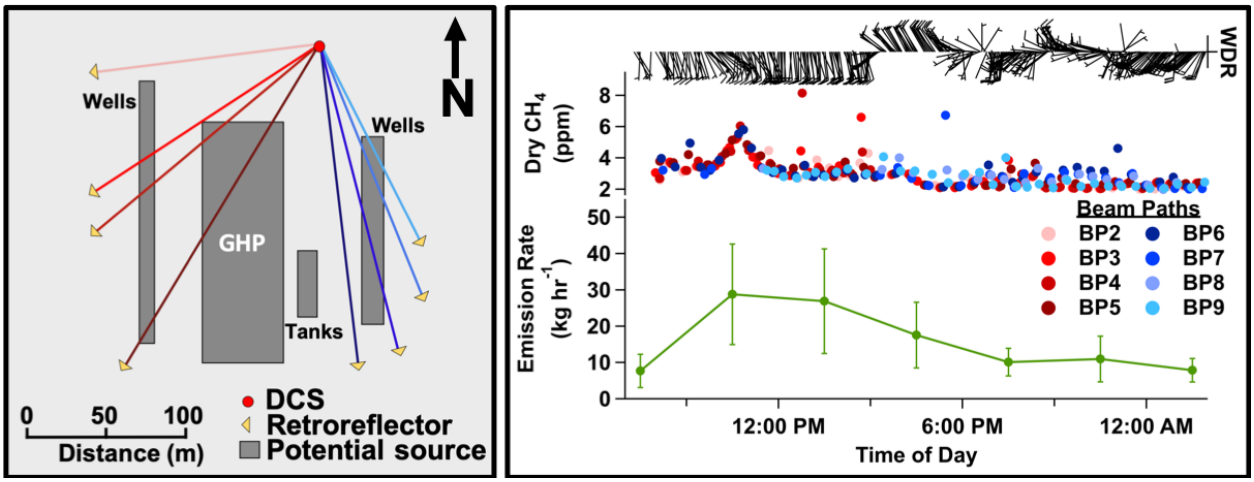

Figure 5: Data sample from the DCS system deployed at an active natural gas storage facility. Panel (a) shows a schematic of the site configuration with the beam paths overlaid – the beam path colors correspond to their respective traces on the time series plot. Panel (b) shows the methane mole fraction measurements for individual beam paths, the calculated emission rate (error bars represent the standard deviation of the results from the bootstrapped inversion method as per [26]), and the wind barbs (upper axis, arrows point towards the direction from which the wind was blowing and the number of barbs indicate wind speed).

Conclusions

We present the successful implementation and validation of a dual-frequency comb spectrometer coupled to an atmospheric inversion system (DCS Observing System) for the monitoring of methane emissions under real oil and gas emissions scenarios. We validate the DCS Observing System in a series of blinded, controlled emissions tests at the METEC test facility designed to represent operational emissions from natural gas systems. We further demonstrate successful implementation of the system at an active natural gas storage facility, where the system provides continuous emissions monitoring. The results of the two rounds of controlled testing at the METEC facility (this study and [25]) and experience gained from operating the DCS system at active natural gas handling facilities collectively validate this method and technique as a viable option for monitoring and characterization of methane emissions at temporal and spatial scales which are under-represented in currently utilized methods.

The single-blind testing conducted at the METEC facility affords the opportunity to quantitatively assess the system in a controlled setting in which complex and realistic emission scenarios are simulated. The results show that the DCS system is capable of characterizing a variety of complex emissions – including distinguishing simultaneous emissions originating from different pieces of equipment in close proximity and in some cases identifying when an emission is intermittent. Throughout the testing, 6 false positives are reported and 3 emissions go undetected – in all of these cases the emission rates are below 1.65 g min^{-1} (5 scfh). This finding suggests a detection threshold for the system of roughly 1.65 g min^{-1} from a distance of 1 km under complex monitoring conditions (i.e., multiple intermittent potential sources both inside and outside the immediate monitoring region). This threshold is very small in comparison to the distribution of emissions rates observed in past studies of the oil and gas production sector. For example, a previous device-level study around active oil and gas facilities showed that 90% of total emissions come from devices with emissions > 42 g min^{-1} (134 scfh) (e.g. [3]).

For the single-blind tests, all emissions are correctly attributed to within 7 m of the true emission location, which enables differentiation between the different batteries of equipment and often between different components of a single battery with the laser beam configuration used here. Of the reported battery-level emission rates, 84% are quantified to within 1.65 g min^{-1} (5 scfh), with the largest discrepancy (5.3 g min^{-1} [16 scfh]) occurring during a test of exclusively intermittent emission profiles (Test #13, further discussed in Appendix A). Further testing suggests that for emissions exhibiting an intermittent profile, the time required to achieve accurate quantification can be greater than that for steady emissions.

This first demonstration of a DCS Observing System deployed at an active natural gas facility is intended to show the ability to provide long-term continuous monitoring of methane emissions and variability with the overarching goal of improving our understanding of process-level emissions, their variability through time, and how the system can be used as a methane emission mitigation tool. Even with the limited data presented here, several key features are clearly demonstrated from the concentration and emission time series; 1) in areas with dense natural gas operations the background level of methane can vary significantly (several ppm in these measurements) and rapidly (variations shown in this data are >2 ppm hr^{-1} at some points); and 2) emission rates can also change dramatically (factor of 3 in this data) and on short time scales (hours) (figure 5). These events are not necessarily correlated (i.e., changes in background concentrations do not necessarily indicate the presence of a local emission source) and monitoring systems must be capable of distinguishing between them.

The results shown here demonstrate the system's ability to fill a critical spatial and temporal monitoring gap in methane observation technology. The DCS system described, validated, and field-deployed here provides continuous information on a regional scale. Full characterization (i.e., identifying emitting batteries and quantifying emissions rates) of multiple sources across a region (or facility) over extended time periods will aid in enhancing our understanding of methane sources from this important sector of global methane emissions.

Funding. Advanced Research Projects Agency-Energy, Department of Energy (award DE-AR0000539), the Department of Energy (award DE-FE0029168), and the National Institute of Standards and Technology.

Acknowledgment. The authors would like to thank research leaders and personnel at the Methane Emissions Technology Evaluation Center (METEC) as well as the Cooperative Institute for Research in the Atmosphere (CIRA) for aiding with the logistics of testing the system presented here.

Data availability statement: The data that supports the findings of this study are available upon request from the authors.

References

1. IPCC, 2013: *Climate Change 2013: The Physical Science Basis. Contribution of Working Group I to the Fifth Assessment Report of the Intergovernmental Panel on Climate Change* [Stocker, T.F., D. Qin, G.-K. Plattner, M. Tignor, S.K. Allen, J. Boschung, A. Nauels, Y. Xia, V. Bex and P.M. Midgley (eds.)]. Cambridge University Press, Cambridge, United Kingdom and New York, NY, USA, 1535 pp.
2. G. Pétron, A. Karion, C. Sweeney, B. R. Miller, S. A. Montzka, G. J. Frost, M. Trainer, P. Tans, A. Andrews, J. Kofler, D. Helmig, D. Guenther, E. Dlugokencky, P. Lang, T. Newberger, S. Wolter, B. Hall, P. Novelli, A. Brewer, S. Conley, M. Hardesty, R. Banta, A. White, D. Noone, D. Wolfe, and R. Schnell, "A new look at methane and nonmethane hydrocarbon emissions from oil and natural gas operations in the Colorado Denver-Julesburg Basin," J. Geophys. Res. Atmospheres **119**, 2013JD021272 (2014).
3. A. R. Brandt, G. A. Heath, E. A. Kort, F. O'Sullivan, G. Pétron, S. M. Jordaan, P. Tans, J. Wilcox, A. M. Gopstein, D. Arent, S. Wofsy, N. J. Brown, R. Bradley, G. D. Stucky, D. Eardley, and R. Harriss, "Methane Leaks from North American Natural Gas Systems," Science **343**, 733–735 (2014).
4. C. Frankenberg, A. K. Thorpe, D. R. Thompson, G. Hulley, E. A. Kort, N. Vance, J. Borchardt, T. Krings, K. Gerilowski, C. Sweeney, S. Conley, B. D. Bue, A. D. Aubrey, S. Hook, and R. O. Green, "Airborne methane remote measurements reveal heavy-tail flux distribution in Four Corners region," Proc. Natl. Acad. Sci. **113**, 9734–9739 (2016).
5. R. A. Alvarez, D. Zavala-Araiza, D. R. Lyon, D. T. Allen, Z. R. Barkley, A. R. Brandt, K. J. Davis, S. C. Herndon, D. J. Jacob, A. Karion, E. A. Kort, B. K. Lamb, T. Lauvaux, J. D. Maasakkers, A. J. Marchese, M. Omara, S. W. Pacala, J. Peischl, A. L. Robinson, P. B. Shepson, C. Sweeney, A. Townsend-Small, S. C. Wofsy, and S. P. Hamburg, "Assessment of methane emissions from the U.S. oil and gas supply chain," Science **361**, 186–188 (2018).
6. A. P. Ravikumar, J. Wang, M. McGuire, C. S. Bell, D. Zimmerle, and A. R. Brandt, "'"Good versus Good Enough?" Empirical Tests of Methane Leak Detection Sensitivity of a Commercial Infrared Camera," Environ. Sci. Technol. **52**, 2368–2374 (2018).
7. A. Karion, C. Sweeney, G. Pétron, G. Frost, R. Michael Hardesty, J. Kofler, B. R. Miller, T. Newberger, S. Wolter, R. Banta, A. Brewer, E. Dlugokencky, P. Lang, S. A. Montzka, R. Schnell, P. Tans, M. Trainer, R. Zamora, and S. Conley, "Methane emissions estimate from airborne measurements over a western United States natural gas field," Geophys. Res. Lett. **40**, 4393–4397 (2013).

8. H. L. Brantley, E. D. Thoma, W. C. Squier, B. B. Guven, and D. Lyon, "Assessment of Methane Emissions from Oil and Gas Production Pads using Mobile Measurements," Environ. Sci. Technol. **48**, 14508–14515 (2014).
9. D. R. Caulton, P. B. Shepson, R. L. Santoro, J. P. Sparks, R. W. Howarth, A. R. Ingraffea, M. O. L. Cambaliza, C. Sweeney, A. Karion, K. J. Davis, B. H. Stirm, S. A. Montzka, and B. R. Miller, "Toward a better understanding and quantification of methane emissions from shale gas development," Proc. Natl. Acad. Sci. **111**, 6237–6242 (2014).
10. J. R. Roscioli, T. I. Yacovitch, C. Floerchinger, A. L. Mitchell, D. S. Tkacik, R. Subramanian, D. M. Martinez, T. L. Vaughn, L. Williams, D. Zimmerle, A. L. Robinson, S. C. Herndon, and A. J. Marchese, "Measurements of methane emissions from natural gas gathering facilities and processing plants: measurement methods," Atmospheric Meas. Tech. **8**, 2017–2035 (2015).
11. T. I. Yacovitch, S. C. Herndon, G. Pétron, J. Kofler, D. Lyon, M. S. Zahniser, and C. E. Kolb, "Mobile Laboratory Observations of Methane Emissions in the Barnett Shale Region," Environ. Sci. Technol. **49**, 7889–7895 (2015).
12. B. J. Nathan, L. M. Golston, A. S. O'Brien, K. Ross, W. A. Harrison, L. Tao, D. J. Lary, D. R. Johnson, A. N. Covington, N. N. Clark, and M. A. Zondlo, "Near-Field Characterization of Methane Emission Variability from a Compressor Station Using a Model Aircraft," Environ. Sci. Technol. **49**, 7896–7903 (2015).
13. A. P. Ravikumar, S. Sreedhara, J. Wang, J. Englander, D. Roda-Stuart, C. Bell, D. Zimmerle, D. Lyon, I. Mogstad, B. Ratner, and A. R. Brandt, "Single-blind inter-comparison of methane detection technologies – results from the Stanford/EDF Mobile Monitoring Challenge," Elem Sci Anth **7**, 37 (2019).
14. E. National Academies of Sciences, *Improving Characterization of Anthropogenic Methane Emissions in the United States* (2018).
15. T. L. Vaughn, C. S. Bell, C. K. Pickering, S. Schwietzke, G. A. Heath, G. Pétron, D. J. Zimmerle, R. C. Schnell, and D. Nummedal, "Temporal variability largely explains top-down/bottom-up difference in methane emission estimates from a natural gas production region," Proc. Natl. Acad. Sci. **115**, 11712–11717 (2018).
16. D. Zavala-Araiza, R. A. Alvarez, D. R. Lyon, D. T. Allen, A. J. Marchese, D. J. Zimmerle, and S. P. Hamburg, "Super-emitters in natural gas infrastructure are caused by abnormal process conditions," Nat. Commun. **8**, ncomms14012 (2017).
17. C. Zhao, A. E. Andrews, L. Bianco, J. Eluszkiewicz, A. Hirsch, C. MacDonald, T. Nehrkorn, and M. L. Fischer, "Atmospheric inverse estimates of methane emissions from Central California," J. Geophys. Res. Atmospheres **114**, (2009).
18. W. Eugster and G. W. Kling, "Performance of a low-cost methane sensor for ambient concentration measurements in preliminary studies," Atmospheric Meas. Tech. **5**, 1925–1934 (2012).
19. K. J. Davis, A. Deng, T. Lauvaux, N. L. Miles, S. J. Richardson, D. P. Sarmiento, K. R. Gurney, R. M. Hardesty, T. A. Bonin, W. A. Brewer, B. K. Lamb, P. B. Shepson, R. M. Harvey, M. O. Cambaliza, C. Sweeney, J. C. Turnbull, J. Whetstone, and A. Karion, "The Indianapolis Flux Experiment (INFLUX): A test-bed for developing urban greenhouse gas emission measurements," Elem Sci Anth **5**, 21 (2017).
20. T. A. Fox, T. E. Barchyn, D. Risk, A. P. Ravikumar, and C. H. Hugenholtz, "A review of close-range and screening technologies for mitigating fugitive methane emissions in upstream oil and gas," Environ. Res. Lett. **14**, 053002 (2019).

21. A. Collier-Oxandale, J. G. Casey, R. Piedrahita, J. Ortega, H. Halliday, J. Johnston, and M. P. Hannigan, "Assessing a low-cost methane sensor quantification system for use in complex rural and urban environments," Atmospheric Meas. Tech. **11**, 3569–3594 (2018).
22. E. J. Zhang, C. C. Teng, T. G. van Kessel, L. Klein, R. Muralidhar, G. Wysocki, and W. M. J. Green, "Field Deployment of a Portable Optical Spectrometer for Methane Fugitive Emissions Monitoring on Oil and Gas Well Pads," Sensors **19**, (2019).
23. J. Xia, F. Zhu, S. Zhang, A. Kolomenskii, J. Dong, K. Okada, J. Strohaber, and Hans. A. Schuessler, "Probing greenhouse gases in turbulent atmosphere by long-range open-path wavelength modulation spectroscopy," Opt. Lasers Eng. **117**, 21–28 (2019).
24. S. Coburn, C. B. Alden, R. Wright, K. Cossel, E. Baumann, G.-W. Truong, F. Giorgetta, C. Sweeney, N. R. Newbury, K. Prasad, I. Coddington, and G. B. Rieker, "Regional trace-gas source attribution using a field-deployed dual frequency comb spectrometer," Optica **5**, 320–327 (2018).
25. C. B. Alden, S. Coburn, R. J. Wright, E. Baumann, K. C. Cossel, E. Perez, E. Hoenig, K. Prasad, I. R. Coddington, and G. B. Rieker, "Single-blind quantification of natural gas leaks from 1 km distance using frequency combs," Environ. Sci. Technol. **53**, 2908–2917 (2019).
26. C. B. Alden, S. Ghosh, S. Coburn, C. Sweeney, A. Karion, R. Wright, I. Coddington, G. B. Rieker, and K. Prasad, "Bootstrap inversion technique for atmospheric trace gas source detection and quantification using long open-path laser measurements," Atmospheric Meas. Tech. **11**, 1565–1582 (2018).
27. D. T. Allen, A. P. Pacsi, D. W. Sullivan, D. Zavala-Araiza, M. Harrison, K. Keen, M. P. Fraser, A. Daniel Hill, R. F. Sawyer, and J. H. Seinfeld, "Methane Emissions from Process Equipment at Natural Gas Production Sites in the United States: Pneumatic Controllers," Environ. Sci. Technol. **49**, 633–640 (2015).
28. A. Schliesser, M. Brehm, F. Keilmann, and D. W. van der Weide, "Frequency-comb infrared spectrometer for rapid, remote chemical sensing," Opt. Express **13**, 9029–9038 (2005).
29. I. Coddington, N. Newbury, and W. Swann, "Dual-comb spectroscopy," Optica **3**, 414–426 (2016).
30. G. B. Rieker, F. R. Giorgetta, W. C. Swann, J. Kofler, A. M. Zolot, L. C. Sinclair, E. Baumann, C. Cromer, G. Petron, C. Sweeney, P. P. Tans, I. Coddington, and N. R. Newbury, "Frequency-comb-based remote sensing of greenhouse gases over kilometer air paths," Optica **1**, 290–298 (2014).
31. E. M. Waxman, K. C. Cossel, G.-W. Truong, F. R. Giorgetta, W. C. Swann, S. Coburn, R. J. Wright, G. B. Rieker, I. Coddington, and N. R. Newbury, "Intercomparison of Open-Path Trace Gas Measurements with Two Dual Frequency Comb Spectrometers," Atmos Meas Tech Discuss **2017**, 1–26 (2017).
32. G.-W. Truong, E. M. Waxman, K. C. Cossel, E. Baumann, A. Klose, F. R. Giorgetta, W. C. Swann, N. R. Newbury, and I. Coddington, "Accurate frequency referencing for fieldable dual-comb spectroscopy," Opt. Express **24**, 30495–30504 (2016).
33. D. T. Allen, D. W. Sullivan, D. Zavala-Araiza, A. P. Pacsi, M. Harrison, K. Keen, M. P. Fraser, A. Daniel Hill, B. K. Lamb, R. F. Sawyer, and J. H. Seinfeld, "Methane Emissions from Process Equipment at Natural Gas Production Sites in the United States: Liquid Unloadings," Environ. Sci. Technol. **49**, 641–648 (2015).

Environmental Science & Technology

pubs.acs.org/est

Article

Temporal Variability of Emissions Revealed by Continuous, Long-Term Monitoring of an Underground Natural Gas Storage Facility

Caroline B. Alden,* Robbie J. Wright, Sean C. Coburn, Dani Caputi, Griffith Wendland, Alex Rybchuk, Stephen Conley, Ian Faloona, and Gregory B. Rieker

Cite This: *Environ. Sci. Technol.* 2020, 54, 14589–14597

Read Online

ACCESS | Metrics & More | Article Recommendations | Supporting Information

ABSTRACT: Temporal variability contributes to uncertainty in inventories of methane emissions from the natural gas supply chain. Extrapolation of instantaneous, "snapshot-in-time" measurements, for example, can miss temporal intermittency and confound bottom-up/top-down comparisons. Importantly, no continuous long-term datasets record emission variability from underground natural gas storage facilities despite substantial contributions to sector-wide emissions. We present 11 months of continuous observations on a section of a storage site using dual-frequency comb spectroscopy (DCS observing system) and aircraft measurements. We find high emission variability and a skewed distribution in which the 10% highest 3 h emission periods observed by the continuous DCS observing system comprise 41% of the total observed 3-hourly emissions. Monthly emission rates differ by >12×, and 3-hourly rates vary by 17× in 24 h. We find links to the operating phase of the facility—emission rates, including as a percentage of the total gas flow rate, are significantly higher during periods of injection compared to those of withdrawal. We find that if a high frequency of aircraft flights can occur, then the ground- and aircraft-based approaches show excellent agreement in emission distributions. A better understanding of emission variability at underground natural gas storage sites will improve inventories and models of methane emissions and clarify pathways toward mitigation.

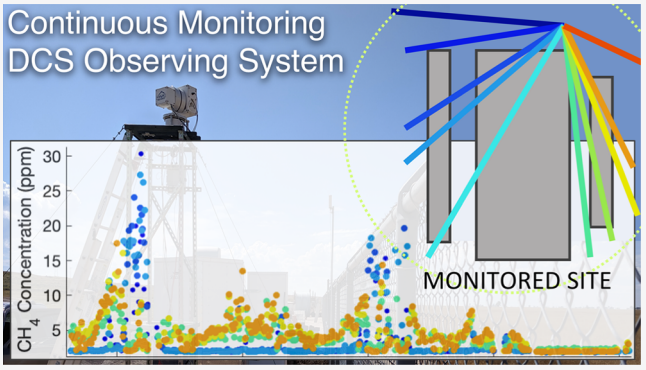

1. INTRODUCTION

Natural gas is an important energy source in the United States, comprising 28.6% of the total U.S. energy use in 2017.[1] Recently, increased scientific, regulatory, societal, and industry attention has focused on emissions of methane along the natural gas supply chain, which threaten to undermine the benefits of natural gas as a relatively lower carbon-to-energy fuel source (compared with coal)[2,3] and which can negatively impact regional air quality.[4,5] The reduction of methane emissions from oil and gas represents a relatively achievable short-term mitigation goal in comparison with longer-term control of emissions from other industries.[6] Independent assessments of emissions have revealed mismatches between bottom-up (e.g., inventory-based) and top-down (e.g., atmospheric measurement-based) estimates across the natural gas sector, from production wells to urban distribution systems.[7,8] Several new studies suggest that temporal variability in emissions as well as a fat-tailed distribution of high-emitting fugitive events can contribute to disagreements in emission estimates and that accounting for these sources of spatial and temporal variability can help to reconcile flux estimates.[9−13]

Better understanding of temporal variability in methane emissions from oil and gas infrastructure has been identified as an important area for improvement in the Environmental Protection Agency (EPA) Greenhouse Gas Inventory (GHGI).[14] Yet, high levels of uncertainty remain in our understanding of temporal characteristics of emissions. Continuous monitoring, in particular, has been identified as a critical tool for a better understanding of the temporal profile of emissions at natural gas facilities.[15] New state-level regulations in Colorado go so far as to mandate continuous monitoring of oil and gas facilities.[16]

While variability in emissions from the production and processing sector of the natural gas supply chain has been increasingly confirmed,[17] emissions from underground natural gas storage facilities have not been studied as extensively. Though there are relatively few storage facilities (~400 in the United States[18]), the transmission and storage sector is estimated to contribute a substantial proportion of value-

Received: May 17, 2020
Revised: October 10, 2020
Accepted: October 13, 2020
Published: October 27, 2020

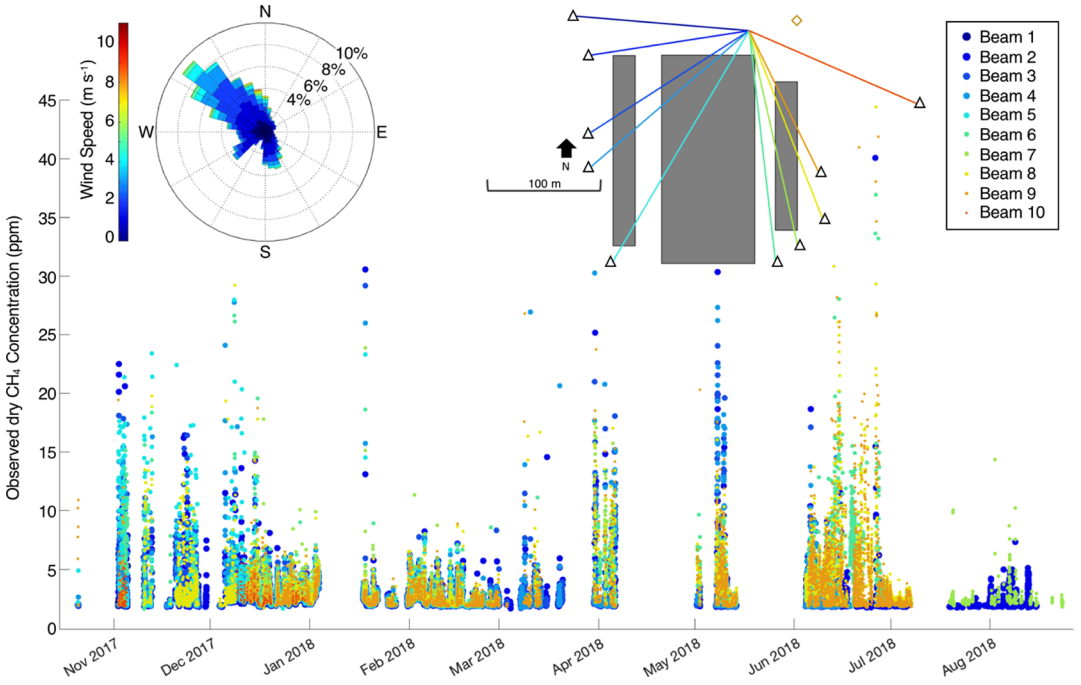

Figure 1. Time series of atmospheric observations of CH_4 concentrations along the DCS laser beam paths. The beam path and site layout are shown in a map-view inset at the upper right, including three gray areas with well heads (left box), gas conditioning equipment (middle box), and well heads (right box). Black triangles show the locations of retroreflectors and the yellow diamond shows the location of an anemometer. The inset in the upper left shows a wind rose of meteorological conditions during the observation period. The legend shows the laser beam colors and marker sizes as they relate to the site layout and concentration data.

chain emissions (20%[1]) and has garnered attention because of the recent high-profile Aliso Canyon extreme emission event.[19,20] Storage of natural gas in underground reservoirs has been practiced in the United States for over 100 years to supplement pipeline delivery during periods of variable supply and demand.[21] Storage reservoirs are primarily porous rock reservoirs (e.g., depleted oil and gas fields or aquifers) and salt caverns[18] into which gas is injected or from which it is withdrawn to level supply/demand, such as during cold snaps.[21] Gas storage is increasingly also used to meet higher-frequency changes in electricity generation, supplementing other energy sources with more variable supply (e.g., renewables).[22]

Detailed examination of emissions from specific equipment at underground storage facilities has been limited in time and has focused primarily on compressor stations.[23,24] Repeated flyover measurements of emissions from underground natural gas storage sites do, however, suggest the possibility of high emission variability.[25] For example, one recent study demonstrated emission rates that differed by up to 6× on contiguous days at the same site.[25,26]

In this study, we perform the first continuous monitoring of emissions from a portion of an underground natural gas storage facility using local atmospheric trace gas concentration measurements and inversions with a ground-based dual-frequency comb spectrometry (DCS) observing system (hereafter DCS observing system). We also perform concurrent, repeat aircraft mass balance flights for cross-validation of methods. Finally, we compare the resulting time series of estimated emissions with operations data collected by the storage site managers.

2. EXPERIMENTAL METHODS

To assess emissions and variability at an underground natural gas storage site, we deployed two sensor systems for a period of 11 months, from October 2017 through August 2018. The first is a ground-based sensor system that continuously and autonomously monitors emissions (DCS observing system, Section 2.2) and the second is an aircraft-based trace gas sensor flown for mass balance "snapshot-in-time" emission estimation (Section 2.3). The ground-based sensor is a long-range, open-path DCS. The DCS data are coupled with atmospheric inversions to determine emission source locations and rates.[27−29] The aircraft-based sampling approach relies on methods developed and tested at similar sites.[19,25,30] Both are described in greater detail below.

2.1. Underground Natural Gas Storage Site Layout.

The study site is an underground natural gas storage facility located in the U.S. Energy Information Administration (EIA) Pacific Region. The site is in the top quartile of all storage sites in the United States in terms of both base gas storage (the "permanent" inventory used to maintain the storage reservoir pressure) and total field capacity (the maximum reservoir storage capacity).[18] Continuous DCS observing system measurements and repeat aircraft mass balance flights focused on an isolated section of infrastructure on the site, which allowed for a clear constraint of signals against background emissions from neighboring sites (Figure 1). The portion of the storage site studied houses well heads and gas conditioning equipment (Figure 1 and Supporting Information Section 1 for more details regarding on-site equipment). The nearest compressors are >500 m away in a different area of the site. The study area contains just over 40% of the total well heads on the whole site and just over 20% of the filter separators, and the spatial extent of the study area covers roughly 10% of the

https://dx.doi.org/10.1021/acs.est.0c03175
Environ. Sci. Technol. 2020, 54, 14589−14597

full extent of the underground formation. Equipment heights in the study area range from roughly ground-height to roughly 13 m above the ground.

2.2. Ground-Based DCS Observing System Measurements and Data Reduction. The DCS observing system collects continuous, high-frequency atmospheric concentration measurements and atmospheric inversions yield emission rates and locations with a 3 h resolution.

A single DCS laser housed in a small trailer was placed on the north edge of a section of the above-ground infrastructure associated with the storage site (Section 2.1, Figure 1). A laser light pitch and catch system was positioned on a small retractable tower. A set of 10 retroreflective mirrors was fixed to the existing infrastructure on the site, enabling 10 integrated open paths or "beams" that extended between the laser head and each retroreflector (Figure 1). After 11 months, minor degradation of return power was observed from dust accumulation on the retroreflectors, with no impact on measurement precision or reliability. Infrequent, heavy rain occluded the line-of-sight to the retroreflectors, and morning dew occasionally and temporarily blocked the telescope window until evaporation took place. Observations were taken along one beam path at a time in sequence, and measurements were averaged for 120−180 s. Beam heights varied between 1 and 3 m above the ground level. An RM Young 81000 3D sonic anemometer was stationed at a 10 m standoff distance from the DCS to collect meteorological observations for use in the inversion (Figure 1).

DCS is a spectroscopic method that measures extremely high-resolution (0.0018 nm or 200 MHz) absorption spectra, which can be used to determine accurate and precise information about concentrations of molecular trace gases along the beam path.[31] The laser light is eye-safe and invisible. The precision of the concentration measurements during this campaign was on the order of 5−30 ppb. Critically, instrument calibration is not needed for DCS in this application because we are measuring differential enhancements among laser beams (overcoming small absolute biases of the spectroscopic model used for concentration retrieval) and because the DCS wavelength, phase noise, and return power are all continuously monitored and controlled to eliminate drift or distortion of the measured spectrum.[32] The atmospheric data (which consist of both methane and water vapor concentrations) are processed to provide dry-air path-averaged mole fractions (concentrations) of methane using spectroscopic fits to the HITRAN 2008 database. The broad wavelength range afforded by DCS (178.8−185.5 THz or 1625−1675 nm), combined with the extremely high resolution (200 MHz), allows for the simultaneous fitting of approximately 3240 individual H_2O (133), CH_4 (625), and CO_2 (2482) absorption features. This allows for a precise intercomparison of observations made on different instruments and across different time periods.[32,33] The concentration information generated in this way is used in an atmospheric inversion algorithm, which solves for the locations and rates of emissions in the monitored area. Background or baseline concentrations are removed, yielding CH_4 enhancements that are then fitted using a Gaussian plume model to parameterize atmospheric transport.[27] Potential emission sources are parsed from the areas in the gray boxes in Figure 1 into groupings of equipment, with heights assigned accordingly. The use of this system for emission quantification in blinded validation tests and at oil and gas sites has been described in several recent publications.[29,34]

We solve for emissions with 3-hourly resolution to balance data density (maximizing the number of measurements available for inversion, given the high number of beams sampled to cover a large facility) with a temporal resolution that allows for analysis of subdaily emission variability; a higher or a lower temporal resolution is possible via the balance of these two trade-offs.

Data analysis for the DCS observing system involves several steps. First, atmospheric inversions with a range of parameter choices are performed to estimate the error bounds of the emission calculation. Specifically, an ensemble of five atmospheric inversions is used, following recently published work using the DCS observing system[27−29,34] (full details in Supporting Information Section 3). Second, an analysis of site coverage is performed to guide the interpretation of the results. Changing wind conditions can result in a greater or lesser sensitivity of line-integrated measurements to emission sources at various locations on the storage site because of the geometry of the site layout. That is, the "fetch" of the area surveyed with each measurement changes based on the meteorological conditions of each measurement. Indeed, this phenomenon is a factor common to all atmospheric concentration-based observing systems and one that is particularly important for point sensor arrays that cannot offer integrated path-averaged coverage. For example, when the prevailing wind direction is from the north, plumes from some areas are less likely to cross any laser beam measurement paths ("beam") such that not all areas in the gray boxes in Figure 1 would be covered. In this case, the extent of the site coverage is expected to be lower compared with the opposite case (winds from the south) when plumes from most areas of the site are very likely to cross a laser beam measurement path, and all areas in the gray boxes shown in Figure 1 would be covered. A relationship may therefore exist between the percent of site coverage and the emission rate wherein spuriously low emissions are estimated under a lower observational coverage.

To ensure that variability in the emission rate we estimate is due to changing emission rates and not the changing site coverage, we perform an initial processing step to remove low-coverage time periods from our analysis (Supporting Information Section 4). We find that samples with <30% site coverage are likely affected by a low bias because of insufficient site coverage but that samples with >30% site coverage are likely not. To be sure that 30% is not too low a threshold for site coverage, we additionally test a range of cutoff values (Supporting Information Section 4) and report emission rates calculated for a nominally higher value of >70% site coverage.

2.3. Aircraft-Based Mass Balance Measurements. Aircraft mass balance flights occurred at regular intervals during the measurement campaign. The mass balance flights use a stacked, closed-loop methodology whereby a virtual cylinder is traced by the airplane around the potential source area. The flux normal to the cylinder is calculated using instantaneous winds[35] and observed in situ methane concentrations. The path integral is then calculated for each loop to yield the average flux divergence of methane gas at the altitude of each loop according to Gauss' Theorem.[30] Most flights in this study involved 15−25 loops flown from ∼70 m above ground level to a height above which no methane plumes were detected. Finally, the vertical integral of the flux divergences is calculated to yield a total emission rate for the area within the circle.

https://dx.doi.org/10.1021/acs.est.0c03175
Environ. Sci. Technol. 2020, 54, 14589−14597

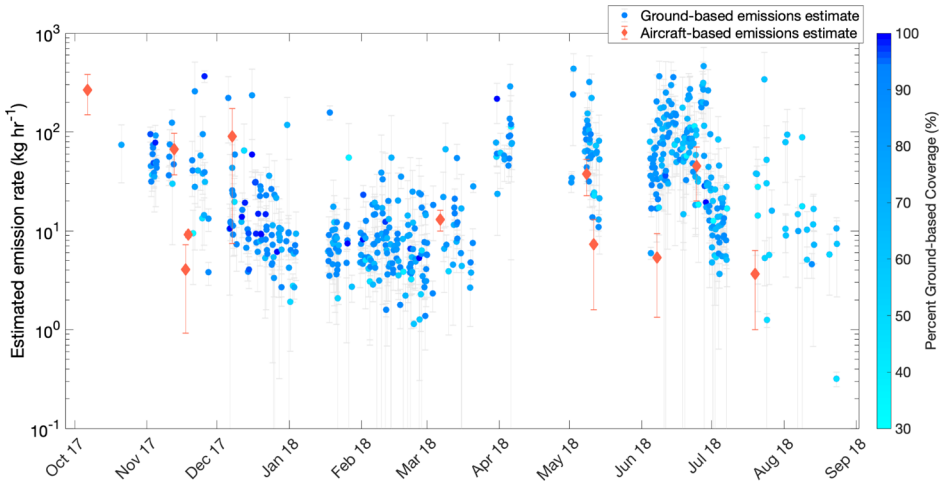

Figure 2. 3-hourly emission estimates (blue dots) of the ground-based DCS observing system and aircraft-based mass balance emission estimate (red diamonds) on a log scale. Gradation of color for the ground-based DCS observing system emission estimates represents the percent of equipment on site covered by observations in each 3 h period (color bar). Uncertainty bars are 1σ.

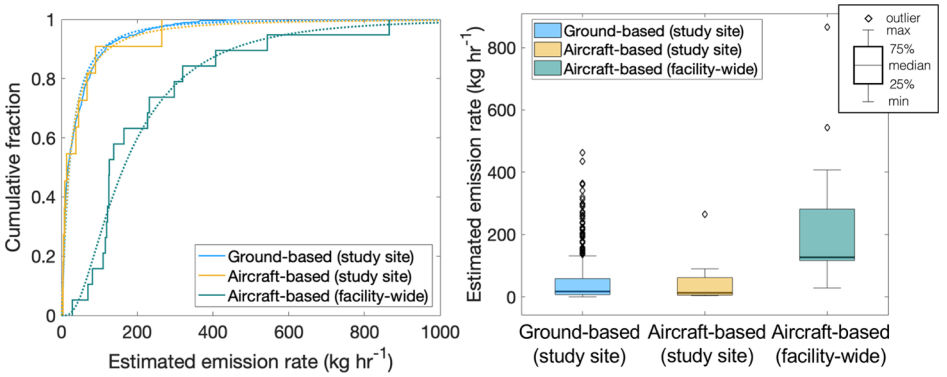

Figure 3. Empirical (solid step lines) and fitted (dotted curves) cumulative distribution functions (left panel) for the ground-based rates for the study site (blue), aircraft-based rates for the study site (yellow), and aircraft-based rates for the entire facility (teal). Box and whisker plots showing range, variability, and outliers for the estimated emission rates (right panel) for ground-based rates for the study site (blue, left box), aircraft-based rates for the study site (yellow, middle box), and aircraft-based rates for the entire facility (teal, right box).

An update to previous methods[30,35] is developed here, in which the slope in the lowest available 100 m altitude bin is extrapolated to the ground rather than assuming a constant value. The standard deviation of an individual loop flux within each 100 m bin is multiplied by the bin thickness (100 m) to obtain an error estimate for that bin. An error term for the total flux emission is then calculated by combining each bin's error term in a standard error propagation.[36]

During the measurement period of October 2017 through August 2018, 11 aircraft mass balance flights were performed. The average duration of airborne sampling measurements was 23 min.

3. RESULTS AND DISCUSSION

3.1. Atmospheric Concentration Measurements. Atmospheric concentration measurements are made along open beam paths as shown in the site layout in Figure 1. The line-integrated concentrations are divided by the path length of the laser to yield path-averaged concentrations. Concentration measurements span a large range, from values near the global mean (the marine boundary layer global annual mean CH_4 dry-air mole fractions were 1849.65 ppb in 2017 and 1857.30 ppb in 2018[37]) to isolated peaks of up to ~42,000 ppb. The mean and standard deviation of all concentration measurements is 3281 ± 2413 ppb and the median value is 2449 ppb. Several data gaps, evident in Figure 1, are due to two factors. First, this deployment was the first sustained, remote, autonomous field deployment of the DCS observing system. As such, multiple system upgrades were implemented during the 11-month field deployment, associated with lessons learned on the ground, including improved electrical power conditioning, better climate control of the laser system, and deterrents for wasps and birds in the telescope. Second, major on-site operations resulted in temporary blocking of some retroreflectors, a factor that has led to alternate beam path configurations in subsequent industrial deployments.

3.2. Study Site Emission Estimates. We examine 3-hourly mean emissions (i.e., the average emission rate over 3 h in kg h^{-1}) at the study site (all areas shown in Figure 1) and aircraft-based estimates of emissions from the study site as well as from the entire facility. The time series of estimated emissions at the study site based on the DCS observing system and aircraft mass balance flights is shown in Figure 2. Substantial temporal variability and spread are evident in both the aircraft and DCS observing system estimates. The DCS observing system emission estimates shown in Figure 2 are shaded according to percent site coverage (Section 2.2).

https://dx.doi.org/10.1021/acs.est.0c03175
Environ. Sci. Technol. 2020, 54, 14589−14597

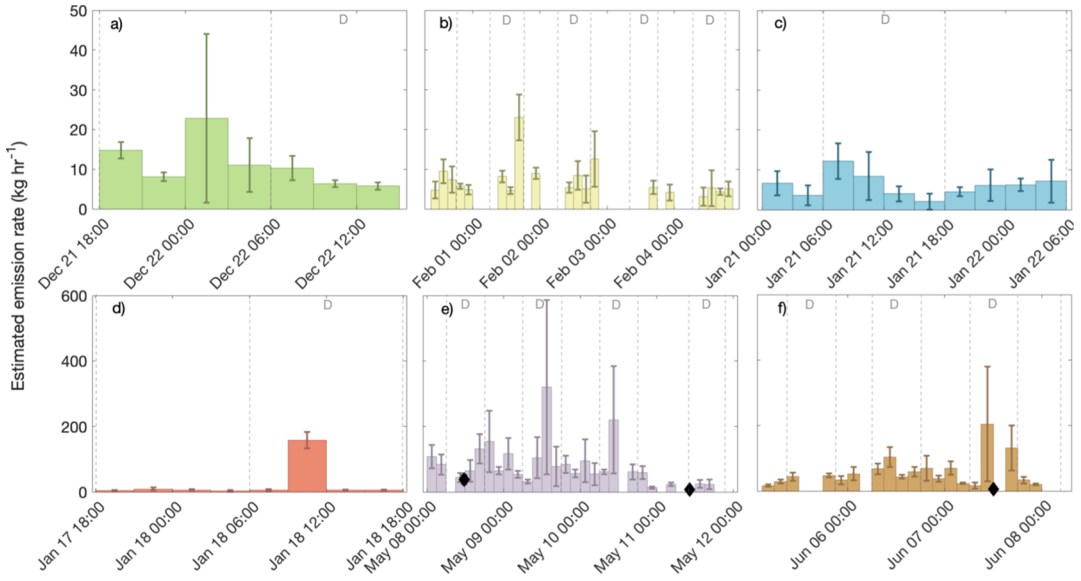

Figure 4. Ground-based DCS observing system emission estimates (bars) and aircraft-based mass balance emission estimates (black diamonds) for six time periods. (a−c) Time periods during which the variability in 3 h estimated emission rates is low compared with time periods shown in (d−f). Note the change in the *y*-axis from (a−c) to (d−f). Uncertainty bars are 1σ, and the width of each bar is 3 h. Dashed vertical gray lines distinguish day (6:00−18:00, labeled "D") from night.

3.3. Long-Term Emission Rates and Variability. The study site emission rates estimated by both the ground- and aircraft-based approaches are highly skewed. Figure 3 shows cumulative distributions of the emission rates. For the 3 h-average ground-based data, the maximum emission rate observed is 2.4 times the 95% fractile of the distribution. Finding that emission rates follow a lognormal distribution, we report the geometric mean for all emission time series. The emissions during all time periods (October 2017 through August 2018) are lognormally distributed (the mean and standard deviation of the log of the distribution are μ = 3.0 and σ = 1.3) with a geometric mean rate of 20 [−2, +3] kg h^{-1} (n = 560) [95% confidence interval (CI)]. (For all lognormally distributed results, we report the geometric mean and 95% CI of the distribution.) Using a >70% site coverage threshold, the geometric mean emission rate is the same (20 [−3, +3] kg h^{-1}) and the lognormal distribution parameters are μ = 3.0 and σ = 1.5.

During the same time period, the aircraft-based emission rates also follow a lognormal distribution with parameters of the log of the distribution of the data of μ = 3.0 and σ = 1.4. The geometric mean of the aircraft-based estimated emission rates is 19.9 [−12.3, +32.0] kg h^{-1} (n = 11) (95% CI), indicating close agreement between the ground- and aircraft-based approaches.

The presence of more high outliers and a higher upper adjacent value in the continuous ground-based data, compared with the aircraft-based data, while the median and 25th and 75th percentile ranges and distributions are very similar, suggests that the increase in data density afforded by continuous monitoring allows for a fuller representation of the emission distribution (Figure 3). Indeed, the aircraft data only capture one outlier event, without which the distribution changes substantially with a geometric mean emission rate of only 15.3 [−8.8, +20.9] kg h^{-1}. We find that these outlier time periods comprise a critical proportion of overall emissions. The 10% highest 3 h emission periods observed by the continuous DCS observing system (outliers in Figure 3) comprise 41% of the total observed 3-hourly emissions. This suggests that intermittent monitoring is very unlikely to accurately capture total emissions, compared with continuous monitoring.

Additional aircraft flights occurred before and after the DCS observing system campaign. The geometric mean of the estimated emission rates from all aircraft mass balance flights that occurred between October 2017 and June 2019 is 26.5 [−13.1, +26.0] kg h^{-1} (n = 17) (95% CI), with a lognormal distribution with log transform parameters μ = 3.3 and σ = 1.3. Two-sample Kolmogorov−Smirnov testing of all three combinations of data (long-term and short-term aircraft, long-term aircraft and ground, and short-term aircraft and ground) confirms that they are from the same distribution. The agreement in distributions suggests that the time period of observation was sufficient to accurately capture the true distribution of emissions from the study area.

The emission rates demonstrate substantial variability through time, not only on shorter (day-to-day) but also on longer (month-to-month) time scales. Monthly geometric mean emission rates from the DCS observing system vary from a minimum of 6 [−2, +2] kg h^{-1} in February 2018 to a maximum of 85 [−22, +30] kg h^{-1} in April 2018 (Supporting Information Section 5). The aircraft-based emission estimates show an even wider range, although with a low number of monthly samples.

To better understand day-to-day and subdaily variability, we focus on several multiday periods in which favorable winds allowed for continuous observation of emissions from >30% of the site area. We examine three relatively low-variability time periods and three relatively high-variability time periods, including one time period during which a transient but large spike in emissions occurs. Figure 4a−c shows periods of relatively low variability in emissions and low mean emission rates overall. The geometric mean and full range of observed emission rates are 10 (6−23) , 6 (3−23), and 6 (2−12) kg h^{-1} for a−c, respectively. Figure 4d−f shows relatively higher and more variable emission rates. The geometric mean and range of observed emission rates are 9 (4−158), 66 (14−320), and

https://dx.doi.org/10.1021/acs.est.0c03175
Environ. Sci. Technol. 2020, 54, 14589−14597

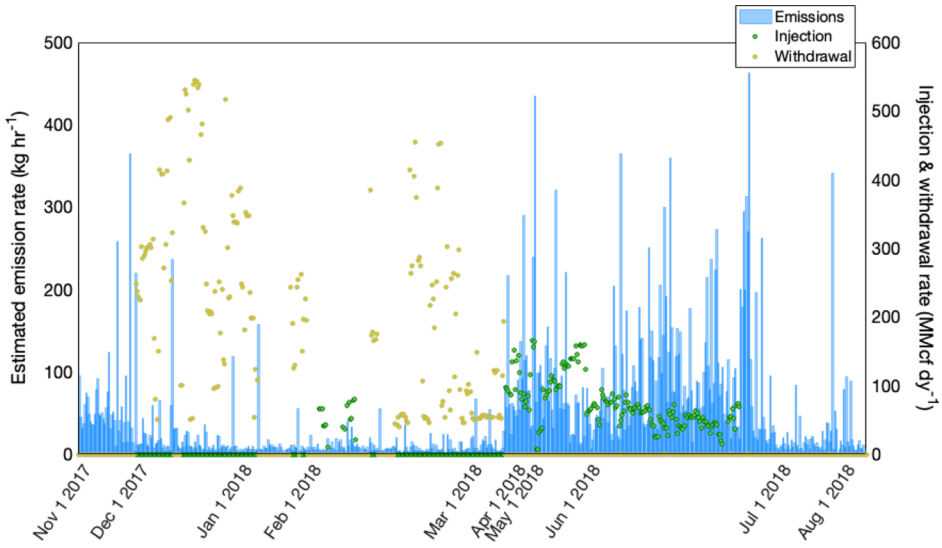

Figure 5. Time series of emissions (blue bars with a width of 3 h) with injection (green dot) and withdrawal (yellow dot) rates. Gaps in time series have been removed; the first day of each month is labeled on the *x*-axis.

46 (17−204) kg h^{-1} for d−f, respectively. The majority of the time period in Figure 4d shows emission rates below 10 kg h^{-1}; however, one 3 h period demonstrates a much higher emission rate of 158 ± 25 kg h^{-1} (1σ).

We examine the concentration data that are used to estimate the emission profiles in Figure 4d,e. One transient increase in emissions (Figure 4d) is associated with a spike in concentration measurements of roughly 30 ppm that is only 45 min in duration (Supporting Information Figure S3), indicating that even 3 h is too long a time period to fully capture the temporal variability in emissions at the site. The mean emission rate during the 3 h in which this event occurs is more than 17× the 24 h mean emission rate.

The high emission rate variability in Figure 4e is also accompanied by highly variable concentration measurements. Throughout the days of May 8−10, emission rates and atmospheric concentrations are both relatively high and variable, with a mean of 3.36 ppm and a range of 1.18−44.47 ppm (Supporting Information Figure S3). Beginning May 11, however, emission rates and atmospheric concentrations both return to lower values that vary less through time. Aircraft measurements made during the same 4-day period show a consistent signature of higher emissions during May 8−10 and lower emissions on May 11. Clustered aircraft flights during different time periods show similar variability; for example, three aircraft flights within a span of 7 days in November 2017 exhibit a nearly 17-fold difference (Figure 2). These examples highlight the uncertainties inherent in "snapshot" sampling of highly variable emission sources, as seen here, and underscore the importance of continuous monitoring for an accurate understanding of total emissions and for rapid identification of emission events in case they are driven, for example, by malfunctioning equipment that would benefit from rapid repair. Conversely, snapshots in time can capture large emissions that are not persistent and therefore overestimate total emissions through time. A snapshot, drive-by or fly-by emission estimate on the afternoon of May 10, for example, would have recorded an emission rate at least 8× higher than an estimation made the following day.

3.4. Comparison of the DCS Observing System and Aircraft Mass Balance. Periods of overlap between the aircraft and DCS observing system sampling offer an opportunity to examine potential differences between the two methods. We reanalyze the DCS observing system data by examining emissions in 3 h windows centered on the time that each aircraft mass balance flight took place. In one instance, individual ensemble members have fewer than three downwind data points, so a 6 h window is used.

All concurrent aircraft and DCS observing system estimates agree to within 2σ uncertainty; however, some uncertainties are large for both methods, masking discrepancies. The overall root mean squared error between the estimated emission rates is 42 kg h^{-1}. A Bland−Altman analysis highlights differences between the methods based on the mean of both methods as a best estimate of the "true" value. No consistent bias is observed between methods, and all values fall within the 95% level of agreement (Supporting Information Section 9).

A recent study shows similar or greater magnitudes of discrepancy on same-day, same-facility flights using different aircraft emission estimation methods.[26] A possible source of the mismatch observed in our analysis is a difficulty in obtaining truly temporally concurrent estimates. Aircraft mass balance flights last only 23 min on average, compared with ground-based observation windows of several hours. Given the very short-term variability in the emission rates we observe (e.g., Figure 4), it may be expected that emission rates vary on shorter timescales than 3 h. While discrepancies are evident between some concurrent aircraft and DCS observing system estimates, the distributions of the long-term datasets are nonetheless very similar for the two methods (Figure 3). A future study using large eddy simulations of these data will yield further insights into potential drivers of the observed offsets of individual flight days.

3.5. Facility-Wide Emissions. In addition to aircraft mass balance flights that isolated emissions from the primary study site, a series of 19 flights characterizing the entire underground natural gas storage facility were performed between October 2017 and June 2019 (see Supporting Information Sections 1 and 7 and Figure S2 for details of the full facility and time series of emissions). Very high variability and skewness in emissions are recorded by the facility-wide mass balance flights (Figure 3). The geometric mean emission rate for the entire

https://dx.doi.org/10.1021/acs.est.0c03175
Environ. Sci. Technol. 2020, 54, 14589−14597

time period is 164.6 [−51.8, +75.5] kg h^{-1} (95% CI), and the mean and standard deviation of the distribution of the log of emissions are μ = 5.1 and σ = 0.8. Despite the non-normal distribution of emissions, we examine the arithmetic mean facility-wide emission rate for comparison with past studies.[25] The arithmetic mean of the facility-wide emission rate is 222.1 ± 24.2 kg h^{-1} (2σ uncertainty) or roughly 4× the rate observed at the smaller section of the site. Two outliers drive the mean value higher (Figure 3 and Supporting Information Figure S2); removal of these outliers yields a mean rate of 165.3 kg h^{-1}. Both the arithmetic mean and the arithmetic mean with outliers removed are within the range of reported emission rates observed at other storage sites.[25,26] The drastic difference in the mean emission rate when outliers are and are not considered underscores the importance of either continuous or high-frequency, repeat measurement of storage facilities to allow for accurate capture of the true distribution of emission rates.

3.6. Comparison with Operations Data. To better understand potential sources of variability in the methane emission rate from the study site, we examine time series of operations data, including injection and withdrawal rates and leak detection and repair schedules. We find a statistically significant difference in emission rates during periods of injection (geometric mean rate of 56 [−7, +9] kg h^{-1}) compared with periods of withdrawal (8 [−1, +1] kg h^{-1}) (Figure 5 and Supporting Information Section 6). Similarly, CH_4 emissions as a percentage of the total gas flow rate (injection or withdrawal) are consistently higher during the injection phase compared with the withdrawal phase (Supporting Information Figure S1).

A statistically significant difference between emission rates estimated by the aircraft mass balance is not found; however, this is likely due to the significantly lower number of samples in the study period. For example, only two flights occurred during periods of withdrawal. While injection and withdrawal rates appear to be correlated with emission rates, relatively high emissions also occur at the beginning and end of the time series: periods during which neither injection nor withdrawal is occurring at the study site.

Higher emissions might be expected from some equipment, such as compressors, during injection and withdrawal because of the known methane slip associated with compression.[38] However, with no compressors on the study site (and the presence of gas conditioning equipment, which is used during withdrawal), it will remain the subject of future continuous monitoring studies with a higher spatial attribution to determine the source of higher emissions during injection. Analysis confirms that interference from compressor emissions did not skew our findings (Supporting Information Section 2). We therefore posit that the higher system pressures present during the injection phase could be driving pressure-based emission behavior.

Available work logs detailing locations and dates of leak detections and repair activities offer an opportunity for comparison with emissions. We find that a series of operations notes logged on 1/18/2018 coincide with the anomalous emission event shown in Figure 4d. The notes suggest the detection and logging of an issue with a series of well heads that the operator found to be below internal standards. We further find that the cessation of a nearly 3-day-long period of withdrawal at this section of the site coincides with the timing of the event shown in Figure 4 d. The site operator suggests the possibility of maintenance or blowdown activity, although a detailed record of maintenance corresponding with the emission event is not available. We find that a series of notes on recommended repairs also coincide with other periods of transient, higher-emission rates from this section of the site. The finding that higher emissions are associated with repairs is confirmed by the site operator who reports that, typically, maintenance on well heads requires blowdown of the well head and the associated piping.

Finally, we find some evidence that daytime emissions differ from nighttime emissions depending upon the operating phase, but results are uncertain and require further investigation with additional data before conclusions can be drawn (Supporting Information Section 11).

3.7. Greenhouse Gas Inventory Relevant Numbers. This study produces, for the first time, long-term observations of variability in emissions from an underground natural gas storage facility. Nearly a full year of regular measurements allow for estimation of the full range of variability at the site measured. We find that a minimum of roughly monthly aircraft flights is necessary to adequately capture the distribution of emissions observed with continuous monitoring. If, for example, the aircraft flights had commenced just weeks later, missing the only outlier event captured by the aircraft, the distribution would have changed significantly (mean and standard deviation of the log of μ = 2.7 and σ = 1.2 compared with the aircraft−ground agreed on values of μ = 3.1 and σ = 1.3). This finding further underscores the importance of continuous or quasicontinuous (high frequency) monitoring for accurate capture of emission distributions from natural gas systems, including underground natural gas storage infrastructure.

We further compare available emission inventory numbers for the facility with our emission data. There is no inventory number for the smaller subsection of the site studied, only for the entire site. However, the 19 aircraft mass balance measurements of the entire underground natural gas storage facility (Section 3.5) are directly comparable to the facility-wide inventory estimate. We find good agreement between the inventory value of 1997 metric tons yr^{-1} and the aircraft-based estimated facility-wide mean and standard deviation of 1937 ± 1765 metric tons yr^{-1}. We report arithmetic mean and standard deviation for direct comparison with inventories and past studies.[25]

3.8. Implications and Opportunities for Future Mitigation Efforts. The findings of this work suggest that emissions from underground natural gas storage can vary substantially through time, with monthly geometric mean emission rates differing by more than 12× and 3-hourly mean emission rates varying by more than 17× in a 24 h period. We find a significant difference between emission rates during different operating phases of the facility (injection or withdrawal) and some evidence of higher emissions during logged work at the facility. These findings highlight the need for high-frequency or continuous monitoring for accurate emission quantification and characterization of emission distributions at underground natural gas storage facilities, as has been found for other sectors of the natural gas supply chain. In particular, this study supports the importance of Colorado's SB 19-181 legislation requiring that oil and gas operators (including in the storage segment) install continuous methane emissions monitors at facilities with large emissions potential.[16] The inclusion of quantified indicators of variability

https://dx.doi.org/10.1021/acs.est.0c03175
Environ. Sci. Technol. 2020, 54, 14589−14597

in inventories will help end-users and stakeholders to appropriately contextualize temporally limited versus temporally continuous measurement campaigns. Finally, these findings offer insights into potential areas of focus for future emission mitigation activities.

■ ASSOCIATED CONTENT

Supporting Information

The Supporting Information is available free of charge at https://pubs.acs.org/doi/10.1021/acs.est.0c03175.

Details of storage site equipment, testing of potential interference from compressors, emission rates as a percentage of injection and withdrawal rates, facility-wide emission time series, overlapping aircraft and ground data time series, wellhead emissions, and analysis of diurnal variation in emissions (PDF)

■ AUTHOR INFORMATION

Corresponding Author

Caroline B. Alden − *Precision Laser Diagnostics Laboratory and Cooperative Institute for Research in Environmental Sciences, University of Colorado Boulder, Boulder, Colorado 80309, United States;* orcid.org/0000-0002-5249-7800; Email: caroline.alden@colorado.edu

Authors

Robbie J. Wright − *Precision Laser Diagnostics Laboratory, University of Colorado Boulder, Boulder, Colorado 80309, United States*

Sean C. Coburn − *Precision Laser Diagnostics Laboratory, University of Colorado Boulder, Boulder, Colorado 80309, United States*

Dani Caputi − *University of California, Davis, California 95616, United States*

Griffith Wendland − *Precision Laser Diagnostics Laboratory, University of Colorado Boulder, Boulder, Colorado 80309, United States*

Alex Rybchuk − *Precision Laser Diagnostics Laboratory, University of Colorado Boulder, Boulder, Colorado 80309, United States*

Stephen Conley − *Scientific Aviation, Boulder, Colorado 80301, United States;* orcid.org/0000-0001-6753-8962

Ian Faloona − *University of California, Davis, California 95616, United States*

Gregory B. Rieker − *Precision Laser Diagnostics Laboratory, University of Colorado Boulder, Boulder, Colorado 80309, United States*

Complete contact information is available at: https://pubs.acs.org/10.1021/acs.est.0c03175

Author Contributions

The manuscript was written through contributions of all authors. All authors have given approval to the final version of the manuscript.

Funding

Funding for this work comes from the Department of Energy, National Energy Technology Laboratory, Office of Fossil Energy (DE- FE0029168); Advanced Research Projects Agency—Energy (ARPA-E) (DE-AR0000539); USDA National Institute of Food and Agriculture (hatch project CA-D-LAW-2229-H, "Improving Our Understanding of California's Background Air Quality and Near-Surface Meteorology").

Notes

The authors declare the following competing financial interest(s): C. Alden, R. Wright, S. Coburn and G. Rieker disclose financial interest in the company LongPath Technologies Inc., a commercial entity that employs similar trace gas sensing and inversion techniques to those used in this study.

■ ACKNOWLEDGMENTS

The authors wish to acknowledge the facility operators for invaluable data contributions and discussions.

■ REFERENCES

(1) Inventory of U.S. *Greenhouse Gas Emissions and Sinks 1990−2017*; EPA 430-R-19-001, 2019.

(2) Hayhoe, K.; Kheshgi, H. S.; Jain, A. K.; Wuebbles, D. J. Substitution of Natural Gas for Coal: Climatic Effects of Utility Sector Emissions. *Clim. Change* **2002**, *54*, 107−139.

(3) Alvarez, R. A.; Pacala, S. W.; Winebrake, J. J.; Chameides, W. L.; Hamburg, S. P. Greater Focus Needed on Methane Leakage from Natural Gas Infrastructure. *Proc. Natl. Acad. Sci.* **2012**, *109*, 6435−6440.

(4) Gilman, J. B.; Lerner, B. M.; Kuster, W. C.; de Gouw, J. A. Source Signature of Volatile Organic Compounds from Oil and Natural Gas Operations in Northeastern Colorado. *Environ. Sci. Technol.* **2013**, *47*, 1297−1305.

(5) Thompson, C. R.; Hueber, J.; Helmig, D. Influence of Oil and Gas Emissions on Ambient Atmospheric Non-Methane Hydrocarbons in Residential Areas of Northeastern Colorado. *Elem. Sci. Anth.* **2014**, *2*, 000035.

(6) Saunois, M.; Jackson, R. B.; Bousquet, P.; Poulter, B.; Canadell, J. G. The Growing Role of Methane in Anthropogenic Climate Change. *Environ. Res. Lett.* **2016**, *11*, 120207.

(7) Alvarez, R. A.; Zavala-Araiza, D.; Lyon, D. R.; Allen, D. T.; Barkley, Z. R.; Brandt, A. R.; Davis, K. J.; Herndon, S. C.; Jacob, D. J.; Karion, A.; Kort, E. A.; Lamb, B. K.; Lauvaux, T.; Maasakkers, J. D.; Marchese, A. J.; Omara, M.; Pacala, S. W.; Peischl, J.; Robinson, A. L.; Shepson, P. B.; Sweeney, C.; Townsend-Small, A.; Wofsy, S. C.; Hamburg, S. P. Assessment of Methane Emissions from the U.S. Oil and Gas Supply Chain. *Science* **2018**, *361*, No. eaar7204.

(8) Plant, G.; Kort, E. A.; Floerchinger, C.; Gvakharia, A.; Vimont, I.; Sweeney, C. Large Fugitive Methane Emissions From Urban Centers Along the U.S. East Coast. *Geophys. Res. Lett.* **2019**, *46*, 8500−8507.

(9) Brandt, A. R.; Heath, G. A.; Cooley, D. Methane Leaks from Natural Gas Systems Follow Extreme Distributions. *Environ. Sci. Technol.* **2016**, *50*, 12512−12520.

(10) Frankenberg, C.; Thorpe, A. K.; Thompson, D. R.; Hulley, G.; Kort, E. A.; Vance, N.; Borchardt, J.; Krings, T.; Gerilowski, K.; Sweeney, C.; Conley, S.; Bue, B. D.; Aubrey, A. D.; Hook, S.; Green, R. O. Airborne Methane Remote Measurements Reveal Heavy-Tail Flux Distribution in Four Corners Region. *Proc. Natl. Acad. Sci.* **2016**, *113*, 9734−9739.

(11) Zavala-Araiza, D.; Alvarez, R. A.; Lyon, D. R.; Allen, D. T.; Marchese, A. J.; Zimmerle, D. J.; Hamburg, S. P. Super-Emitters in Natural Gas Infrastructure Are Caused by Abnormal Process Conditions. *Nat. Commun.* **2017**, *8*, ncomms14012.

(12) Vaughn, T. L.; Bell, C. S.; Pickering, C. K.; Schwietzke, S.; Heath, G. A.; Pétron, G.; Zimmerle, D. J.; Schnell, R. C.; Nummedal, D. Temporal Variability Largely Explains Top-down/Bottom-up Difference in Methane Emission Estimates from a Natural Gas Production Region. *Proc. Natl. Acad. Sci.* **2018**, *115*, 11712−11717.

(13) Johnson, D.; Heltzel, R.; Oliver, D. Temporal Variations in Methane Emissions from an Unconventional Well Site. *ACS Omega* **2019**, *4*, 3708−3715.

(14) Heath, G. A. *Taxonomy, Life Cycle Assessment, and Meta-Analyses for Improving Methane Emissions Estimates from Oil and Gas*; NREL/PR-6A20-68478; National Renewable Energy Lab. (NREL): Golden, CO (United States), 2019.

(15) National Academies of Sciences Engineering, and Medicine. *Improving Characterization of Anthropogenic Methane Emissions in the United States*; National Academies Press: Washington, D.C., 2018.
(16) Protect Public Welfare Oil and Gas Operations Colorado General Assembly. https://leg.colorado.gov/bills/sb19-181 (accessed Jan 15, 2020).
(17) Lavoie, T. N.; Shepson, P. B.; Cambaliza, M. O. L.; Stirm, B. H.; Conley, S.; Mehrotra, S.; Faloona, I. C.; Lyon, D. Spatiotemporal Variability of Methane Emissions at Oil and Natural Gas Operations in the Eagle Ford Basin. *Environ. Sci. Technol.* **2017**, *51*, 8001−8009.
(18) U.S. Energy Information Administration (EIA) https://www.eia.gov/naturalgas/ngqs/#?report=RP7&year1=2018&year2=2018&company=Name (accessed Dec 2, 2019).
(19) Conley, S.; Franco, G.; Faloona, I.; Blake, D. R.; Peischl, J.; Ryerson, T. B. Methane Emissions from the 2015 Aliso Canyon Blowout in Los Angeles, CA. *Science* **2016**, *351*, 1317−1320.
(20) Michanowicz, D. R.; Buonocore, J. J.; Rowland, S. T.; Konschnik, K. E.; Goho, S. A.; Bernstein, A. S. A National Assessment of Underground Natural Gas Storage: Identifying Wells with Designs Likely Vulnerable to a Single-Point-of-Failure. *Environ. Res. Lett.* **2017**, *12*, 064004.
(21) Katz, D. L.; Tek, M. R. Overview on Underground Storage of Natural Gas. *J. Pet. Technol.* **1981**, *33*, 943.
(22) Schultz, R. A.; Hubbard, D. W.; Evans, D. J.; Savage, S. L. Characterization of Historical Methane Occurrence Frequencies from U.S. Underground Natural Gas Storage Facilities with Implications for Risk Management, Operations, and Regulatory Policy. *Risk Anal.* **2020**, *40*, 588.
(23) Subramanian, R.; Williams, L. L.; Vaughn, T. L.; Zimmerle, D.; Roscioli, J. R.; Herndon, S. C.; Yacovitch, T. I.; Floerchinger, C.; Tkacik, D. S.; Mitchell, A. L.; Sullivan, M. R.; Dallmann, T. R.; Robinson, A. L. Methane Emissions from Natural Gas Compressor Stations in the Transmission and Storage Sector: Measurements and Comparisons with the EPA Greenhouse Gas Reporting Program Protocol. *Environ. Sci. Technol.* **2015**, *49*, 3252−3261.
(24) Zimmerle, D. J.; Williams, L. L.; Vaughn, T. L.; Quinn, C.; Subramanian, R.; Duggan, G. P.; Willson, B.; Opsomer, J. D.; Marchese, A. J.; Martinez, D. M.; Robinson, A. L. Methane Emissions from the Natural Gas Transmission and Storage System in the United States. *Environ. Sci. Technol.* **2015**, *49*, 9374−9383.
(25) Mehrotra, S.; Faloona, I.; Suard, M.; Conley, S.; Fischer, M. L. Airborne Methane Emission Measurements for Selected Oil and Gas Facilities Across California. *Environ. Sci. Technol.* **2017**, *51*, 12981−12987.
(26) Thorpe, A. K.; et al. Methane Emissions from Underground Gas Storage in California. *Environ. Res. Lett.* **2020**, *15*, 045004.
(27) Coburn, S.; Alden, C. B.; Wright, R.; Cossel, K.; Baumann, E.; Truong, G.-W.; Giorgetta, F.; Sweeney, C.; Newbury, N. R.; Prasad, K.; Coddington, I.; Rieker, G. B. Regional Trace-Gas Source Attribution Using a Field-Deployed Dual Frequency Comb Spectrometer. *Optica* **2018**, *5*, 320.
(28) Alden, C. B.; Ghosh, S.; Coburn, S.; Sweeney, C.; Karion, A.; Wright, R.; Coddington, I.; Rieker, G. B.; Prasad, K. Bootstrap Inversion Technique for Atmospheric Trace Gas Source Detection and Quantification Using Long Open-Path Laser Measurements. *Atmos. Meas. Tech.* **2018**, *11*, 1565−1582.
(29) Alden, C. B.; Coburn, S. C.; Wright, R. J.; Baumann, E.; Cossel, K.; Perez, E.; Hoenig, E.; Prasad, K.; Coddington, I.; Rieker, G. B. Single-Blind Quantification of Natural Gas Leaks from 1 Km Distance Using Frequency Combs. *Environ. Sci. Technol.* **2019**, *53*, 2908−2917.
(30) Conley, S.; Faloona, I.; Mehrotra, S.; Suard, M.; Lenschow, D. H.; Sweeney, C.; Herndon, S.; Schwietzke, S.; Pétron, G.; Pifer, J.; Kort, E. A.; Schnell, R. Application of Gauss's Theorem to Quantify Localized Surface Emissions from Airborne Measurements of Wind and Trace Gases. *Atmos. Meas. Tech.* **2017**, *10*, 3345−3358.
(31) Coddington, I.; Newbury, N.; Swann, W. Dual-Comb Spectroscopy. *Optica* **2016**, *3*, 414−426.
(32) Waxman, E. M.; Cossel, K. C.; Truong, G.-W.; Giorgetta, F. R.; Swann, W. C.; Coburn, S.; Wright, R. J.; Rieker, G. B.; Coddington, I.; Newbury, N. R. Intercomparison of Open-Path Trace Gas Measurements with Two Dual Frequency Comb Spectrometers. *Atmos. Meas. Tech.* **2017**, *10*, 3295−3311.
(33) Coddington, I.; Newbury, N.; Swann, W. Dual-Comb Spectroscopy. *Optica* **2016**, *3*, 414−426.
(34) Coburn, S.; Alden, C. B.; Wright, R.; Wendland, G.; Rybchuk, A.; Seitz, N.; Coddington, I.; Rieker, G. B. Long Distance Continuous Methane Emissions Monitoring with Dual Frequency Comb Spectroscopy: Deployment and Blind Testing in Complex Emissions Scenarios. **2020**, arXiv:physics/2009.10853. https://arxiv.org/ftp/arxiv/papers/2009/2009.10853.pdf.
(35) Conley, S. A.; Faloona, I. C.; Lenschow, D. H.; Karion, A.; Sweeney, C. A Low-Cost System for Measuring Horizontal Winds from Single-Engine Aircraft. *J. Atmos. Ocean. Technol.* **2014**, *31*, 1312−1320.
(36) Caputi, S. D. Meteorological Conditions Surrounding California's Central Valley High Ozone Events: An Integrative Approach. Ph.D. Dissertation, University of California Davis, 2019.
(37) Dlugokencky, E. J. NOAA/ESRL. Www.Esrl.Noaa.Gov/Gmd/Ccgg/Trends_ch4/ (accessed February 1, 2020).
(38) Johnson, D. R.; Covington, A. N.; Clark, N. N. Methane Emissions from Leak and Loss Audits of Natural Gas Compressor Stations and Storage Facilities. *Environ. Sci. Technol.* **2015**, *49*, 8132−8138.

https://dx.doi.org/10.1021/acs.est.0c03175
Environ. Sci. Technol. 2020, 54, 14589−14597

Environmental Science & Technology

Article

Cite This: Environ. Sci. Technol. 2019, 53, 2908−2917

pubs.acs.org/est

Single-Blind Quantification of Natural Gas Leaks from 1 km Distance Using Frequency Combs

Caroline B. Alden,*[,‡,†] Sean C. Coburn,[‡] Robert J. Wright,[‡] Esther Baumann,[§] Kevin Cossel,[§] Edgar Perez,[§] Eli Hoenig,[§] Kuldeep Prasad,[⊥] Ian Coddington,[§] and Gregory B. Rieker[‡]

[‡]Precision Laser Diagnostics Laboratory and [†]Cooperative Institute for Research in Environmental Sciences, University of Colorado Boulder, Boulder, Colorado 80309, United States

[§]National Institute of Standards and Technology, Boulder, Colorado 80305, United States

[⊥]National Institute of Standards and Technology, Gaithersburg, Maryland 20899, United States

Supporting Information

ABSTRACT: A new method is tested in a single-blind study for detection, attribution, and quantification of methane emissions from the natural gas supply chain, which contribute substantially to annual U.S. emissions. The monitoring approach couples atmospheric methane concentration measurements from an open-path dual frequency comb laser spectrometer with meteorological data in an inversion to characterize emissions. During single-blind testing, the spectrometer is placed >1 km from decommissioned natural gas equipment configured with intentional leaks of controllable rate. Single, steady emissions ranging from 0 to 10.7 g min^{-1} (0−34.7 scfh) are detected, located, and quantified at three gas pads of varying size and complexity. The system detects 100% of leaks, including leaks as small as 0.96 g min^{-1} (3.1 scfh). It attributes leaks to the correct pad or equipment group (tank battery, separator battery, wellhead battery) 100% of the time and to the correct equipment (specific separator, tank, or wellhead) 67% of the time. All leaks are quantified to within 3.7 g min^{-1} (12 scfh); 94% are quantified to within 2.8 g min^{-1} (9 scfh). These tests are an important initial demonstration of the methodology's viability for continuous monitoring of large regions, with extension to other trace gases and industries.

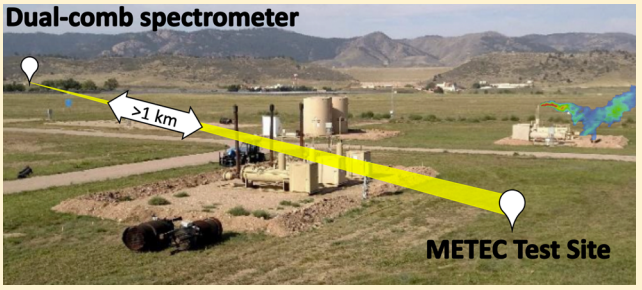

1. INTRODUCTION

A number of scientific and industrial fields require more accurate, rapid, and/or continuous monitoring of airborne constituents with environmental, chemical, biological, and health-and-safety impacts. For example, recent increases in natural gas production in the United States[1] have led to a parallel increase in attention from researchers, policymakers, and industry on methane and volatile organic compound emissions from this sector and the efficacy of current mitigation activities.[2,3] Past measurements of methane emissions from the oil and gas sector suggest a so-called "fat-tailed" distribution: a few large, and possibly intermittent, sources account for a large proportion of total emissions.[4,5] Approaches to monitoring that are continuous in time and regional in coverage are therefore critically important for detection and mitigation of the biggest emitters.[3] Current leak detection and repair (LDAR) practices, however, consist of "snapshots" in time of emissions using an infrared camera: a practice that is known to have high levels of uncertainty,[6] is not amenable to continuous monitoring, and cannot itself yield estimates of leak rates. These findings have led to efforts to create new technologies, particularly with continuous monitoring capabilities, for detection and mitigation of emissions from oil and gas production, distribution, and storage.[7]

This study examines the technical effectiveness of dual frequency comb spectroscopy (DCS) with atmospheric inversions for continuous monitoring (including detection, attribution, and quantification) of trace gas emissions, such as those from natural gas production and storage. We use a DCS observing system,[8−10] which emits and detects light in the near-infrared, to monitor methane emissions from a distance of more than 1 km. Measurements made with the DCS instrument are ingested into an atmospheric inverse model that estimates the presence or absence of a leak, the leak location, and the leak rate.[10,11] Deployment of the system for the monitoring of real oil and gas production equipment and facilities would leverage the ability to monitor many pads and equipment groups/batteries within the laser beam radius (Figure 1). The approach to methane monitoring shown here would not only solve problems of temporal and spatial

Received: November 7, 2018
Revised: January 20, 2019
Accepted: January 29, 2019
Published: January 29, 2019

DOI: 10.1021/acs.est.8b06259
Environ. Sci. Technol. 2019, 53, 2908−2917

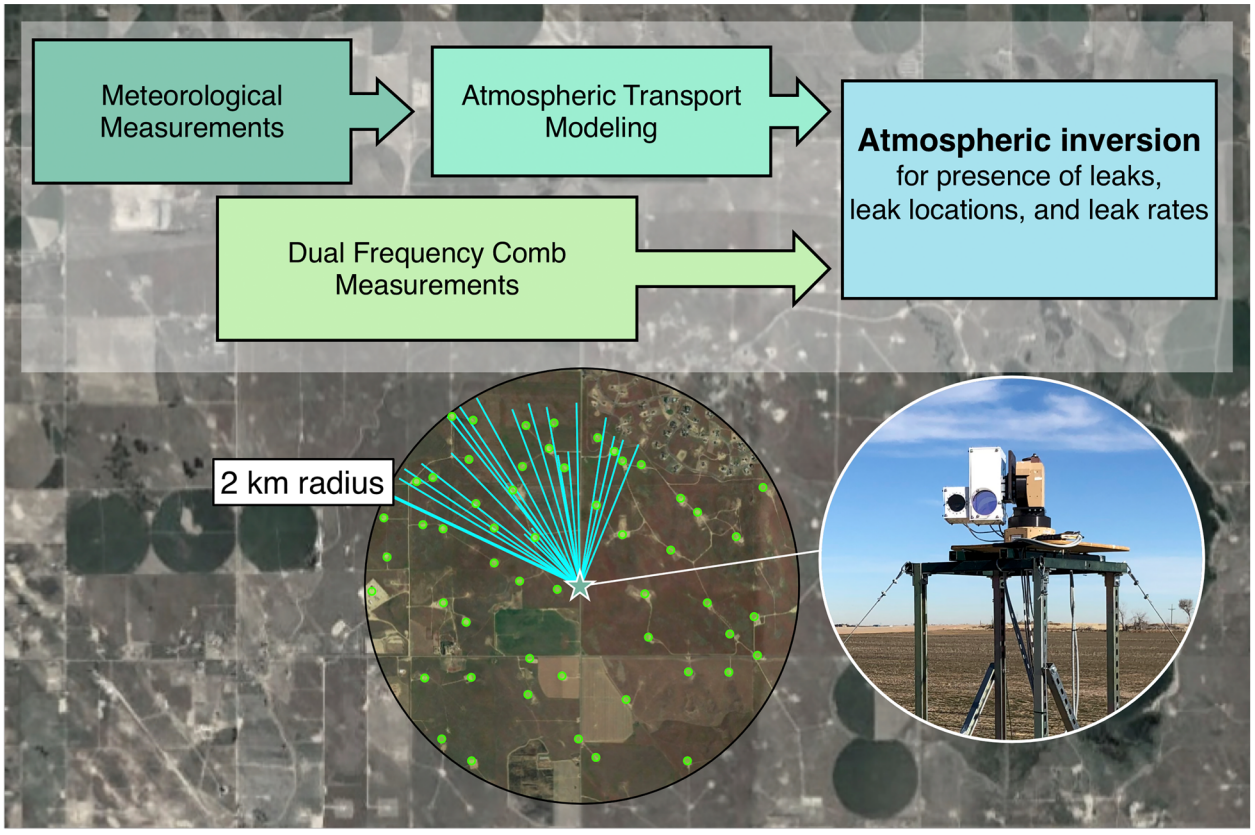

Figure 1. Schematic showing idealized deployment of dual frequency comb spectrometer (teal star) for monitoring of real oil and gas facilities (green circles) within a 2-km radius. Cyan lines demonstrate how rotation of the telescope head allows for querying of different beam paths within the monitoring area, and shorter beam paths allow characterization of near-field sites. Boxes demonstrate flow of data collection and analysis. The map shows oil and gas facilities in the Denver Julesburg basin of Colorado. The inset photo shows the laser terminal head and telescope operating in the field. Map data: Google.

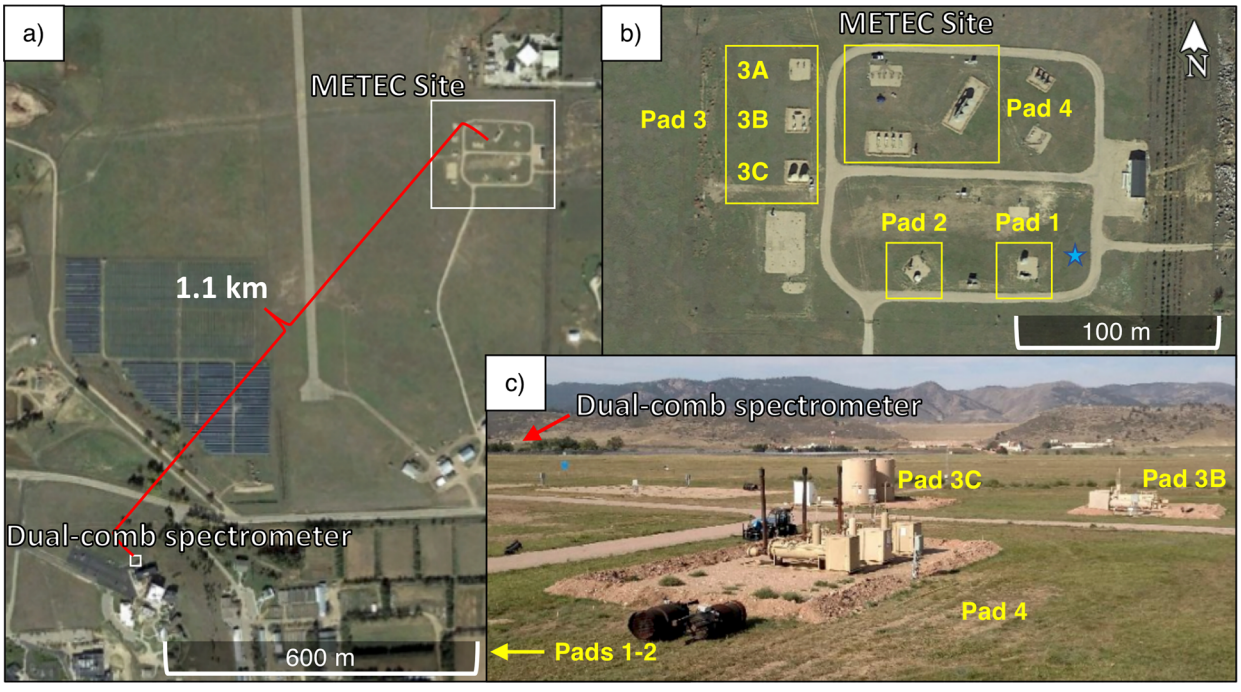

Figure 2. (a) Aerial view of METEC site and Mobile Lab with dual-comb spectrometer (DCS) > 1 km away to the SW. (b) Detailed aerial view of METEC site and pads 1, 2, and 3, as well as batteries 3A, 3B, and 3C. The blue star in panel (b) shows the location of the sonic anemometer. (c) View from the center of the METEC test site to the west-southwest, toward the Mobile Lab with DCS. Pad 4, visible in panel (c),was not used in single-blind testing. Map data: Google.

DOI: 10.1021/acs.est.8b06259
Environ. Sci. Technol. 2019, 53, 2908−2917

coverage, but it is also viable for practical LDAR use because of its potential to offer reduced cost and increased efficiency of leak determination, given its regional scale.

We test the observing system and inversion in a single-blind pilot study at the Methane Emissions Technology Evaluation Center (METEC)[12] at Colorado State University in Fort Collins, Colorado, over the course of 3 weeks in August and September 2017. We examine the system's capabilities for pad-level or battery-level (i.e., smaller natural gas pads or separate batteries of equipment on larger natural gas pads) as well as equipment-level (i.e., wellhead, separator, or tank on a single gas pad) emissions monitoring. In this paper, battery refers to a group of like equipment placed close together. We discuss how these single-blind tests offer a first step in validating the capabilities of the system in the context of monitoring needs along the oil and gas supply chain. The technology and methodologies presented here are readily adaptable to other types of monitoring needs.

2. MATERIALS AND METHODS

We combine atmospheric measurements of methane with inverse methods to estimate emissions from the locations of interest, which range from equipment-scale to pad-scale. We employ a dual frequency comb spectrometer as our measurement platform, which allows for high-precision[8−10] (ppb·km) measurements of methane gas over long (>1 km) open paths through the atmosphere. Beam paths are sampled between the DCS location and retroreflective mirrors stationed on tripods in the field of monitored facilities, enabling the determination of path-integrated atmospheric methane concentrations. The DCS transceiver (beam pitch/catch optics) is located on a rotating and tilting gimbal, so that multiple different beam paths were measured in sequence with a single instrument.

At the METEC test facility, the DCS system was located 1.1 km southwest of the test site (Figure 2a), and laser beams extended to retroreflectors placed on the METEC site (Figure 2b). While it would have been possible to station the DCS closer to the METEC test site, which could have enhanced the observed signals and enable greater certainty in leak detection, we chose instead to situate the DCS far from the site; situating the DCS further away allowed these tests to more closely mimic the deployment scenario in which many sites can be monitored across a region with a single instrument (e.g., Figure 1). In that scenario, emissions characterization is best suited for scales of equipment batteries or pads.

2.1. Dual Frequency Comb Spectrometer as a Measurement Platform. Dual frequency comb spectroscopy is a unique form of laser-based trace gas sensing that combines high spectral resolution and broad spectral coverage.[13] These capabilities enable precise and calibration-free measurements of multiple species simultaneously, which in turn reduces the influence of absorption and dilution interference among species and leads to high stability.[8,9,11,13,14] Here, for example, atmospheric water vapor is measured simultaneously with methane to enable interference-free, true dry-air mole fractions that correct for changes in water vapor dilution over time.[11] By fitting the hundreds of absorption features from the multiple species that contribute to the broad, high resolution absorption spectrum, it has been shown that stability and excellent agreement (below 0.5% across multiple trace gases) are possible without calibration across multiple DCS instruments.[8] Here, the measured spectra were centered at 1640 nm (7000 cm^{-1}) and spanned a bandwidth of 70 nm (~270 cm^{-1}) with a point spacing of <2 × 10^{-3} nm (0.0067 cm^{-1}).[9] The acquisition rate of a single spectrum was 625 Hz, and the spectra were coherently averaged to yield one high signal-to-noise spectrum every 2 min. The sensitivity to methane gas is on the order of several ppb over 2 min for a ~1-km-long, one-way path (2-km roundtrip), and the beam is eye-safe.

2.2. METEC Test Site and Protocols. We performed the single-blind tests at the Methane Emissions Technology Evaluation Center (METEC) at Colorado State University in Fort Collins, Colorado.[15] The METEC facility has three pads built to simulate those found in natural gas production (Figure 2). Pads 1 and 2 are 10 m × 10 m with a wellhead, separator, and storage tank located on each. Pad 3 is 60 m × 10 m, and has a 10 m × 10 m wellhead battery on the north end with three wellheads, a 10 m × 10 m separator battery in the middle with two separators, and a 10 × 10 m tank battery on the south end with two storage tanks. All equipment is decommissioned, and each piece is plumbed to allow testers to remotely activate natural gas leaks, at known flow rates, at a variety of points on the equipment.[16]

Prior to testing, we were informed by METEC that methane leak rates could vary from 0 to any value. In the single-blind tests, actual emission values ranged from 0 to 10.7 g min^{-1} (0−34.7 standard cubic feet per hour, or scfh) of methane gas. The composition of gas emitted was that of natural gas (see Supporting Information), and we reported rates of methane emissions. Emission rates were continuous throughout the course of each test. The upper limit and range of emission rates chosen by METEC reflected two target goals. First, the METEC testers intended to assign leak rates to components that reflect measured emission rates from like components at operational oil and gas sites.[17−21] Second, the testers chose a maximum limit for emissions that is equal to 5× the target emission rate (6 scfh) established by the ARPA-E MONITOR program,[7,21] which funds the test site and the development of this technology.[7]

Here, we refer to the true controlled emission rates and locations engineered by METEC as the "true" locations and rates (acknowledging that the true rates are not perfectly known and have associated uncertainties). We refer to the values that we estimate using our observing system as the "estimated" locations and rates. Uncertainties in the "true" methane flow rates, as reported to us by METEC, include uncertainty in the mean flow rate and meter reading, uncertainty in corrections that relate calibration of emitted gas to a reference gas, and uncertainty in methane concentration as calculated from repeat gas composition analyses.

The test protocols for the METEC site are for a single-blind study, in which the locations and rates of the true methane emissions are only known by the testers at the Colorado State University Energy Institute, and not by our team of researchers deploying the DCS system and performing the atmospheric inversion modeling. We undertook a total of 18 single-blind tests (6 tests on each pad). Tests were numbered 1−6 at Pad 1, 7−12 at Pad 2, and 13−18 at Pad 3.

In order to retrieve more information about our ability to detect, attribute, and quantify emissions, six additional tests were run in nonblind mode. The METEC facility offers visiting technologies the opportunity to request any rates or locations of emissions, for purposes of gathering additional trial runs of the observing system in this close-to-real-world setting. Because we designed and requested these trials, the DCS

DOI: 10.1021/acs.est.8b06259
Environ. Sci. Technol. 2019, 53, 2908−2917

team had knowledge of the leak rate and location. However, to ensure that the nonblind trials offer meaningful feedback on our observing system capabilities, the data were analyzed following the same inversion protocol applied to the single-blind tests. That is, the six nonblind tests, of which three are from Pad 2 and three are from Pad 3, were treated as if nothing was known a priori about the location or rate of the leak, and the single-blind inversion approach was applied. The results of these additional tests are labeled nonblind (NB) tests 1−6.

In all tests, the beginning and end times of the emissions were known, and the pad (Pad 1, 2 or 3) was also known. The test durations ranged from 3.5 to 4.25 h at Pad 1, from 3.5 to 5.5 h at Pad 2, and from 1.5 to 2 h at Pad 3. We conveyed our results to the METEC testers by means of gridded pad layouts to report leak locations, and tables to report leak rates. The reporting grids were provided to us by METEC. The size of each grid box is 1 foot, in the x, y, and z directions (see Supporting Information for images of the test reporting grid for each pad).

2.3. Data Collection and Data Reduction. To orient the test reporting grids, we determined the locations of potential sources relative to the DCS by using a combination of GPS of the retroreflector locations and pad extents, together with knowledge of the layout of each pad (for example, from freely available satellite imagery). Leak attribution was performed using the known locations of equipment infrastructure (as gathered following the above methods) to generate a map of possible sources, which were then allowed as possible leak locations in the inversion.

The metrics and protocols of testing for Pads 1 and 2 were different for that of Pad 3: at Pads 1 and 2, our goal during each test was to detect, attribute, and quantify emissions at the equipment-level (i.e., identify the specific wellhead, separator or tank that is leaking) on the pad. At Pad 3, our goal during each test was to detect, attribute, and quantify emissions at the pad- or battery-scale (that is, to differentiate the leak location by pad or by equipment group: the wellhead battery, separator battery, or tank battery). The goal for future emissions monitoring in real oil and gas production is most closely mimicked by the tests at Pad 3, although even those tests demonstrated a density of equipment batteries that is high compared with, for example, pad layouts in the Denver Julesburg basin (Figure 1).

The number of beams used in each test scales with the number of areas to be measured, m, where the number of beams is equal to $m + 1$ (see Supporting Information for beam placements). The DCS transceiver rotates to sample each beam path in sequence. For Pads 1 and 2, for example, we sought to attribute the leak to the correct piece of equipment. On those pads, there are three pieces of equipment (one tank, one separator, and one wellhead), so four beams were used. On Pad 3, there are three distinct batteries that were monitored, such that the number of beams, $m + 1$, is equal to 4. Two additional beams were used in tests at Pad 1, although the use of these additional beams was not necessary (see Supporting Information).

In some Pad 3 tests, we also sampled extra beams monitoring Pads 1 and 2 (so that the number of beams used is equal to 6), to simulate a scenario in which multiple pads and batteries are being simultaneously monitored. Continuous monitoring of multiple pads at one time more realistically mimics deployment in areas of oil and gas production (Figure 1). In all tests, sampling occurred in a repeating, sequential pattern (east-to-west), and we set the DCS to query each beam path for 2 min at a time.

The atmospheric methane background, or ambient concentration measured during testing at METEC, is highly variable and similar to that observed in active oil and gas regions. Because emission signals are superimposed upon the background concentration of methane, it was necessary to estimate and subtract an estimate of that value from each measurement to isolate enhancements due to leaks alone. We used the "downwind−upwind" background estimation procedure described in refs 9 and 11, in which beams that are upwind of the potential source location of interest, in a given set of wind conditions, are used to estimate the background methane concentrations for beams downwind.

We measured meteorological conditions using a sonic anemometer placed 2 m above ground level near the southeast corner of the METEC site (Figure 2). We used information about the scalar wind direction and wind speed and stability conditions in a plume model to estimate influence functions describing the relationship between prior leak locations and beam-averaged methane concentrations. Standard practice for filtering of measurements taken during quiescent wind conditions (<1 m s^{-1}) was followed.[22]

We fit emission rates to enhancements of methane above background concentrations for each test to determine leak location and size. Inversions and atmospheric dispersion modeling were performed as described in refs 9 and 11. Dispersion modeling used a Gaussian plume model for a point source, and inversions relied on a least-squares approach.[10,11] The confidence in the leak rate was determined using the bootstrap approach described in ref 11, in which resampling from the residuals of the fit to the data allows for estimation of confidence bounds. For detection of leaks, we used a 95% confidence interval to report the presence or absence of a nonzero emission point (or leak). That is, the reporting of a "positive" emission event was triggered if an emission rate was estimated to be more than 2 standard deviations (of the uncertainty as determined from the bootstrap approach) above zero for a potential source location. Conversely, if the estimated emission rate for a given pad, equipment battery, or piece of equipment was not statistically distinguishable from 0 g min^{-1} at the 95% confidence level, then we classified the detection as negative (no leak).

For tests at Pad 3, an additional step was necessary to first identify the battery that was leaking (wellhead battery, separator battery, or tank battery). In this step, the relative concentrations on each beam were analyzed to determine the likelihood of a leak at each pad. While the goal of leak detection and attribution at Pad 3 was by battery, an equipment-level analysis, as described above, was performed in order to quantify the leak rate.

Quantification of emissions for all tests was performed for the single-blind tests as described here and found in refs 9 and 11. Subsequent to testing, several updates were made to the inversion codes, including correction of an indexing error and treatment of low wind speeds to fit recommendations in the micrometeorological literature (see Supporting Information). The final results shown here were calculated using the code updates. Description of these updates as well as the initially reported (single-blind) quantification results are shown in the Supporting Information.

DOI: 10.1021/acs.est.8b06259
Environ. Sci. Technol. 2019, 53, 2908−2917

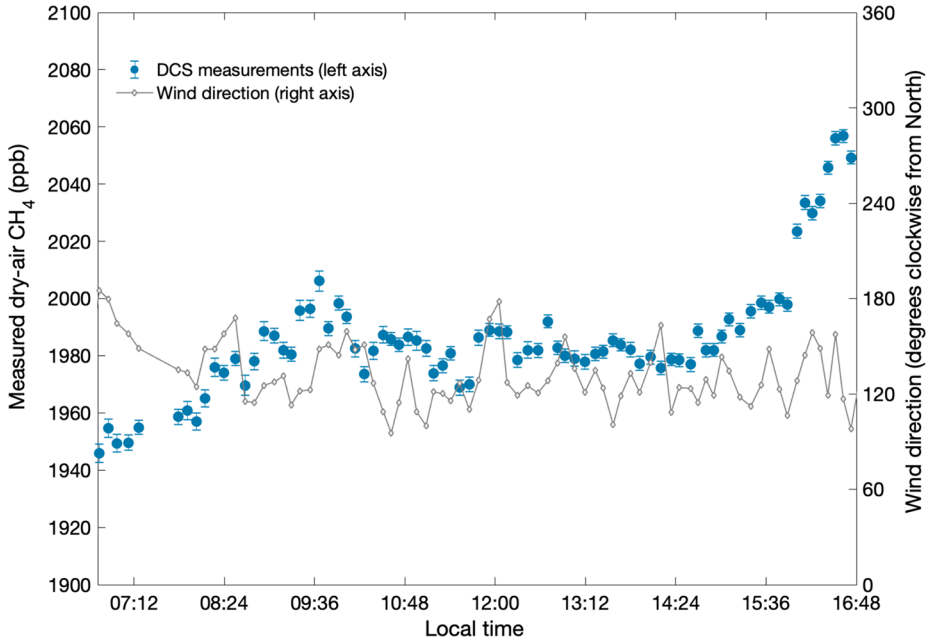

Figure 3. Measured dry-air CH_4 mole fraction (left axis) and wind direction (right axis) during Test 4, during which no controlled emissions were present. In the absence of emissions, the data collected over this 4-h period measured ambient "background" concentrations of methane at the METEC site. Uncertainty bars show the 1-sigma measurement uncertainty.

3. RESULTS AND DISCUSSION

We analyzed the results of the METEC tests using three performance criteria: detection, attribution, and quantification. The first tier of monitoring was detection, or the ability of our monitoring system to identify that a leak was present. Of equal importance for purposes of efficiency in leak detection and repair practices was the ability to identify that a leak was *not* present (that is, to avoid false-positive leak detection). The second tier was attribution, or our ability to determine the location of any leaks detected. Third, we sought to quantify the emission rate of any identified leaks.

3.1. Leak Detection. Of the 18 tests, the controlled emissions for 17 of the tests included a leak rate >0. The no-leak case tests our system's ability to differentiate fluctuations in the ambient atmospheric methane concentrations at the site from the local variability that would arise from a leak. That is, the no-leak test assesses whether our leak detection protocol is robust to instrument noise and atmospheric variability such that an LDAR team would not be dispatched to repair a false emission detection.

Our DCS system was successful in identifying 17 of 17 true leaks, and 1 of 1 no-leak scenarios, resulting in a 100% success rate in leak detection for single-blind leaks that were as small as 0.96 g min^{-1} (3.1 scfh). Additionally, we were successful in detecting the leak in 6 of 6 of the nonblind tests. For reference, it is estimated that 90% of emissions from measured device-level leaks in the oil and gas sector arise from devices with emissions greater than ∼41.7 g min^{-1} (∼135 scfh).[4] This disproportionate contribution of emissions is due to the skewed, heavy-tailed distribution of emissions measured in all source categories.[4] Device-level measurements suggest the fraction total emissions arising from leaks emitting in the range of the controlled release rates tested here (0−10.7 g min^{-1} (0−34.7 scfh) is roughly 0−5%.[4] That is, emissions below and up to the maximum rate tested here are considered small in the oil and gas sector and represent a small fraction of total emissions.[2,3]

The DCS monitoring system successfully detected the single-blind and nonblind leaks against a background ambient methane concentration that varied substantially during testing. For example, during the no-leak test, which in the absence of controlled emissions was equivalent to 4 h of measuring ambient methane conditions, the standard deviation of measurements was 33 ppb, and the measured values ranged from 1946 to 2057 ppb (Figure 3). This range of values was observed without a significant change in the wind direction; in some tests, changing wind directions carried air masses from different source regions, which can lead to additional, rapid shifts in the ambient (background) concentration of methane.

The results show that leak detection was successful even given short test durations (one to 6 h) and consequently low measurement density (average number of 2 min samples, *n*, of 35, with as few as 6 and as many as 92). Overall, we consider all tests to be short in duration compared with anticipated monitoring of real oil and gas operations (because the system is designed to operate continuously and autonomously, monitoring can proceed for periods of days to months or longer). Certain tests contained very low numbers of samples for three reasons: short duration of testing, data loss due to filtering for low wind speeds, and larger number of beams sampled (which reduced the beam revisit rate for a given period of monitoring). For example, nonblind test 6 extended for only 2 h and 46 min, and a series of 7 beams were sampled to simulate the monitoring of 6 individual areas (including equipment batteries and smaller pads). Following filtering for wind conditions for that test, *n* was only 6, yet leak detection was successful, though with slightly higher uncertainty.

3.2. Leak Attribution. *3.2.1. Attribution to Batteries of Equipment and Smaller Pads.* At the battery level (Pad 3), our goal was to identify whether the leak originated at the wellhead battery, the separator battery, or the tank battery. For these equipment battery attribution tests, the correct pad or

DOI: 10.1021/acs.est.8b06259
Environ. Sci. Technol. 2019, 53, 2908−2917

Table 1. Attribution of Emissions at the Equipment Level (Tests 1−12) or Battery Level (Tests 13−18 and NB 1−6) with Locations That Are Estimated Correctly (Incorrectly) Colored Blue (Yellow)

Test ID	Pad	True Location	Estimated Location	*n* number of samples
1	1	wellhead	wellhead	69
2	1	separator	separator	40
3	1	separator	wellhead	42
4	1	no leak	no leak	58
5	1	tank	separator	53
6	1	tank	separator	31
7	2	wellhead	wellhead	35
8	2	wellhead	wellhead	32
9	2	wellhead	wellhead	56
10	2	separator	separator	49
11	2	separator	separator	46
12	2	tank	tank	44
13	3	wellhead battery	wellhead battery	9
14	3	wellhead battery	wellhead battery	12
15	3	separator battery	separator battery	13
16	3	separator battery	separator battery	21
17	3	tank battery	tank battery	29
18	3	tank battery	tank battery	29
NB1	2	tank	tank	92
NB2	2	wellhead	wellhead	30
NB3	2	separator	separator	34
NB4	3	separator battery	separator battery	9
NB5	3	tank battery	tank battery	12
NB6	3	wellhead battery	wellhead battery	6

battery was successfully identified in all cases (Table 1). Of the three battery-level nonblind tests (NB4, NB5 and NB6), we also successfully attributed each leak to the correct battery on Pad 3 (separator battery, tank battery, and wellhead battery, respectively). As for smaller pads (for the tests at Pads 1 and 2), the pad from which the emission point would originate was communicated to testers beforehand, such that leak attribution was binary: either a leak was present or no leak was present (which was successful in all cases, as described in Section 3.1).

The results of these tests indicate that attribution of emissions at the battery level can be done with high confidence, given the number of samples, sampling time, and meteorological conditions experienced during testing.

3.2.2. Attribution to Specific Pieces of Equipment. We sought to attribute leaks at the equipment level (discerning whether the leak was from the wellhead, separator, or tank on a single pad) for the tests conducted at Pads 1 and 2. Leak attribution to the correct piece of equipment was successful in all tests at Pad 2 (Table 1). In the three nonblind tests conducted at Pad 2 (NB1, NB2, and NB3), we were also successful 100% of the time at attributing the leak to the correct piece of equipment (tank, wellhead, and separator, respectively).

We attributed the leak to the correct piece of equipment in two cases at Pad 1 (Table 1). In tests 1 and 2, the wellhead and separator, respectively, were accurately determined as the source locations. However, in test 3, the leak was attributed to the wellhead, whereas the true leak location was the separator and in tests 5 and 6, the leak was attributed to the separator, whereas the true leak location was the tank. In test 4, no leak was present (no attribution was therefore necessary).

Attribution of emissions at the equipment-level may be dependent upon the orientation of the equipment on the pad with respect to the DCS. A favorable orientation (in which line-of-sight from the DCS between different pieces of equipment is possible) can lead to a high success rate (100% at Pad 2) of leak attribution. If this condition is not in place, however, then leak attribution at the equipment-level appears to be less consistent, at least under the conditions of these tests. This condition is not an issue at the battery- or pad-scales. Longer testing times and/or different wind conditions could improve attribution in the case of Pad 1.

3.3. Leak Quantification. Leak quantification was defined as the estimation of the flow rate of the leak or emission. While emission rates were randomly assigned by the METEC testers, the target range of emission rates, described in Section 2.2, was set to the original goals of the Department of Energy Advanced Research Projects Agency Energy (DOE ARPA-E) MONITOR program. The goal is emissions quantification for leaks as small as 1.9 g min^{-1} (6 scfh),[7] which is on the order of magnitude expected from "normal" natural gas operations (that is, emissions well below the so-called "super-emitter" level).[17−21] For comparison (and as stated previously), device-level measurements of leaks across the natural gas supply chain suggest that most emissions (90%) come from

DOI: 10.1021/acs.est.8b06259
Environ. Sci. Technol. 2019, 53, 2908−2917

devices with emissions that are in excess of ~41.7 g min^{-1} (~135 scfh).[4]

The majority (10 of 18 tests) of leak rates in the single-blind tests were below 3.1 g min^{-1} (10 scfh or 3.1 g min^{-1}). Of those tests, 4 were below 1.9 g min^{-1} (6 scfh), which is roughly the average literature-reported emission rate from pneumatic controllers found on well pads.[5,20] The largest true leak rate during single-blind testing was an emission of 10.7 g min^{-1} (34.7 scfh) from the separator on Pad 1, although several larger emissions were assessed during nonblind testing (up to 12.4 g min^{-1} or 40 scfh).

We correctly estimated all leaks to within 3.7 g min^{-1} (12 scfh), including the 17 single-blind tests (and one test in which we successfully identified the leak rate as not distinguishable from 0 g min^{-1}) and all of the six nonblind tests (Figure 4). Of the 24 total tests, 17 were quantified to within 1.9 g min^{-1} (6 scfh) or less, and 12 were quantified to within 0.9 g min^{-1} (3 scfh). In terms of percent deviation of the estimated emission rates from the true emission rates, the mean absolute deviation of all estimated emissions from the true emissions was 27%. All estimated emissions (including nonblind) were quantified to within 160%, 20 of the 24 tests were quantified to within 50%, 15 were quantified to within 25%, and half of all tests were quantified to within 10% of the true emission rate. Histograms showing the distribution of the deviations of our estimated rates from the true rates are centered around zero, suggesting that there is not a systematic bias in our quantification of emissions (Figure 5).

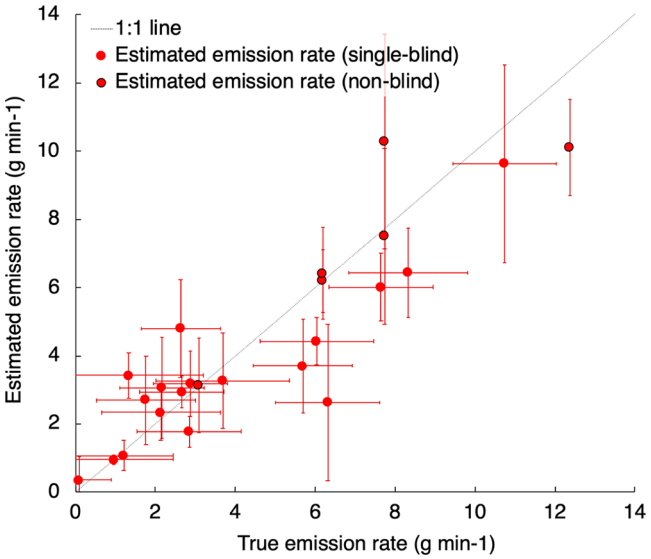

Figure 4. Scatter plot showing the estimated emission rates with 2-sigma uncertainties on the *y*-axis and the true emission rates with 2-sigma uncertainties on the *x*-axis (nonblind tests rate uncertainties were not reported to us by METEC and so are unknown). Red circles with no border denote single-blind tests, and red circles with black border denote nonblind tests.

The only test for which our quantification of emissions differed by more than 2.8 g min^{-1} (9 scfh) from the true emission rate was test 14, during which the true leak rate was 6.3 g min^{-1} (20.4 scfh) and the true leak location was the east wellhead on Pad 3A. The mean wind direction during this test was 154° (clockwise from the north). The retroreflector downwind of Pad 3A during this test did not extend far enough to intersect the entire plume (see Supporting Information), which we hypothesize maximized potential transport errors and led to increased difficulty in rate quantification.

No clear relationships are evident between deviations of estimated from true leak rates and the following variables: atmospheric stability class, variability in wind direction during the test (as estimated by the circular standard deviation of wind direction), time duration of test, or number of samples, *n* (see Supporting Information). The duration of testing may have been too short in the tests performed here, however, for relationships between deviation from the true leak rate and these variables to emerge.

The finding that our system can detect even very small emissions from a distance of >1 km suggests that our approach is promising for the purposes of both monitoring of emissions and observing and estimating the profile of emissions across the natural gas supply chain. In tests with small emissions, small atmospheric enhancements must be identified, which requires high measurement precision. For example, the true emission rate for Test 10 at Pad 2 was 1.2 g min^{-1} (3.9 scfh), resulting in path-average atmospheric enhancements of

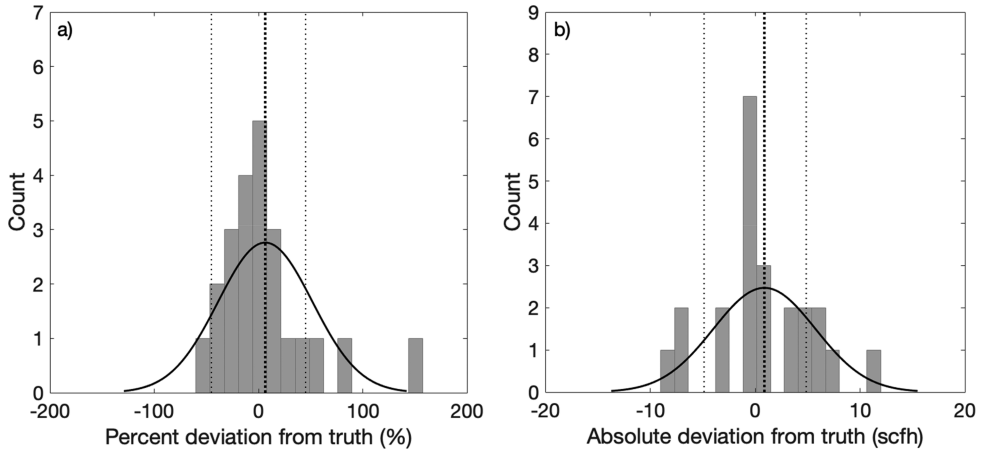

Figure 5. Histograms showing deviation of the estimated emission rate from the true emission rate (estimated−true), in terms of percent (a) and absolute value (b), for the 23 single-blind and nonblind tests for which emissions were nonzero. Solid black lines show normal density functions fitted to each histogram; dark dashed lines show the mean (6.5% and 0.9 scfh, respectively) and light dashed lines show the standard deviation (45.8% and 4.9 scfh, respectively) of each fit.

DOI: 10.1021/acs.est.8b06259
Environ. Sci. Technol. 2019, 53, 2908−2917

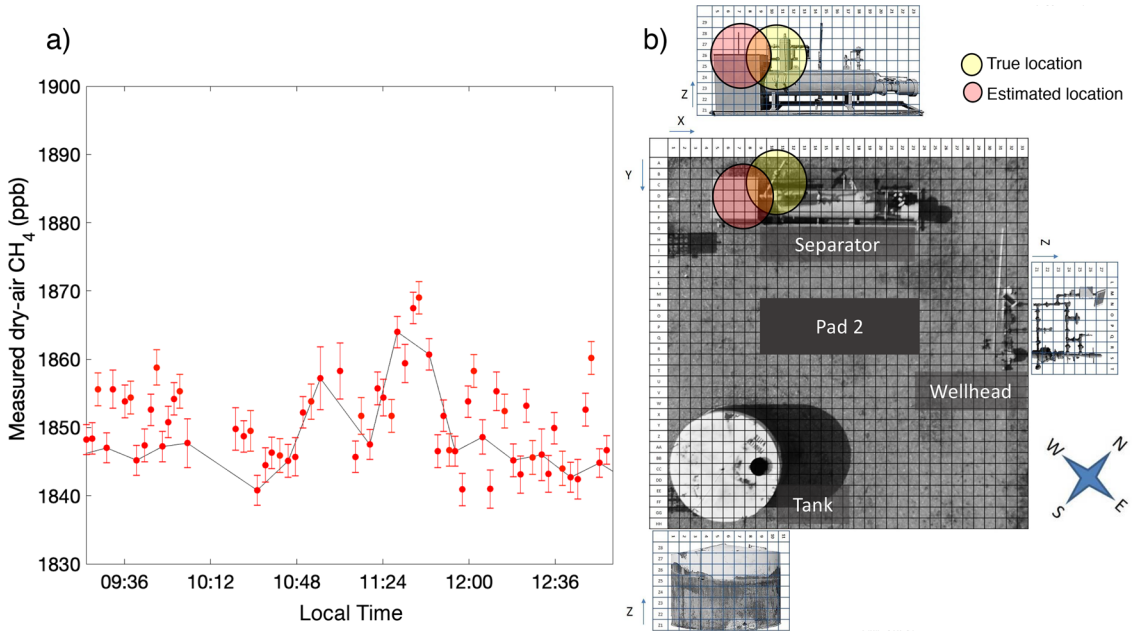

Figure 6. Atmospheric measurements with 1-sigma uncertainty (a) and attribution results (b) for Test 10. Panel (a) shows dual frequency comb measurements (red points) with estimate of background methane concentrations (black line). The grid sizes in panel (b) are 1 foot in the *x*, *y*, and *z* dimensions. Image of test reporting grid adapted, with permission, from METEC.

methane of 3.1 ± 5.5 ppb above a variable background (Figure 6). Detection of such a small enhancement requires very high instrument stability and precision; the mean 1-sigma DCS measurement uncertainty during this test was 2.5 ppb. We find that not only was leak detection for this test successful, but the leak was also correctly attributed to the southwestern half of the separator, and the leak was accurately quantified to 10% of the true leak rate: we estimated an emission rate of 1.1 g min^{-1} (3.5 scfh) compared with the true leak rate of 1.2 g min^{-1} (3.9 scfh).

3.4. Scaling and Future Prospects. This study demonstrates an important first step in demonstrating the viability of dual frequency comb spectroscopy with atmospheric inversions to reliably detect methane leaks in a quasi-realistic simulation of emissions from oil and natural gas production from a distance of 1 km. In these tests, we assessed the system's ability to detect, attribute, and quantify emissions. We found that the observing system offers very high fidelity of leak detection, with a 100% success rate in the 18 single-blind and 6 nonblind tests performed at METEC. Leak attribution was very consistent at the pad and battery level. Leak attribution could also be consistently done at the equipment level, provided more than two beams per pad were used, and that the spatial orientation of the equipment on the pad was favorable with respect to the orientation of the DCS. These tests also demonstrate a high degree of fidelity in the quantification of emissions across a variety of sizes, and down to very small leak rates (less than 1.9 g min^{-1} or 6 scfh).

The size of the leaks tested at the METEC test site demonstrates the viability of this method for two important purposes. First, for purposes of mitigation of methane emissions from oil and gas operations, these results demonstrate that our methodology is adequate to address the vast majority of emissions, including very small leaks. Device-level measurements suggest that mitigation of leaks larger than 41.2 g min^{-1} (135 scfh), or more than 43 times larger than the smallest emissions quantified here (and more than 3 times larger than the largest emissions quantified here), would account for 90% of all emissions from oil and gas.[9,11] Second, for purposes of emissions inventories and characterizing the profile of emissions from oil and gas, the granularity of information made available by this approach, combined with its ability to monitor many facilities continuously through time, is not currently available through other approaches. Critical to both mitigation and sector-wide emissions estimation purposes is the ability of the DCS system to provide long-term, continuous, and regional data streams.

The current study represents an important first step in single-blinded validation of the monitoring approach. In addition to the strengths of the METEC tests, including the use of real oil and gas equipment and the testing of small emissions, several limitations apply to extension of the conclusions drawn here to operational oil and gas settings. First, the number of no-leak tests is one, a sample size that is too low for establishing confidence in the ability of the system to avoid false-positive detections. However, several recent publications describe additional field tests with the same system that demonstrate the viability of the system in terms of false detection avoidance.[10,11] A second limitation of the tests described here is that the continuity of emissions is steady, whereas some emissions from oil and gas operations are observed to be intermittent.[19,20] A second round of testing, in which intermittent emissions were included, has been performed at the METEC site, and those results (as well as results from on-site measurements at active oil and gas operations) will be published in a follow-on study.[24] A third limitation of the testing described here is that the start and end times of the emissions were provided by METEC to the DCS team (which would not occur in a real-world monitoring scenario). We point to a series of additional, nonblinded field tests of the monitoring system in which the start and stop times were treated as unknown, and that were successful in identifying the onset and end of emissions, as well as their rates.[9] A fourth potential limitation of the tests described here

DOI: 10.1021/acs.est.8b06259
Environ. Sci. Technol. 2019, 53, 2908−2917

is that only one emission occured at one time, when in reality, multiple emissions may arise from a single piece or grouping of equipment. We address this caveat by pointing to a recent field study in which multiple, simultaneous emissions were successfully characterized,[9] and to the second, follow-on round of single-blind field tests at METEC that included multiple emissions.[24] A final limitation of these tests is that they were of short duration compared with what would take place in a real-world monitoring scenario. Because of this limitation, only a narrow range of wind conditions occurred during each test (see Supporting Information for wind conditions during testing).

The system can be operated autonomously and at a low cost, making this option an efficient and cost-effective solution to emissions monitoring and characterization. For some current regulations (for example, EPA), a technology (or alternative work practice) is considered equivalent to currently accepted LDAR techniques (or current work practice) if the emission reduction attained is equal to or greater than current work practice over a given period of time. For operations with regulations requiring regular site visits to check for leaks, and given the fat-tailed distribution of large and potentially intermittent emissions,[3−5] it is likely that continuous and regional emissions monitoring can improve upon cost effectiveness of current work practice for achieving equal or greater emission reductions. Recent studies assessing the effectiveness of the use of optical gas imaging technologies make this potentiality particularly relevant.[25,26] Furthermore, a large proportion of sites have negligible emissions,[4] such that site visits to look for leaks following the current work practice is neither resource nor cost efficient compared with what a stand-off regional survey could provide. A more thorough economic and cost comparison analysis will be undertaken in a future study employing, for example, the FEAST model.[27]

We find that this technology is a promising, powerful tool for emissions monitoring and quantification. These tests suggest the system could fill critical temporal continuity and regional coverage gaps in the current methane monitoring infrastructure.[3] The DCS technology and inversion framework are highly adaptable to emissions of gases other than methane; dual frequency comb spectroscopy is sensitive to any gases for which distinct absorption features are evident within the system wavelength range. Similarly, the inversion modeling presented here can be adapted to other conserved or nonconserved species. The monitoring approach offers more than a binary detector—it offers the capability to identify leak origins and rates across large areas (multiple square km), with rapidness and efficiency. Further, this approach is configurable to provide the different levels of granularity: from a binary, yes−no leak detector, to a localization scheme that can attribute emissions to pads or in certain circumstances, individual pieces of equipment.

This study contributes an important initial single-blind validation of a novel methane monitoring approach. These tests pave the way for continued development of the observing system, and lay the groundwork for higher complexity testing (to resolve some of the noted limitations of the testing described here), and, ultimately, for testing in operational environments side-by-side with current work practice LDAR teams. The tests described here are demonstrative of the technology in a simple but realistic application and, as such, an important first step toward real-world oil and gas monitoring.

■ ASSOCIATED CONTENT

Supporting Information

The Supporting Information is available free of charge on the ACS Publications website at DOI: 10.1021/acs.est.8b06259.

Figures S1−S15, Tables S1−S2 (PDF)

■ AUTHOR INFORMATION

Corresponding Author

*E-mail: caroline.alden@colorado.edu.

ORCID

Caroline B. Alden: 0000-0002-5249-7800

Funding

Funding for this work comes from Advanced Research Projects Agency-Energy (ARPA-E) (DE-AR0000539); Office of Fossil Energy (DE- FE0029168); Defense Advanced Research Projects Agency (DARPA); National Institute of Standards and Technology (NIST).

Notes

The authors declare no competing financial interest.

■ ACKNOWLEDGMENTS

The authors wish to thank the METEC test site managers and engineers.

■ REFERENCES

(1) Inventory of U.S. *Greenhouse Gas Emissions and Sinks: 1990−2016*; EPA 430-R-18−003; EPA, 2018.

(2) Ravikumar, A. P.; Brandt, A. R. Designing Better Methane Mitigation Policies: The Challenge of Distributed Small Sources in the Natural Gas Sector. *Environ. Res. Lett.* **2017**, *12* (4), 044023.

(3) National Academies of Sciences. *Engineering, and Medicine. Improving Characterization of Anthropogenic Methane Emissions in the United States*; National Academies Press: Washington, D.C., 2018. DOI: 10.17226/24987.

(4) Brandt, A. R.; Heath, G. A.; Cooley, D. Methane Leaks from Natural Gas Systems Follow Extreme Distributions. *Environ. Sci. Technol.* **2016**, *50* (22), 12512−12520.

(5) Zavala-Araiza, D.; Alvarez, R. A.; Lyon, D. R.; Allen, D. T.; Marchese, A. J.; Zimmerle, D. J.; Hamburg, S. P. Super-Emitters in Natural Gas Infrastructure Are Caused by Abnormal Process Conditions. *Nat. Commun.* **2017**, *8*, 14012.

(6) Ravikumar, A. P.; Wang, J.; Brandt, A. R. Are Optical Gas Imaging Technologies Effective For Methane Leak Detection? *Environ. Sci. Technol.* **2017**, *51* (1), 718−724.

(7) ARPA-E Advanced Research Projects-Energy. https://arpa-e.energy.gov/?q=arpa-e-programs/monitor (accessed Jun 6, 2018).

(8) Rieker, G. B.; Giorgetta, F. R.; Swann, W. C.; Kofler, J.; Zolot, A. M.; Sinclair, L. C.; Baumann, E.; Cromer, C.; Petron, G.; Sweeney, C.; Tans, P. P.; Coddington, I.; Newbury, N. R. Frequency-Comb-Based Remote Sensing of Greenhouse Gases over Kilometer Air Paths. *Optica* **2014**, *1* (5), 290−298.

(9) Waxman, E. M.; Cossel, K. C.; Truong, G.-W.; Giorgetta, F. R.; Swann, W. C.; Coburn, S.; Wright, R. J.; Rieker, G. B.; Coddington, I.; Newbury, N. R. Intercomparison of Open-Path Trace Gas Measurements with Two Dual-Frequency-Comb Spectrometers. *Atmos. Meas. Tech.* **2017**, *10* (9), 3295−3311.

(10) Coburn, S.; Alden, C. B.; Wright, R.; Cossel, K.; Baumann, E.; Truong, G.-W.; Giorgetta, F.; Sweeney, C.; Newbury, N. R.; Prasad, K.; Coddington, I.; Rieker, G. B. Regional Trace-Gas Source Attribution Using a Field-Deployed Dual Frequency Comb Spectrometer. *Optica* **2018**, *5* (4), 320.

(11) Alden, C. B.; Ghosh, S.; Coburn, S.; Sweeney, C.; Karion, A.; Wright, R.; Coddington, I.; Rieker, G. B.; Prasad, K. Bootstrap Inversion Technique for Atmospheric Trace Gas Source Detection

and Quantification Using Long Open-Path Laser Measurements. *Atmos. Meas. Tech.* **2018**, *11* (3), 1565−1582.
(12) *ARPA-E | MONITOR Field Test Site* https://arpa-e.energy.gov/?q=slick-sheet-project/monitor-field-test-site (accessed Jan 7, 2019).
(13) Coddington, I.; Newbury, N.; Swann, W. Dual-Comb Spectroscopy. *Optica* **2016**, *3* (4), 414−426.
(14) Truong, G.-W.; Waxman, E. M.; Cossel, K. C.; Baumann, E.; Klose, A.; Giorgetta, F. R.; Swann, W. C.; Newbury, N. R.; Coddington, I. Accurate Frequency Referencing for Fieldable Dual-Comb Spectroscopy. *Opt. Express* **2016**, *24* (26), 30495−30504.
(15) METEC. Energy Institute.
(16) Ravikumar, A. P.; Wang, J.; McGuire, M.; Bell, C. S.; Zimmerle, D.; Brandt, A. R. Good versus Good Enough?" Empirical Tests of Methane Leak Detection Sensitivity of a Commercial Infrared Camera. *Environ. Sci. Technol.* **2018**, *52* (4), 2368−2374.
(17) Bell, C. S.; Vaughn, T. L.; Zimmerle, D.; Herndon, S. C.; Yacovitch, T. I.; Heath, G. A.; Pétron, G.; Edie, R.; Field, R. A.; Murphy, S. M.; et al. Comparison of Methane Emission Estimates from Multiple Measurement Techniques at Natural Gas Production Pads. *Elem Sci. Anth* **2017**, *5* (0), 79.
(18) Vaughn, T. L.; Bell, C. S.; Yacovitch, T. I.; Roscioli, J. R.; Herndon, S. C.; Conley, S.; Schwietzke, S.; Heath, G. A.; Pétron, G.; Zimmerle, D. Comparing Facility-Level Methane Emission Rate Estimates at Natural Gas Gathering and Boosting Stations. *Elem Sci. Anth* **2017**, *5* (0), 71.
(19) Allen, D. T.; Sullivan, D. W.; Zavala-Araiza, D.; Pacsi, A. P.; Harrison, M.; Keen, K.; Fraser, M. P.; Daniel Hill, A.; Lamb, B. K.; Sawyer, R. F.; et al. Methane Emissions from Process Equipment at Natural Gas Production Sites in the United States: Liquid Unloadings. *Environ. Sci. Technol.* **2015**, *49* (1), 641−648.
(20) Allen, D. T.; Pacsi, A. P.; Sullivan, D. W.; Zavala-Araiza, D.; Harrison, M.; Keen, K.; Fraser, M. P.; Daniel Hill, A.; Sawyer, R. F.; Seinfeld, J. H. Methane Emissions from Process Equipment at Natural Gas Production Sites in the United States: Pneumatic Controllers. *Environ. Sci. Technol.* **2015**, *49* (1), 633−640.
(21) Allen, D. T.; Torres, V. M.; Thomas, J.; Sullivan, D. W.; Harrison, M.; Hendler, A.; Herndon, S. C.; Kolb, C. E.; Fraser, M. P.; Hill, A. D.; et al. Measurements of Methane Emissions at Natural Gas Production Sites in the United States. *Proc. Natl. Acad. Sci. U. S. A.* **2013**, *110* (44), 17768−17773.
(22) De Visscher, A. *Air Dispersion Modeling: Foundations and Applications*; John Wiley & Sons: New York, 2013.
(23) Brandt, A. R.; Heath, G. A.; Cooley, D. Methane Leaks from Natural Gas Systems Follow Extreme Distributions. *Environ. Sci. Technol.* **2016**, *50* (22), 12512−12520.
(24) Coburn, S.; Alden, C. B.; Wright, R.; Wendland, G.; Rybchuk, O.; Seitz, N.; Trousdell, J.; Faloona, I.; Coddington, I.; Rieker, G. B. Dual Frequency Comb Measurements of Methane Sources: Complex Emission Testing and Real Natural Gas Infrastructure Monitoring. *Opt. Express*, in preparation.
(25) Ravikumar, A. P.; Wang, J.; Brandt, A. R. Are Optical Gas Imaging Technologies Effective For Methane Leak Detection? *Environ. Sci. Technol.* **2017**, *51* (1), 718−724.
(26) Ravikumar, A. P.; Wang, J.; McGuire, M.; Bell, C. S.; Zimmerle, D.; Brandt, A. R. Good versus Good Enough?" Empirical Tests of Methane Leak Detection Sensitivity of a Commercial Infrared Camera. *Environ. Sci. Technol.* **2018**, *52* (4), 2368−2374.
(27) *FEAST: Fugitive Emissions Abatement Simulation Testbed Monte Carlo Simulation Approach for Evaluating Alternative Work Practices for Equipment Leaks (Report)*; U.S. Environmental Protection Agency; Office of Air and Radiation, Office of Air Quality Planning and Standards: Research Triangle Park, NC, 1999 (accessed Jan 8, 2019).

DOI: 10.1021/acs.est.8b06259
Environ. Sci. Technol. 2019, 53, 2908−2917

Research Article Vol. 5, No. 4 / April 2018 / Optica 320

Regional trace-gas source attribution using a field-deployed dual frequency comb spectrometer

Sean Coburn,[1,*,†] Caroline B. Alden,[1,2,6,†] Robert Wright,[1] Kevin Cossel,[3] Esther Baumann,[3] Gar-Wing Truong,[3] Fabrizio Giorgetta,[3] Colm Sweeney,[2,4] Nathan R. Newbury,[3] Kuldeep Prasad,[5] Ian Coddington,[3] and Gregory B. Rieker[1,7]

[1]Precision Laser Diagnostics Laboratory, University of Colorado Boulder, Boulder, Colorado 80309, USA
[2]Cooperative Institute of Research in Environmental Sciences, Boulder, Colorado 80309, USA
[3]National Institute of Standards and Technology, Boulder, Colorado 80305, USA
[4]National Oceanic and Atmospheric Administration, Boulder, Colorado 80305, USA
[5]National Institute of Standards and Technology, Gaithersburg, Maryland 20899, USA
[6]e-mail: aldenc@colorado.edu
[7]e-mail: greg.rieker@colorado.edu
*Corresponding author: coburns@colorado.edu

Received 9 January 2018; revised 21 February 2018; accepted 22 February 2018 (Doc. ID 319377); published 22 March 2018

Identification and quantification of trace-gas sources is a major challenge for understanding and regulating air quality and greenhouse gas emissions. Current approaches provide either continuous but localized monitoring, or quasi-instantaneous "snapshot-in-time" regional monitoring. There is a need for emissions detection that provides both continuous and regional coverage, because sources and sinks can be episodic and spatially variable. We field deploy a dual frequency comb laser spectrometer for the first time, enabling an observing system that provides continuous detection of trace-gas sources over multiple-square-kilometer regions. Field tests simulating methane emissions from oil and gas production demonstrate detection and quantification of a 1.6 g min^{-1} source (less than the average emissions from a small pneumatic controller) from a distance of 1 km, and the ability to discern two leaks among a field of many potential sources. The technology achieves the goal of detecting, quantifying, and attributing emissions sources continuously through time, over large areas, and at emissions rates ∼1000 × lower than current regional approaches. It therefore provides a useful tool for monitoring and mitigating undesirable sources and closes a major information gap in the atmospheric sciences.

OCIS codes: (010.0280) Remote sensing and sensors; (300.1030) Absorption; (280.1120) Air pollution monitoring.

https://doi.org/10.1364/OPTICA.5.000320

1. INTRODUCTION

Emissions of greenhouse gases and pollutants pose serious risks for global climate change and human health and safety. Regional detection, quantification, and attribution of trace gas sources and sinks is therefore a critical need for a variety of applications, including quantification of emissions in urban or industrial settings for monitoring, reporting, and verification; detection of small amounts of hazardous gases; verification of sub-surface sequestration efforts; and characterization of the exchange of trace gases between the atmosphere and natural or managed ecosystems. For many needs, strictly local and/or strictly time-invariant observational capabilities do not suffice for complete characterization of fluxes. For example, the "snapshots-in-time" provided by aircraft, satellite, or vehicle-mounted point sensor estimations of emissions from oil and gas operations may miss the largest fluxes, which are thought to be highly infrequent [1,2] or may misrepresent fluxes by sampling during midday, when manually triggered (operational) emissions are most frequent [3]. Similarly, regional continuous monitoring can be achieved with networks of point sensors, but the level of detail in the disaggregation of source locations and sizes must necessarily scale with the number of sensors deployed (e.g., [4]), increasing costs and complexity.

Here, we demonstrate a technology capable of continuous monitoring of trace gas fluxes, with the ability to distinguish between emissions sources at fine scales and across large areas and to infer time evolution and variability of individual sources. We present the first remote field deployment of dual frequency comb technology [5,6], coupled with innovations in atmospheric inversion modeling, to enable the continuous detection, location and quantification of small trace gas sources over several square kilometer regions using a single, autonomous instrument. The system consists of the fielded dual frequency comb spectrometer, located in a centralized mobile trailer, which emits a sparse array of kilometer-scale beams strategically located throughout a region

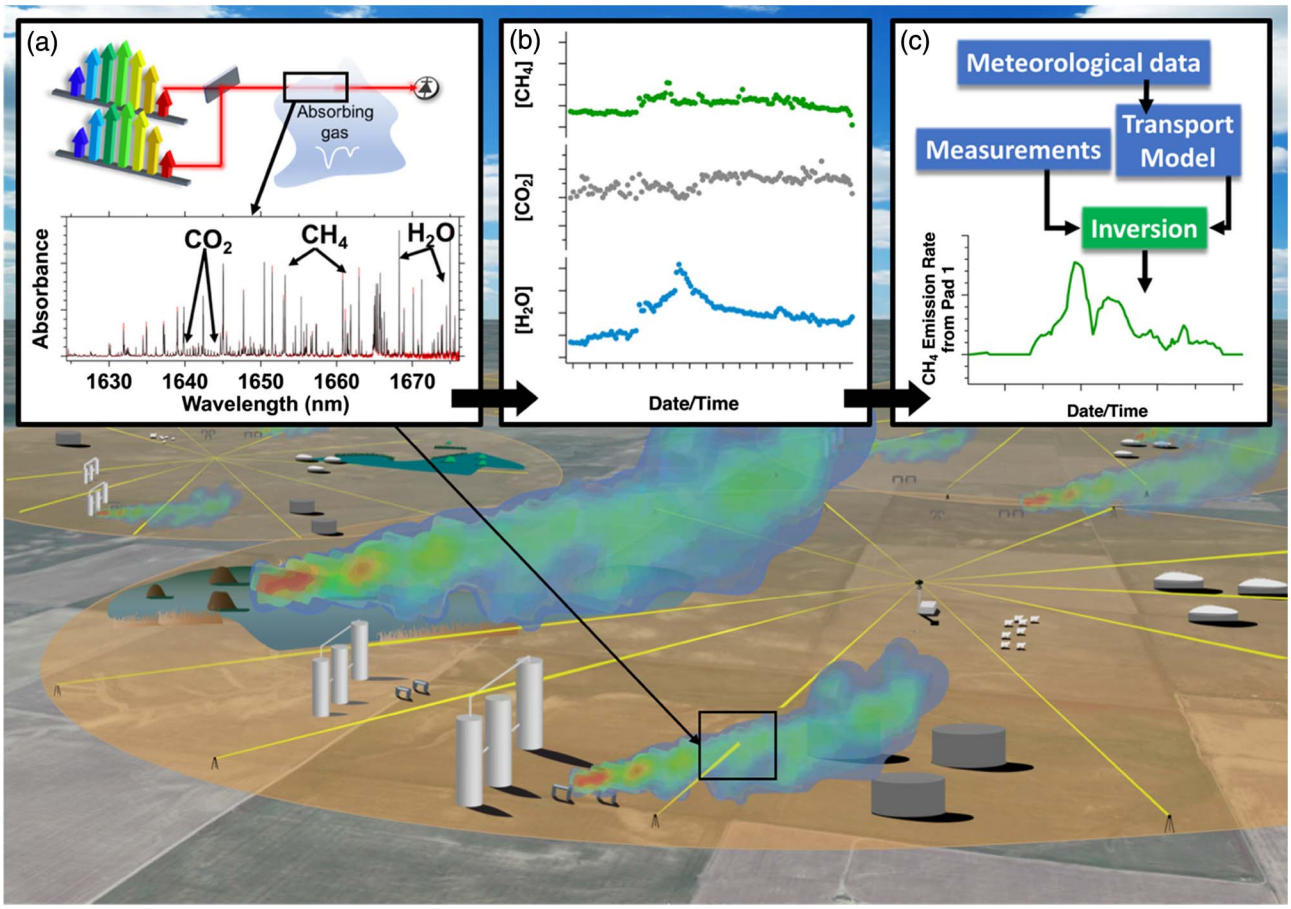

Fig. 1. Regional source monitoring with a centralized DCS. (a) The DCS measures trace gas absorption over an array of long-distance beam paths. (b) Time-resolved trace gas concentrations are determined from fits to the absorption spectra with ppb-km sensitivity and stability. (c) An atmospheric transport model and inversion determines source location and time-resolved emission rate.

of potential emitters to sensitively measure trace gas concentrations over time (see Fig. 1). The measurements are coupled with an atmospheric transport model in a Bayesian inversion to identify sources and quantify the emission rate over time at each source location with several-minute resolution. The laser beam is invisible and eye-safe, and the system can operate continuously day and night except during periods of total optical occlusion (e.g., heavy precipitation). Trace gas sources do not need to be imaged directly, which is important for cases in which line-of-sight from the laser to the source location is blocked by terrain or vegetation. Rather, the sensitivity of the spectrometer enables a sparse beam array that only must intersect the plumes downwind of the sources.

Two field test scenarios utilizing controlled methane emissions are presented here to demonstrate the system's capabilities with respect to two key features for regional trace gas emission characterization: 1) quantification of small, variable-rate gas sources from long distance (>1 km); and 2) identification and quantification of multiple sources within a field of many potential sources. During the first test scenario, we quantify an emission source varying from 1.6 to 8 g min^{-1} over a 24 h period from a distance of >1 km. As a point of reference, the average breathing rate for an adult human can be estimated at ~8 standard liters per minute (slpm, air), compared with volumetric rates ranging from 2.5 to 12 slpm (methane) used for the emission tests in this study. The average reported emissions from pneumatic controllers found on well pads also falls within this range [1,7]. During the second test, we show that the system correctly identifies and quantifies two simultaneous emission sources among an area with up to five potential sources.

2. FIELD-DEPLOYED DUAL-COMB SPECTROMETER

The frequency comb laser is based on Nobel-prize-winning research [8,9] that has significantly impacted the field of molecular spectroscopy [10–12]. The femtosecond pulsed output of a mode-locked frequency comb laser is composed of thousands of perfectly spaced, discrete wavelength elements or "comb teeth," that act as a parallel set of continuous-wave lasers with known frequencies. Dual frequency comb spectroscopy uses two combs with slightly different tooth spacing, mixed on a photodiode after transmission through a sample, to extract high resolution absorption information [13–17,11]. The result is an unprecedented combination of spectral bandwidth (>100 nm, 12 THz) and resolution (<2×10^{-3} nm, 200 MHz), providing precise and accurate absorption spectra over long atmospheric paths [18,19].

Achieving field operation of the dual-comb spectrometer (DCS) under harsh conditions required several technological advancements over the laboratory-based proof-of-concept open-path DCS [18]. The original ring-cavity frequency combs relied

on nonlinear polarization rotation mode locking and were extremely sensitive to vibration and any environmental change that manipulated the polarization state within the cavity. The dual-comb spectrometer employed here utilizes a linear-cavity frequency comb design with all polarization-maintaining fiber and mode locking based on a semiconductor saturable absorber mirror (SESAM) [5,20]. The new frequency comb design was shown to be far more robust and capable of operation in a moving vehicle [5]. Phase coherence between the two frequency combs, and full stabilization of the frequency comb teeth in the original laboratory-based system, was achieved by phase locking the combs to two fiber lasers that were locked to a temperature-stabilized cavity under vacuum. This system was both expensive and sensitive to vibration and environmental changes. Stabilization of the fieldable system demonstrated here is achieved by locking the carrier offset frequency (f_{ceo}) using f-to-2f locking, and phase locking an individual tooth from each comb to a common 1 kHz linewidth continuous-wave (CW) commercial diode laser. The diode laser is then stabilized against drift through a feedback loop to the drive current or diode temperature using the repetition rate of one of the combs [6]. A commercially available ovenized quartz oscillator with high stability and low drift serves as the time base for all electronic components. These measures allow the DCS system to operate untethered from laboratory frequency references required by the proof-of-concept instrument, while still maintaining a level of stabilization that allows for the high-fidelity measurements presented here.

The near-infrared (NIR) frequency comb oscillators used here generate light around 1.55 μm over a ∼10 nm range. The light from each oscillator is amplified and spectrally broadened (using highly nonlinear fiber) to cover from 1.0 to 2.2 μm (for f-to-2f locking). The light from the two combs is then combined and spectrally filtered using a custom fiberized interference filter so that only light in the 1.62–1.69 μm region is sent over the open path (an optimal NIR wavelength range for measurement of atmospheric CH_4 and water vapor over long paths with high precision). The filtered light is then transmitted via 20 m of single-mode fiber (SMF) to the telescope transceiver, which is located either on top of the spectrometer trailer or on a standalone tower nearby. The transceiver sends light to and receives light from the retroreflectors, which are placed in the field, as demonstrated here, or can be located on an unmanned aerial system as in [21].

A single 100-MHz-bandwidth InGaAs photodetector mounted on the telescope transceiver is used for detection of the dual-comb interference signal. The detector signal is transmitted to the data collection system inside the mobile laboratory. A bias tee separates the RF and DC components of the signal. The DC portion is used to monitor the power reaching the detector. The RF portion is passed to the data collection system and digitized at 14 bits and 200 MHz (clocked at the repetition rate of one of the combs). Prior to digitizing, the dual-comb signal is amplified and attenuated in order to optimize linearity of the detection system [19]. The digitizer is controlled by a custom acquisition code that allows for real-time averaging of individual interferograms as well as phase correction and additional averaging of phase-corrected interferograms in order to reduce the final data burden. For these tests, individual interferograms are recorded at ∼630 Hz and averaged for 128 s with phase corrections applied to the interferograms every 150 ms. An example transmission spectrum from the DCS is shown in Fig. 2(a).

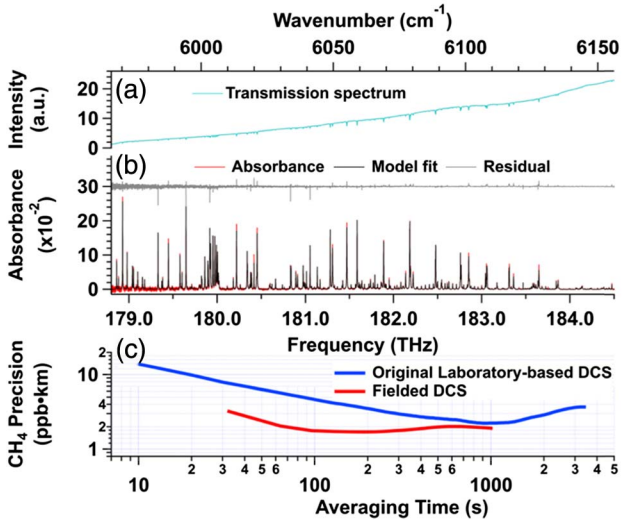

Fig. 2. (a) Raw transmission spectrum. (b) Result of fit with absorbance model including CH_4, CO_2, and H_2O. The fit residual is largest near water vapor features in the spectrum. (a) and (b) share horizontal axes. (c) Allan deviation for methane mole fraction data collected during well-mixed atmospheric conditions and without nearby leak sources. Also included in (c) is an Allan deviation trace from open-path DCS measurements using the original laboratory-based system [13].

The spectra are fit with an absorption model (based on the HITRAN database in this case) to simultaneously retrieve the atmospheric concentration of all trace gases that absorb within the bandwidth [Fig. 2(b)]. The combination of the dual-comb instrument and fitting approach produces results that are undistorted by atmospheric turbulence, free from instrument-specific lineshapes, robust against species interference, and require no periodic calibration (the absorption model serves as the permanent calibration for all instruments) [18,19]. Cross validations between this DCS instrument and another using the same fieldable design show a long-term agreement of 0.35% (7 ppb) in CH_4 concentration [19]. Thus, the instruments can be networked and the measurements linked (through an appropriate absorption model) to international standards without periodic calibration.

Figure 2(c) shows the instrument precision versus averaging time (Allan deviation) for methane measurements with the fielded DCS under windy well-mixed conditions. This gives an indication of the DCS performance and optimal averaging time under ideal conditions. The measurements used for the Allan deviation calculation were taken without a leak present, during a 6 h period when the atmospheric variability in background methane was very low, which is necessary to accurately decouple instrument performance from natural atmospheric variations. The methane measurement precision is compared with results from the original laboratory-based system under similar conditions. The fielded DCS system is shown to be more precise, reaching below 2 ppb · km sensitivity in 100 s. The improvement in precision is mostly the result of improved transceiver throughput over the laboratory-based setup (see Supplement 1 for further details). This performance compares well with other work using a similar DCS architecture [6,19,22].

The current spectrometer is capable of detecting a range of near-infrared absorbing molecules such as CH_4, H_2O, CO_2,

and isotopologues. With modifications, it would be capable of detecting O_2, SO_2, NH_3, and CO. More complex comb spectrometers operating further into the mid-infrared will expand the list of detectable molecules in the future [23].

3. TIME-RESOLVED INVERSION OF THE DCS DATA TO LOCATE AND SIZE TRACE-GAS SOURCES

New inversion techniques are needed to provide time-resolved location and quantification of sources with the sparse array of line-of-sight integrated open-path measurements provided by the DCS. For this, we implement an inversion that identifies sources and quantifies emissions at multiple possible source locations, given a time series of observations and related covariance, a transport model to relate the sources and open-path measurements, and estimates of temporal and spatial emission and background covariance [24].

Specifically, we use a Bayesian inversion to solve for time-resolved fluxes. The technique allows for the identification of the onset and end of potentially intermittent emissions, and has not previously been employed for this type of application. We achieve time resolution that varies from several minutes to tens of minutes, depending upon the number of retroreflectors queried and measurement frequency. Following [24], the standard formulation for the mass emission rate estimate, or flux estimate, $\hat{\mathbf{s}}$, is

$$\hat{\mathbf{s}} = \mathbf{s}_p + \mathbf{Q}\mathbf{H}^T(\mathbf{H}\mathbf{Q}\mathbf{H}^T + \mathbf{R})^{-1}(\mathbf{z} - \mathbf{H}\mathbf{s}_p). \quad (1)$$

The $m \times 1$ posterior flux vector is $\hat{\mathbf{s}}$. $\mathbf{s}_p$ is the $m \times 1$ state vector of prior source estimates, $\mathbf{z}$ is the $n \times 1$ vector of observations, $\mathbf{R}$ is the $n \times n$ matrix of observation covariance, $\mathbf{Q}$ is the $m \times m$ matrix of prior flux covariance, and $\mathbf{H}$ is the $n \times m$ matrix of source–receptor functions. The dimension n is equal to the number of observations. The dimension m is equal to the number of mass emission rates to be estimated, which is equal to the number of time steps evaluated multiplied by the number of potential source locations to be monitored.

The inversion uses spectrometer measurements as the prior estimate for background concentrations, thereby removing potentially confounding signals from nearby emissions and obviating the need for additional sensors to constrain background conditions. A unique aspect of our approach is that background concentrations are optimized in the inversion to limit aliasing of background uncertainty onto flux estimation. Any atmospheric transport model can be used to determine the source–receptor functions. Here, we use the Gaussian plume model as a steady-state solution to atmospheric transport, such that the number of time steps of flux estimation is equal to the number of atmospheric observations, n. Assumptions of steady-state atmospheric transport, based on mean meteorological conditions during a 2 min measurement window, are an appropriate choice because the travel time (approximated using mean wind speed) from a given source location to its assigned downwind beam is comparable to measurement averaging times. Further, our use of a simplified model of atmospheric transport serves as a baseline assessment of the viability of the methodology; more advanced models can be employed in the future, which could reasonably be expected to reduce the error in the posterior leak estimate. A more detailed description of the components of the inversion can be found in Supplement 1. Additionally, there is potential to explore other numerical methods for decreasing uncertainty in derived emission rates using open-path DCS data [25].

4. RESULTS

In the initial deployment described here, we choose the important case of methane emission detection and quantification from oil and gas operations to demonstrate the capability of the system. To this end, controlled methane sources are dispersed across a field site to simulate emissions from natural gas production sites. The fielded DCS is located at the Table Mountain Field Site, ~10 km north of Boulder, Colorado (Fig. 3). A trailer houses the DCS, but the volume of the DCS and supporting equipment is $0.6 \times 0.9 \times 0.7$ m and thus amenable to smaller platforms. The launch/receive optics and pointing gimbal are mounted on the trailer roof or an adjacent tower. Both the frequency combs and transceiver optics have been subjected to four seasons of weather over a 12 month operational period including drastic temperature variations (~18°C daily), significant wind loading (>30 ms^{-1}), and precipitation (rain, snow). Retroreflectors are placed at distances of up to 1.1 km from the spectrometer. Targeted sequentially, each retroreflector reflects laser light back to the photodetector co-located with the launch optics. The retroreflectors are placed among the potential sources (lateral offset between source and beam path is 15–60 m) for measurement of upwind and downwind integrated trace-gas concentrations along sets of laser beams, enabling the estimation of background concentrations for each potential emission site and for each time step. This configuration holds potential for identification of even very small sources in regions with a high density of oil and gas operations, where ambient concentrations of methane can have high spatial and rapid temporal variability.

First, we demonstrate the identification and quantification of a very small, variable-rate emission at a distance of 1 km (Fig. 4). Atmospheric measurements begin at 09:00 local time, and continue until 07:00 the following day. At 14:05, the controlled release of 7.7 g min^{-1} begins. At 18:00 the rate changes to 4.6 g min^{-1}, at 22:00 the rate drops again to 3.1 g min^{-1}, and at 00:00 drops to 1.6 g min^{-1}, before stopping completely at 04:55 (Fig. 4). Atmospheric CH_4 measurements downwind of the leak show clear enhancements when the controlled release begins, and the inversion successfully predicts that no leak is present before this time (the posterior flux is within $1 - \sigma$ of zero). The posterior emission estimate becomes significantly greater than zero within minutes of the true leak start, demonstrating that the system can rapidly identify the onset of emissions, a particularly important feature for intermittent sources. The posterior emission estimate remains significant for the entire leak duration, becoming indistinguishable from zero only when the controlled release is shut off at 04:55 the next day. The posterior emission rate is variable, particularly during periods of low wind speed and shifting wind directions, such as occurred between 16:00 and 20:00 (see Figs. 4 and S1), and at night, when parameterization of atmospheric stability is difficult. Use of more sophisticated transport models and parameterizations may be expected to increase the fidelity of the representation of atmospheric flow, and may therefore lead to reductions in flux estimation errors. Over the measurement period, the root-mean squared (RMS) deviation between the measured and true leak rate is 2.9 g min^{-1}. For comparison, this value is smaller than the mean emissions from functioning pneumatic controllers on a well site [1,7].

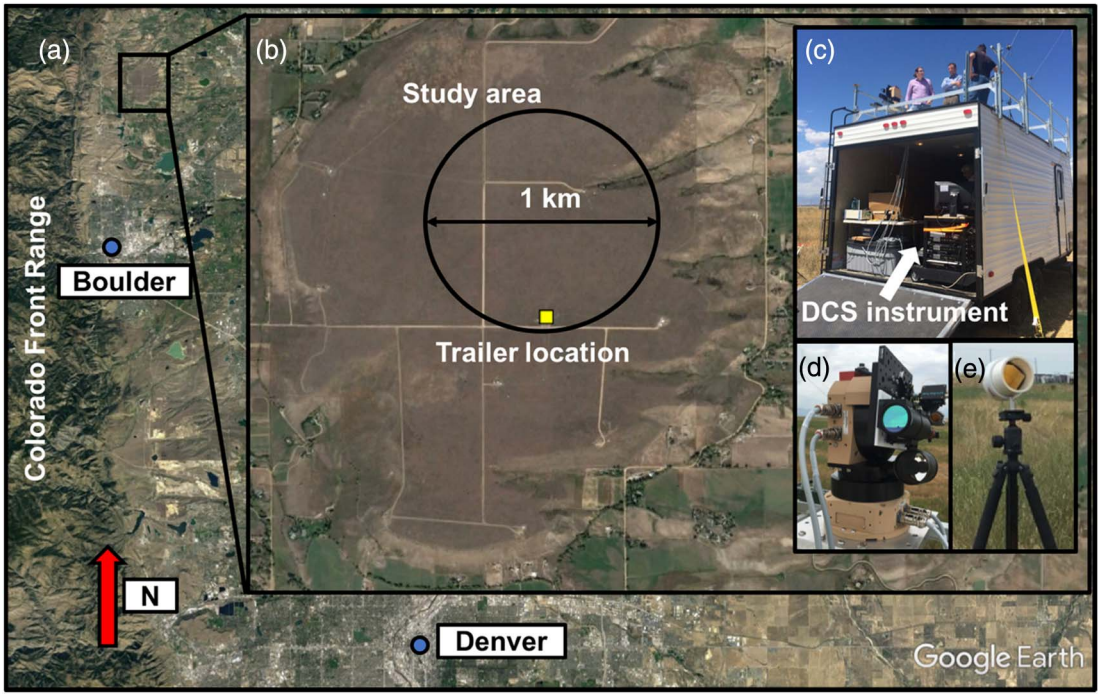

Fig. 3. Overview of the field site. (a) Table Mountain field site location. (b) Zoomed view of the site including mobile laboratory (yellow square) and the area over which tests were conducted (black circle). (c) Field deployed DCS, (d) gimbal/telescope, and (e) retroreflector.

During the period identified by the inversion as having nonzero emissions, the overall average posterior emission rate is 5.2 ± 1.6 g min^{-1}, which is within $1-\sigma$ of the true average emission rate of 4.9 g min^{-1} (Fig. 4). The rapid variability in the background methane concentration is immediately apparent in the data. Rapid increases and decreases in the overall methane concentration, e.g., at 12:00, 17:00, and 03:00, correspond with abrupt changes in the wind direction, which carries air masses from different urban, mountain, and nearby oil and gas production environments across the test site (see Fig. S1).

A second set of field tests assesses the ability of the observing system to locate and quantify simultaneous emissions from multiple sources. To simulate an accurate representation of the density of oil and gas production in the United States, the inversion is given prior knowledge of the spatial distribution of five well sites similar to a randomly selected section of the nearby Denver–Julesburg oil and gas basin. Controlled methane release points are positioned at two of five well sites (Fig. 5). Eight retroreflectors create an array of beams interspersed among the sites. Measurements begin at 09:00, and controlled releases begin at both emission points at 11:30 with equal rates of 3.1 g min^{-1}, increasing to 3.7 g min^{-1} at 13:10. Atmospheric measurements continue until both controlled releases are turned off at 17:00. The inversion identifies emissions at both sites beginning at the correct time (Fig. 5). The RMS deviation between the estimated and true leak strength is below 1.2 g min^{-1}. Equally important, the inversion also correctly identifies the three nonleaking well sites as having emissions consistent with zero. The sharp decrease in the overall methane occurring at 13:30 coincides with a shift in the wind direction, which brings in an air mass with lower background methane concentration (see Fig. S2).

These tests demonstrate that the system proved fully capable of detecting and quantifying 1) a small, variable methane emissions (1.6–8 g min^{-1}) from a distance of >1 km, and 2) two simultaneous methane emissions among a field of five potential sources. Both of these capabilities are advantageous for systems that seek to provide robust and sensitive monitoring for methane emissions in the oil and natural gas production sector.

5. DISCUSSION

The production, transport, and storage of natural gas from the more than 1 million active wells in the U.S. results in both intentional and unintentional emissions of 6–12 million metric tons of CH_4 to the atmosphere annually [26,27]. These emissions represent lost revenue, pose risks to public safety, accelerate climate change, and, through natural gas co-emissions, lead to decreased air quality [28]. The economics of leak mitigation is complicated by the wide spatial distribution and time variability of potential leaks, making the task of locating leaks with traditional optical gas imaging and handheld sensing technologies labor intensive, costly, and unreliable [29]. Existing methane sensing technologies offer high spatial but low temporal coverage or vice versa [30]. Satellite and aircraft mass balance approaches cover large regions but at coarse spatial and temporal resolution. Additionally, these methods are effective only under a subset of atmospheric conditions (e.g., clear sky) and are limited to identification of leaks greater than 1000–10,000 g min^{-1} [31–34]. Sensors mounted on vehicles require operators and offer snapshots in time [35–38]. Fixed, continuous ground-based sensors do not acquire sufficient information to locate specific sources from more than a few hundreds of meters [29], and are currently too expensive for adequate monitoring of oil and gas operations.

The dual-comb spectrometer and atmospheric inversion approach demonstrated here offers the ability to continuously and autonomously monitor many potential sources across multiple square kilometer regions with emission rates down to

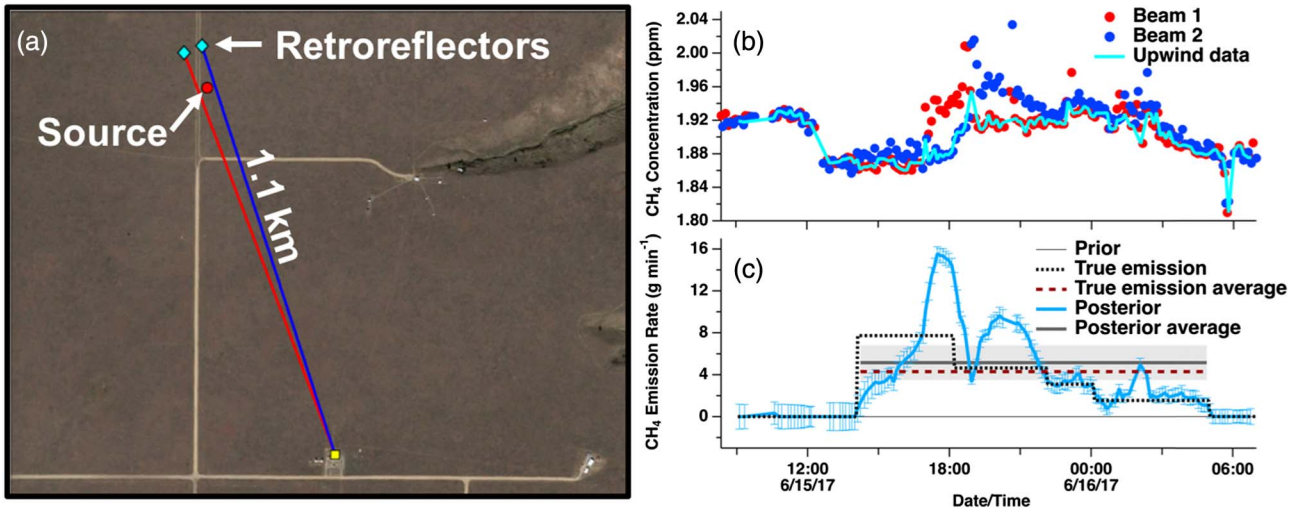

Fig. 4. Detection of a small, time-varying methane source from 1 km. (a) Map showing the site configuration including retroreflectors (blue diamonds) and source (red circle). (b) Methane concentrations measured on beam paths shown in (a). The light blue line denotes the background measurement (the upwind beam depends on wind direction). (c) Retrieved emission rate (blue line; error bars are 1 – σ posterior uncertainty), compared with true emission rate (black dotted line). Also shown is the prior estimate of the emission (thin gray line at zero) used in the inversion and the average values for both the true emission rate (maroon dashed line) and the posterior (thick gray line with mean uncertainty).

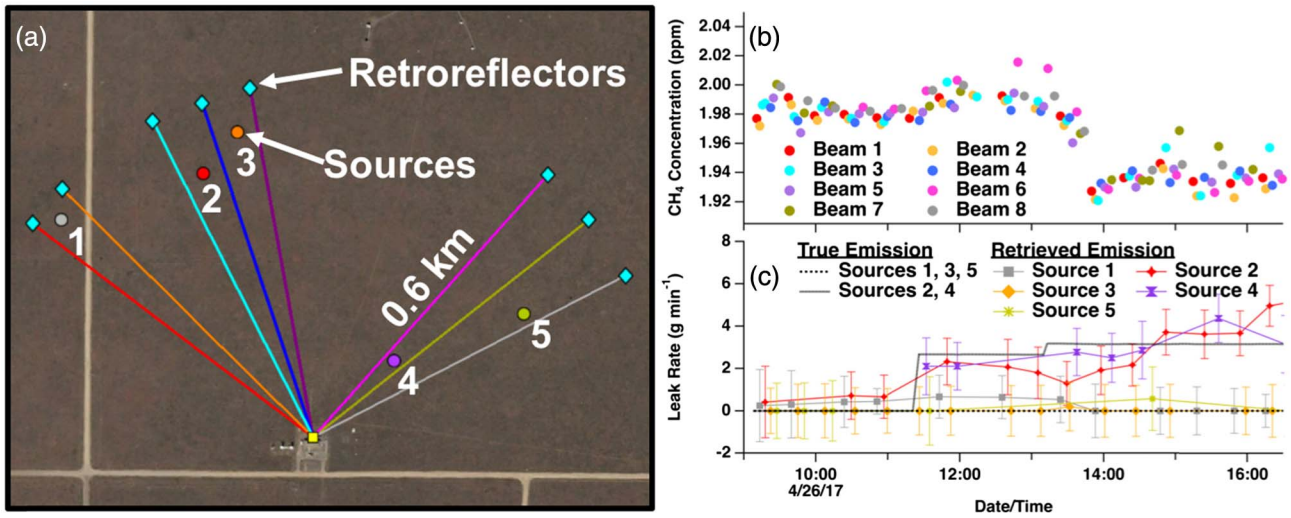

Fig. 5. Detection of two sources from among multiple potential sources. Layout of (a) and (b) in this figure follow that of Fig. 4. (c) True emission rates (sources 2 and 4, solid gray lines; sources 1, 3, and 5, dotted black lines) and retrieved emission rates (sources 1, gray squares; 2, red diamonds; 3, orange diamonds; 4, purple hourglasses; 5, gold asterisks).

1.6 g min^{-1}. Achieving this level of sensitivity means that the system is capable of detecting all sources relevant to oil and gas infrastructure, from so-called "super-emitters," or large point sources that account for a substantial portion of annual renegade emissions, to small sources <1 ton yr^{-1} (e.g., faulty pneumatic controllers). Additionally, the ability to support continuous monitoring increases the chances of detecting large (and small) episodic emission sources, for which there is currently little to no data describing the frequency of occurrence. Thus, in regions of dense oil and gas operations, this approach could lead to drastically reduced monitoring costs, enabling economically viable leak mitigation.

Future applications of the observation and inversion framework described here range from detection and quantification of trace gas sources over large urban and rural regions to sensitive early-warning systems for the presence of small amounts of airborne chemical constituents, to confirmation and monitoring of underground storage or sequestration of gaseous materials. The system bridges a critical gap in existing trace-gas monitoring capabilities by providing highly sensitive, time-varying, continuous, regional-scale coverage.

Funding. Advanced Research Projects Agency—Energy (ARPA-E) (DE-AR0000539); Office of Fossil Energy (DE-FE0029168); Defense Advanced Research Projects Agency (DARPA); National Institute of Standards and Technology (NIST).

Acknowledgment. The authors would like to thank research leaders at the Table Mountain Test Site for help with logistics and for facilitating the field deployment and research activities covered in this paper.

See Supplement 1 for supporting content.

†These authors contributed equally to this work.

REFERENCES

1. D. Zavala-Araiza, R. A. Alvarez, D. R. Lyon, D. T. Allen, A. J. Marchese, D. J. Zimmerle, and S. P. Hamburg, "Super-emitters in natural gas infrastructure are caused by abnormal process conditions," Nat. Commun. **8**, 14012 (2017).
2. A. R. Brandt, G. A. Heath, E. A. Kort, F. O'Sullivan, G. Pétron, S. M. Jordaan, P. Tans, J. Wilcox, A. M. Gopstein, D. Arent, S. Wofsy, N. J. Brown, R. Bradley, G. D. Stucky, D. Eardley, and R. Harriss, "Methane leaks from North American natural gas systems," Science **343**, 733–735 (2014).
3. S. Schwietzke, G. Pétron, S. Conley, C. Pickering, I. Mielke-Maday, E. J. Dlugokencky, P. P. Tans, T. Vaughn, C. Bell, D. Zimmerle, S. Wolter, C. W. King, A. B. White, T. Coleman, L. Bianco, and R. C. Schnell, "Improved mechanistic understanding of natural gas methane emissions from spatially resolved aircraft measurements," Environ. Sci. Technol. **51**, 7286–7294 (2017).
4. T. Lauvaux, N. L. Miles, A. Deng, S. J. Richardson, M. O. Cambaliza, K. J. Davis, B. Gaudet, K. R. Gurney, J. Huang, D. O'Keefe, Y. Song, A. Karion, T. Oda, R. Patarasuk, I. Razlivanov, D. Sarmiento, P. Shepson, C. Sweeney, J. Turnbull, and K. Wu, "High-resolution atmospheric inversion of urban CO_2 emissions during the dormant season of the Indianapolis Flux Experiment (INFLUX)," J. Geophys. Res. Atmos. **121**, 5213–5236 (2016).
5. L. C. Sinclair, I. Coddington, W. C. Swann, G. B. Rieker, A. Hati, K. Iwakuni, and N. R. Newbury, "Operation of an optically coherent frequency comb outside the metrology lab," Opt. Express **22**, 6996–7006 (2014).
6. G.-W. Truong, E. M. Waxman, K. C. Cossel, E. Baumann, A. Klose, F. R. Giorgetta, W. C. Swann, N. R. Newbury, and I. Coddington, "Accurate frequency referencing for fieldable dual-comb spectroscopy," Opt. Express **24**, 30495–30504 (2016).
7. D. T. Allen, A. P. Pacsi, D. W. Sullivan, D. Zavala-Araiza, M. Harrison, K. Keen, M. P. Fraser, A. Daniel Hill, R. F. Sawyer, and J. H. Seinfeld, "Methane emissions from process equipment at natural gas production sites in the United States: pneumatic controllers," Environ. Sci. Technol. **49**, 633–640 (2015).
8. J. L. Hall, "Nobel lecture: defining and measuring optical frequencies," Rev. Mod. Phys. **78**, 1279–1295 (2006).
9. T. W. Hänsch, "Nobel lecture: passion for precision," Rev. Mod. Phys. **78**, 1297–1309 (2006).
10. K. C. Cossel, E. M. Waxman, I. A. Finneran, G. A. Blake, J. Ye, and N. R. Newbury, "Gas-phase broadband spectroscopy using active sources: progress, status, and applications," J. Opt. Soc. Am. B **34**, 104–129 (2017).
11. I. Coddington, N. Newbury, and W. Swann, "Dual-comb spectroscopy," Optica **3**, 414–426 (2016).
12. F. Adler, M. J. Thorpe, K. C. Cossel, and J. Ye, "Cavity-enhanced direct frequency comb spectroscopy: technology and applications," Annu. Rev. Anal. Chem. **3**, 175–205 (2010).
13. A. Schliesser, M. Brehm, F. Keilmann, and D. W. van der Weide, "Frequency-comb infrared spectrometer for rapid, remote chemical sensing," Opt. Express **13**, 9029–9038 (2005).
14. T. Ideguchi, A. Poisson, G. Guelachvili, N. Picqué, and T. W. Hänsch, "Adaptive real-time dual-comb spectroscopy," Nat. Commun. **5**, 3375 (2014).
15. J. Roy, J.-D. Deschênes, S. Potvin, and J. Genest, "Continuous real-time correction and averaging for frequency comb interferometry," Opt. Express **20**, 21932–21939 (2012).
16. S. Okubo, K. Iwakuni, H. Inaba, K. Hosaka, A. Onae, H. Sasada, and F.-L. Hong, "Ultra-broadband dual-comb spectroscopy across 1.0-1.9 μm," Appl. Phys. Express **8**, 082402 (2015).
17. M. Cassinerio, A. Gambetta, N. Coluccelli, P. Laporta, and G. Galzerano, "Absolute dual-comb spectroscopy at 1.55 μm by free-running Er:fiber lasers," Appl. Phys. Lett. **104**, 231102 (2014).
18. G. B. Rieker, F. R. Giorgetta, W. C. Swann, J. Kofler, A. M. Zolot, L. C. Sinclair, E. Baumann, C. Cromer, G. Petron, C. Sweeney, P. P. Tans, I. Coddington, and N. R. Newbury, "Frequency-comb-based remote sensing of greenhouse gases over kilometer air paths," Optica **1**, 290–298 (2014).
19. E. M. Waxman, K. C. Cossel, G.-W. Truong, F. R. Giorgetta, W. C. Swann, S. Coburn, R. J. Wright, G. B. Rieker, I. Coddington, and N. R. Newbury, "Intercomparison of open-path trace gas measurements with two dual-frequency-comb spectrometers," Atmos. Meas. Tech. Katlenburg-Lindau **10**, 3295–3311 (2017).
20. L. C. Sinclair, J.-D. Deschênes, L. Sonderhouse, W. C. Swann, I. H. Khader, E. Baumann, N. R. Newbury, and I. Coddington, "Invited article: a compact optically coherent fiber frequency comb," Rev. Sci. Instrum. **86**, 081301 (2015).
21. K. C. Cossel, E. M. Waxman, F. R. Giorgetta, M. Cermak, I. R. Coddington, D. Hesselius, S. Ruben, W. C. Swann, G.-W. Truong, G. B. Rieker, and N. R. Newbury, "Open-path dual-comb spectroscopy to an airborne retroreflector," Optica **4**, 724–728 (2017).
22. P. J. Schroeder, R. J. Wright, S. Coburn, B. Sodergren, K. C. Cossel, S. Droste, G. W. Truong, E. Baumann, F. R. Giorgetta, I. Coddington, N. R. Newbury, and G. B. Rieker, "Dual frequency comb laser absorption spectroscopy in a 16 MW gas turbine exhaust," Proc. Combust. Inst. **36**, 4565–4573 (2017).
23. A. Schliesser, N. Picqué, and T. W. Hänsch, "Mid-infrared frequency combs," Nat. Photonics **6**, 440–449 (2012).
24. A. Tarantola, *Inverse Problem Theory*, 1st ed. (Elsevier Science, 1987).
25. C. B. Alden, S. Ghosh, S. Coburn, C. Sweeney, A. Karion, R. Wright, I. Coddington, K. Prasad, and G. B. Rieker, "Methane leak detection and sizing over long distances using dual frequency comb laser spectroscopy and a bootstrap inversion technique," Atmos. Meas. Tech. Discuss. (in review, 2017), DOI: 10.5194/amt-2017-262.
26. C. W. Moore, B. Zielinska, G. Pétron, and R. B. Jackson, "Air impacts of increased natural gas acquisition, processing, and use: a critical review," Environ. Sci. Technol. **48**, 8349–8359 (2014).
27. R. A. Alvarez, S. W. Pacala, J. J. Winebrake, W. L. Chameides, and S. P. Hamburg, "Greater focus needed on methane leakage from natural gas infrastructure," Proc. Natl. Acad. Sci. **109**, 6435–6440 (2012).
28. G. Pétron, A. Karion, C. Sweeney, B. R. Miller, S. A. Montzka, G. J. Frost, M. Trainer, P. Tans, A. Andrews, J. Kofler, D. Helmig, D. Guenther, E. Dlugokencky, P. Lang, T. Newberger, S. Wolter, B. Hall, P. Novelli, A. Brewer, S. Conley, M. Hardesty, R. Banta, A. White, D. Noone, D. Wolfe, and R. Schnell, "A new look at methane and nonmethane hydrocarbon emissions from oil and natural gas operations in the Colorado Denver-Julesburg Basin," J. Geophys. Res. Atmospheres **119**, 6836–6852 (2014).
29. A. P. Ravikumar, J. Wang, and A. R. Brandt, "Are optical gas imaging technologies effective for methane leak detection?" Environ. Sci. Technol. **51**, 718–724 (2017).
30. S. M. Miller, S. C. Wofsy, A. M. Michalak, E. A. Kort, A. E. Andrews, S. C. Biraud, E. J. Dlugokencky, J. Eluszkiewicz, M. L. Fischer, G. Janssens-Maenhout, B. R. Miller, J. B. Miller, S. A. Montzka, T. Nehrkorn, and C. Sweeney, "Anthropogenic emissions of methane in the United States," Proc. Natl. Acad. Sci. USA **110**, 20018–20022 (2013).
31. C. Frankenberg, J. F. Meirink, M. van Weele, U. Platt, and T. Wagner, "Assessing methane emissions from global space-borne observations," Science **308**, 1010–1014 (2005).
32. D. J. Jacob, A. J. Turner, J. D. Maasakkers, J. Sheng, K. Sun, X. Liu, K. Chance, I. Aben, J. McKeever, and C. Frankenberg, "Satellite observations of atmospheric methane and their value for quantifying methane emissions," Atmos. Chem. Phys. **16**, 14371–14396 (2016).
33. M. O. L. Cambaliza, P. B. Shepson, D. R. Caulton, B. Stirm, D. Samarov, K. R. Gurney, J. Turnbull, K. J. Davis, A. Possolo, A. Karion, C. Sweeney, B. Moser, A. Hendricks, T. Lauvaux, K. Mays, J. Whetstone, J. Huang, I. Razlivanov, N. L. Miles, and S. J. Richardson, "Assessment of uncertainties of an aircraft-based mass balance approach for quantifying urban greenhouse gas emissions," Atmos. Chem. Phys. **14**, 9029–9050 (2014).
34. S. Conley, G. Franco, I. Faloona, D. R. Blake, J. Peischl, and T. B. Ryerson, "Methane emissions from the 2015 Aliso Canyon blowout in Los Angeles, CA," Science **351**, 1317–1320 (2016).

35. H. L. Brantley, E. D. Thoma, W. C. Squier, B. B. Guven, and D. Lyon, "Assessment of methane emissions from oil and gas production pads using mobile measurements," Environ. Sci. Technol. **48**, 14508–14515 (2014).
36. T. I. Yacovitch, S. C. Herndon, G. Pétron, J. Kofler, D. Lyon, M. S. Zahniser, and C. E. Kolb, "Mobile laboratory observations of methane emissions in the Barnett Shale region," Environ. Sci. Technol. **49**, 7889–7895 (2015).
37. G. Pétron, G. Frost, B. R. Miller, A. I. Hirsch, S. A. Montzka, A. Karion, M. Trainer, C. Sweeney, A. E. Andrews, L. Miller, J. Kofler, A. Bar-Ilan, E. J. Dlugokencky, L. Patrick, C. T. Moore, T. B. Ryerson, C. Siso, W. Kolodzey, P. M. Lang, T. Conway, P. Novelli, K. Masarie, B. Hall, D. Guenther, D. Kitzis, J. Miller, D. Welsh, D. Wolfe, W. Neff, and P. Tans, "Hydrocarbon emissions characterization in the Colorado front range: a pilot study," J. Geophys. Res. Atmos. **117**, D04304 (2012).
38. J. R. Roscioli, T. I. Yacovitch, C. Floerchinger, A. L. Mitchell, D. S. Tkacik, R. Subramanian, D. M. Martinez, T. L. Vaughn, L. Williams, D. Zimmerle, A. L. Robinson, S. C. Herndon, and A. J. Marchese, "Measurements of methane emissions from natural gas gathering facilities and processing plants: measurement methods," Atmos. Meas. Tech. **8**, 2017–2035 (2015).

Atmos. Meas. Tech., 11, 1565–1582, 2018
https://doi.org/10.5194/amt-11-1565-2018

Atmospheric Measurement Techniques
Open Access
EGU

Bootstrap inversion technique for atmospheric trace gas source detection and quantification using long open-path laser measurements

Caroline B. Alden[1,2], Subhomoy Ghosh[3], Sean Coburn[1], Colm Sweeney[2,4], Anna Karion[3], Robert Wright[1], Ian Coddington[3], Gregory B. Rieker[1], and Kuldeep Prasad[3]

[1]Precision Laser Diagnostics Laboratory, University of Colorado at Boulder, Boulder, CO 80309, USA
[2]Cooperative Institute for Research in Environmental Sciences, Boulder, CO 80309, USA
[3]National Institute of Standards and Technology (NIST), Gaithersburg, MD 20899, USA
[4]National Oceanic & Atmospheric Administration (NOAA), Boulder, CO 80305, USA

Correspondence: Caroline B. Alden (caroline.alden@colorado.edu)

Received: 25 July 2017 – Discussion started: 16 October 2017
Revised: 14 December 2017 – Accepted: 17 January 2018 – Published: 22 March 2018

Abstract. Advances in natural gas extraction technology have led to increased activity in the production and transport sectors in the United States and, as a consequence, an increased need for reliable monitoring of methane leaks to the atmosphere. We present a statistical methodology in combination with an observing system for the detection and attribution of fugitive emissions of methane from distributed potential source location landscapes such as natural gas production sites. We measure long (> 500 m), integrated open-path concentrations of atmospheric methane using a dual frequency comb spectrometer and combine measurements with an atmospheric transport model to infer leak locations and strengths using a novel statistical method, the non-zero minimum bootstrap (NZMB). The new statistical method allows us to determine whether the empirical distribution of possible source strengths for a given location excludes zero. Using this information, we identify leaking source locations (i.e., natural gas wells) through rejection of the null hypothesis that the source is not leaking. The method is tested with a series of synthetic data inversions with varying measurement density and varying levels of model–data mismatch. It is also tested with field observations of (1) a non-leaking source location and (2) a source location where a controlled emission of 3.1×10^{-5} kg s^{-1} of methane gas is released over a period of several hours. This series of synthetic data tests and outdoor field observations using a controlled methane release demonstrates the viability of the approach for the detection and sizing of very small leaks of methane across large distances (4+ km^2 in synthetic tests). The field tests demonstrate the ability to attribute small atmospheric enhancements of 17 ppb to the emitting source location against a background of combined atmospheric (e.g., background methane variability) and measurement uncertainty of 5 ppb (1σ), when measurements are averaged over 2 min. The results of the synthetic and field data testing show that the new observing system and statistical approach greatly decreases the incidence of false alarms (that is, wrongly identifying a well site to be leaking) compared with the same tests that do not use the NZMB approach and therefore offers increased leak detection and sizing capabilities.

1 Introduction

The combustion of natural gas in high-efficiency power cycles is cleaner and produces less climate-warming carbon dioxide gas than the combustion of coal (Environmental Protection Agency, 2015), which has led to interest in natural gas as a cleaner alternative to coal for energy generation. Advances in natural gas extraction technology have led to a 35 % increase in total natural gas production between 2005 and 2013 in the United States (U.S. Energy Information Administration, 2015). Production is expected to increase by 45 % above 2013 levels by the year 2040 (U.S. Energy Information Administration, 2015). A caveat to the promise of

natural gas as a lower climate impact energy source, however, is that leaks of methane during extraction and delivery can result in climate warming. Methane gas has high global warming potential (GWP): much higher, for example, than carbon dioxide (CH_4 has a GWP of 28 over 100 years, compared with CO_2, which has GWP of 1 by definition Myhre et al., 2013). Above a low threshold (estimated to be ≈ 3.2 % by Alvarez et al., 2012) leak rate from well to power plant, the near-term climate impacts of using natural gas for power generation become worse than coal (Alvarez et al., 2012; Hayhoe et al., 2002). Recent system-wide analysis suggests that natural gas sector leak rates are likely higher than inventory estimates (Brandt et al., 2014; Zavala-Araiza et al., 2015a). To achieve the lower climate impacts and greater economic benefits of domestic natural gas production, it is important to find low-cost methods to detect and reduce methane leakage (Alvarez et al., 2012).

The current industry practice for leak detection and repair (LDAR) is to perform infrequent (annual or less for most sites) "spot" checks for leaks, for example by visual inspection with an optical gas imaging (OGI) camera. However, recent work has shown that methane concentrations measured by OGI cameras can be drastically underestimated when conditions are not ideal, for example under conditions of lower temperature values or higher wind speeds, or when viewing distances are greater than 50 m (Ravikumar et al., 2016). Furthermore, spot check monitoring is inadequate for detection of leaks, given strong evidence for intermittency of leaks (Allen et al., 2013, 2015a; Mitchell et al., 2015; Subramanian et al., 2015). It has been observed that a small number of facilities leaking at very high rates – so-called "super-emitters" (Brandt et al., 2014; Frankenberg et al., 2016; Rella et al., 2015; Zavala-Araiza et al., 2015b) – can account for a majority of total emissions (Allen et al., 2013, 2015a, b; Brandt et al., 2014). These characteristics underscore the importance of continuous monitoring for leaks over large areas. Field campaigns with sophisticated atmospheric sampling techniques provide valuable snapshots of the state of natural gas development facility leaks (e.g., Brantley et al., 2014; Karion et al., 2013), but it would be too costly to employ such measurement strategies for long-term continuous monitoring of most natural gas sector facilities.

We present and test an atmospheric measurement system coupled with a statistical inversion approach for detecting and quantifying emissions of methane. The statistical approach is focused on limiting the occurrence of false-positive leak detection. The measurement system used to test the statistical approach is composed of a long-range open-path laser situated in the center of a field of well sites and a series of retroreflectors around the perimeter of the field to direct light back to a detector co-located with the laser. The concentration of trace gases along the open beam path (defined as the path between the spectrometer–detector system and a retroreflector) is determined from the species-specific absorption of light (Dobler et al., 2015; Flesch et al., 2004; Groth et al., 2015; Hashmonay et al., 1999; Levine et al., 2016). Many open-path absorption methods for determining species concentration have been demonstrated (Akagi et al., 2011; Dobler et al., 2015; Flesch et al., 2004; Jones et al., 2011; Nikodem et al., 2015; Wagner and Plusquellic, 2016; Wu et al., 2014). Here we use a dual frequency comb spectrometer (DCS): a unique broadband, high-resolution spectrometer that offers very high stability (low drift) and measurement reproducibility of the trace gas measurement so that concentrations can be compared across different conditions and times (Coburn et al., 2018). It was recently demonstrated that two separate dual frequency comb spectrometers stationed side by side and measuring the same 1 km outdoor path showed methane concentration agreement to 0.35 % over a 2-week period under ambient variations in temperature, pressure, and stability (Waxman et al., 2017). In principle, the range of conditions under which two separate dual frequency comb spectrometers should be comparable is much wider than ambient conditions, because the concentration retrieval is largely dependent on the quality of absorption models (which are well-defined under most conditions experienced at Earth's surface). Previous work also demonstrates that this method of atmospheric trace gas measurement does not require regular or traditional calibration (Coburn et al., n.d.; Rieker et al., 2014; Truong et al., 2016; Waxman et al., 2017). Laboratory and initial field measurements made with the dual frequency comb spectrometer indicate extremely high measurement precision (3 ppb or lower) over long (1 km one-way, or 2 km round trip) path lengths (Coburn et al., n.d.; Rieker et al., 2014; Truong et al., 2016; Waxman et al., 2017). The combination of low uncertainty and high stability enables new opportunities for detection and sizing of even very small emissions of methane (Coburn et al., n.d.). Furthermore, the demonstration of sensitive methane measurements over kilometer-scale open paths allows for monitoring methane concentrations over large areas such as natural gas production, processing, and distribution sites. While frequency comb measurements have previously been made in laboratory settings, the recent work of Coburn et al. (n.d.) and the new work shown here demonstrate the viability of dual frequency comb spectroscopy in real-world conditions.

We use the dual frequency comb measurements in a series of synthetic data and field data tests to demonstrate the utility of the observing system and a novel statistical method for accurately locating one or more point sources of methane within a large area ($4+$ km^2) using distributed measurements of methane concentrations and an atmospheric transport model. Previous studies have used Gaussian plume models with atmospheric measurements of wind conditions and constituent concentrations to detect sources (e.g., Hirst et al., 2004), and past studies have also shown the utility of open-path lasers for measuring across-plume concentrations for use in the detection of emissions (Flesch et al., 1995; McBain and Desjardins, 2005). Here, we present a novel statistical technique applied to source detection and quantifi-

cation – with the goal of minimizing false-positive source identification. The source-attribution method used here is to apply a non-negative least-squares (NNLS) fitting technique to solve for methane flux at a series of potential source locations (e.g., pads, well heads or other components), given a set of atmospheric observations and knowledge of atmospheric transport (Leuning et al., 2008). The new statistical approach, called the non-zero minimum bootstrap method (NZMB), uses a bootstrapping of model uncertainties to produce an empirical distribution of source strength for a given well site. Specifically, the empirical distribution is obtained by performing multiple atmospheric inversions (or estimates of surface fluxes using atmospheric data) using a set of resampled atmospheric measurements. The NZMB method establishes a criterion by which well sites or facilities are identified as having non-zero methane emissions based on examination of the minimum value of an ensemble of inversions. That is, a potential leak site is positively identified as a source of methane to the atmosphere when the empirical cumulative distribution of likely source strengths (determined with a series of bootstrap operations) does not include a minimum threshold flux such as zero. Similarly, a facility is identified as not leaking when the empirical cumulative distribution of likely source strengths does include the minimum threshold flux (that is, the minimum value of all bootstrap operations is, for example, zero). By defining a specific null value for each potential leak, this approach reduces the incidence of false-positive leak identification (the incorrect attribution of a methane source to a non-leaking facility or well), compared with the same tests that do not use the NZMB method (the "non-bootstrap" approach). For comparison, we run the same series of tests with the non-bootstrap approach, which approximates emissions using a single NNLS fit.

Synthetic data tests are performed that assess the effects of increasing measurement density (4, 8, 16, 32, and 64 beams) and the effects of increasing model–data mismatch (that is, combined uncertainty in the ability to simulate observations arising from measurement, transport, and other sources). Field tests with atmospheric observation data are performed in a $3\,\mathrm{km} \times 2.5\,\mathrm{km}$ field site located in north-central Colorado over the course of 1 day in January 2017. The meteorological conditions (wind speed, wind direction, atmospheric stability) on this day are typical of wintertime and annual mean conditions measured near the field site (for example, compared with conditions at nearby weather station KCOLONGM30). Field measurements are made along a series of three beams extending from a spectrometer in the middle of the domain.

We define leak identification success as maximizing the incidences of leaks found, with a minimal occurrence of false-positive source identification, enabling quick response to leaks and avoiding costly mobilization of repair teams due to false-positive leak identification. The ability to correctly ascertain the absence of a leak is therefore of equal importance to the ability to find leaks for regulatory compliance applications of this method. With the above tests, we therefore seek to determine (1) whether methane point source emissions can be detected and sized under conditions of observational uncertainty (model–data mismatch) and background variation; (2) whether the absence of a leak can be ascertained in an outdoor field setting; (3) whether the NZMB method allows for leaks to be positively identified under scenarios of greater simulated model–data mismatch uncertainty, compared with the non-bootstrap method; and (4) whether a higher number of observations increases likelihood that the NZMB and non-bootstrap methods can positively identify leaks. The success of the synthetic and field data tests demonstrates the potential of this observing system for continuous monitoring applications, such as for natural gas facilities, and for providing emission source locations and their approximate strengths. The experiments here also demonstrate the potential for this technology to be used for other source estimation and monitoring applications, for example carbon sequestration.

2 Methods

2.1 Gaussian plume atmospheric transport model

In both the synthetic and real data tests, atmospheric transport is simulated using a Gaussian plume model, using Pasquill–Gifford parameterization of plume dispersion in the lateral and vertical directions (Green et al., 1980; Griffiths, 1994; Hanna et al., 1982). Micrometeorology in the boundary layer is a non-trivial source of uncertainty for characterization of atmospheric flow, and the Gaussian plume model represents a simplified representation of atmospheric transport and dispersion. It is used to characterize the mean state (or steady state) of source–receptor relationships with a point source, as long as the transport time from source to receptor is comparable to the data averaging time (Gifford, 1976; Hirst et al., 2004). More sophisticated plume (e.g., AERMOD) or stochastic Lagrangian dispersion models (e.g., WindTrax) and stability parameterizations would be expected to provide more robust representations of the wind shear and inhomogeneities in turbulence in the atmospheric surface layer (Flesch et al., 1995; Perry et al., 1994; Wilson and Sawford, 1996). We select the simplified and low-computational-cost plume model for assessment of the NZMB method as a baseline test rather than implementing more advanced representations of transport. Future campaigns aimed at quantification of true emissions will benefit from an assessment of the drawbacks inherent in Gaussian plume model characterization of atmospheric transport or use of a more sophisticated model, particularly for measurements made at short range.

For the synthetic data tests, the choice of transport model is largely trivial, given that the transport is considered "perfect". Field data are collected with a constant methane source to the atmosphere and a measurement averaging time that is

comparable to the source-to-receptor travel time, such that the Gaussian plume model is a simplified but appropriate choice of transport model (Gifford, 1976; Hirst et al., 2004). Because the purpose of this study is to confirm or reject the basic methodology and not to investigate the impacts of micrometeorological representation on flux estimation, we find the plume model to be sufficient as a baseline test (see Sect. 6).

Neglecting influence of background methane concentrations, Eq. (1) shows the relationship between fluxes and atmospheric concentrations (e.g., Leuning et al., 2008):

$$\boldsymbol{c} = \boldsymbol{x} \times (\boldsymbol{c}/\boldsymbol{x})_{\text{modeled}}, \quad (1)$$

where the $n \times 1$ vector $\boldsymbol{c}$ is the atmospheric concentration of the constituent of interest, and n is the number of measurements. The vector $\boldsymbol{x}$ is $m \times 1$ sources of the constituent (flux units), where the size of m is equal to the number of potential source flux locations. Here, the vector of fluxes, $\boldsymbol{x}$, is the emission rate of methane from each potential source location. In the synthetic tests and field tests described here, multiple measurements are made on each beam, such that n is always greater than m. The value $(\boldsymbol{c}/\boldsymbol{x})_{\text{modeled}}$ is the transport operator matrix describing the relationship between the point source emission and concentrations at observation points (spectrometer beams) under different meteorological conditions, derived using the Gaussian plume model, and commonly written as $\mathbf{H}$ (that convention will be followed here; see Sect. 2.5.3 for details on scaling from point source, to point concentration, to line-averaged concentration).

2.2 Dual frequency comb spectrometer for long-range open-path methane detection

Dual frequency comb spectrometer measurements are made by transmitting light from the spectrometer through open air at a discrete set of wavelengths where methane absorbs light. The light is transmitted in the direction of a retroreflector, which can be placed 1+ km away (Coburn et al., n.d.; Rieker et al., 2014; Truong et al., 2016; Waxman et al., 2017). The retroreflector directs light back toward a detector co-located with the spectrometer. The amount of light that is absorbed by methane yields a direct measurement of the average concentration of methane along the open path from spectrometer to retroreflector. The measurements presented here are part of the first campaign to measure atmospheric concentrations with a fielded dual frequency comb spectrometer (Coburn et al., n.d.). The temporal resolution of measurements is related to averaging time: as averaging time increases, measurement precision increases, until such time that atmospheric CH_4 variability begins to erode measurement repeatability (see Sect. 4.1). The spatial resolution of the measurement depends on beam length, which is easily adjusted by moving retroreflectors closer to or further away from the spectrometer, and beam width, which scales with telescope diameter.

2.3 Flux estimation with non-negative least-squares fitting solution

We use the NNLS algorithm in Fortran-90 to solve for a flux rate (that is, the emission rate from each potential source location), given atmospheric observations (synthetic or real) and atmospheric transport influence functions (Lawson and Hanson, 1995). This algorithm iteratively solves for the best-fit $m \times 1$ vector of fluxes, $\boldsymbol{x}$ (see Sect. 2.1 for a description of $\boldsymbol{x}$), given an $n \times 1$ vector of data measurements, $\boldsymbol{y}$, and an $n \times m$ matrix of influence functions, $\mathbf{H}$. Given $\mathbf{H}$ and $\boldsymbol{y}$, the NNLS algorithm computes a vector $\boldsymbol{x}$ (methane emission rate at each well site) that solves the least squares problem:

$$\mathbf{H}\boldsymbol{x} = \boldsymbol{y}, \text{ subject to } \boldsymbol{x} >= 0. \quad (2)$$

Uncertainties in $\boldsymbol{x}$ and $\boldsymbol{y}$ are not included in the NNLS fit; model–data mismatch is used only in generation of the synthetic observations and not as a control on the solution for $\boldsymbol{x}$. The NNLS algorithm returns the solution vector, $\boldsymbol{x}$, and also allows for the calculation of $\mathbf{H}\boldsymbol{x}$, an $n \times 1$ vector describing the expected atmospheric concentration given $\mathbf{H}$ and the solution for $\boldsymbol{x}$.

2.4 Non-zero minimum bootstrap analysis

The non-zero minimum bootstrap analysis, or NZMB, is a statistical test of the null hypothesis (Hypothesis_0) that the source strength at a given well site is equal to $0\,\text{kg}\,\text{s}^{-1}$. It is used here to estimate source strengths in both the synthetic and field data tests. Whereas bootstrapping methods and least-squares methods are not novel techniques and have previously been applied to problems of source strength estimation, we develop the present methodology with the motivation to seek a solution for fluxes in which the incidence of false-positive source attribution is limited (Efron, 1979; Lawson and Hanson, 1995).

For each of m potential source locations, the null hypothesis (Hypothesis_0) is that there is no methane emission from that potential source location, and the alternative hypothesis (Hypothesis_1) is that there is a (non-zero) emission from that potential source location:

$$\text{Hypothesis}_0 : x_j = 0 (j = 1, \ldots, m), \quad (3)$$

$$\text{Hypothesis}_1 : x_j > 0 (j = 1, \ldots, m). \quad (4)$$

Given that model–data mismatch uncertainty is not zero (i.e., there is uncertainty in the exact relationship between atmospheric observations and surface fluxes due to transport, measurement, and other uncertainties), it is not expected that the NNLS fit of $\mathbf{H}\boldsymbol{x}$ to $\boldsymbol{y}$ is exact, although the problem is overdetermined (that is, $n > m$). We therefore use the mismatch between $\mathbf{H}\boldsymbol{x}$ and $\boldsymbol{y}$ to create an empirical distribution function describing the confidence interval of the fit to the data and to accept or reject the null hypothesis claim that we have enough evidence to claim that a particular

source is not leaking. That is, the empirical fit to the data is used to quantify uncertainties associated with the model–data mismatch (including, for example, instrument and measurement uncertainties, transport uncertainties, and model uncertainties) rather than relying on a "bottom-up" estimation of those sources of uncertainty. We rely on the assumption that model–data mismatch uncertainty has an un-biased Gaussian distribution. Although biases in transport or other sources of uncertainty can exist, we suggest that investigation of that contingency is suited for future studies.

The method for employing the bootstrap analysis is as follows. We first solve for surface-to-atmosphere fluxes of CH_4, $\boldsymbol{x}$, using NNLS, as described in Sect. 2.3. Second, for each observation, y_i ($i = 1, \ldots, n$), we calculate the residual values from the fit to the NNLS solution:

$$\boldsymbol{e}_i = y_i - \hat{y}_i, \tag{5}$$

where $\hat{y}_i$ ($i = 1,\ldots,n$) are the individual values in the vector $\mathbf{H}\boldsymbol{x}$. The values of $\hat{y}_i$ ($i = 1,\ldots, n$) are the "predicted" change in atmospheric methane given the NNLS solution for $\boldsymbol{x}$, or the change in atmospheric methane that is simulated by convolving the source–receptor matrix, $\mathbf{H}$, with $\boldsymbol{x}$.

The next step in the NZMB method is, for each observation, y_i ($i = 1,\ldots, n$), to generate a new estimate of that observation by using Eq. (3) to sample from the vector of the residuals of the fit to the atmospheric data, $\boldsymbol{e}$ (with replacement, meaning a given value can be sampled more than once), and adding that randomly selected e_i value to the predicted observation value, $\hat{y}_i$, to create $y_{\mathrm{b}i}$ (Efron, 1979). That is, for each observation vector, $\boldsymbol{y}$, we create a new vector, $\boldsymbol{y}_{\mathrm{b}}$ (b denotes a bootstrapped value):

$$y_{\mathrm{b}i} = \hat{y}_i + \mathrm{e}_{\mathrm{b}i}. \tag{6}$$

We perform this step 1000 times, resulting in 1000 vectors $\boldsymbol{y}_{\mathrm{b}}$, or 1000 different sets of observations of the form $\{y_{\mathrm{b}i}, \ldots, y_{bn}\}$, where $y_{\mathrm{b}i} = \hat{y}_i + \mathrm{e}_{\mathrm{b}i}$.

For the field data, we apply a moving block bootstrap (Künsch, 1989) because residuals of observations made nearer together in time are more likely to be co-representative, whereas residuals of observations made further apart in time are likely to be less representative due to changes in wind conditions and atmospheric stability. We calculate the autocorrelation in time of the residuals resulting from a single non-negative least-squares fit and use for the moving block window length a value 2 times the lag time at which the autocorrelation falls below the 95 % confidence level. As there is no time dimension in the synthetic data case, we do not apply the moving block bootstrap to those cases.

Next, we use NNLS to solve for $\boldsymbol{x}$ for each of the 1000 resampled sets of observations, yielding 1000 individual solutions for $\boldsymbol{x}$. The final step in the NZMB method is to apply the non-zero-minimum criterion to the 1000 bootstrap solutions for each member of $\boldsymbol{x}$. For each possible source location, we find the minimum value from the 1000-member bootstrap analysis. The non-zero-minimum criterion states that if the minimum bootstrap value for a given well location is $0\,\mathrm{kg\,s^{-1}}$, then the source location is classified as having a leak rate of $0\,\mathrm{kg\,s^{-1}}$ (i.e., no leak). This criterion establishes, under the null hypothesis, whether or not 0 (<0 is not possible since a non-negative least-squares fit is used) is included in the domain of the empirical cumulative distribution function with non-zero mass, described by the 1000 solutions for each well site in $\boldsymbol{x}$. If zero is included in this distribution, then the null hypothesis ($\boldsymbol{x} = 0$) cannot be rejected. Conversely, if 0 is not included in the empirical cumulative distribution function for a given well site (x_j), then the null hypothesis can be rejected and it can be assumed that the well site is leaking. We use a large number of bootstrap members (1000) to ensure that the law of large numbers (LLN) is met. LLN justifies that when the number of bootstrap operations is large, the bootstrapped leak mean approaches the estimated leak from the sample (i.e., the bootstrapped leak mean is a consistent estimator of the estimated leak), and the distribution of the bootstrapped leak approaches the probability distribution of the source strength. Thus, we can claim that the bootstrapped estimator is a good candidate of the estimated leak from the NNLS and that the empirical cumulative distribution function is an approximation of the true cumulative distribution function.

After having identified which source locations are non-zero sources to the atmosphere (leaking), the mean leak strength is estimated as the mean of the 1000 bootstrap solutions for that source location. Uncertainty in the strength of the true leak is calculated as the standard deviation of the 1000 bootstrap solutions at the true leak location.

This method requires little additional computational cost over the non-bootstrap NNLS approach, because additional runs of the transport model are not required, only additional NNLS fits using resampling of the observations. The NZMB approach has the benefit of reducing false-positive solutions while also gathering information regarding the parameters of the assumed Gaussian distribution.

2.5 Synthetic data tests and results

2.5.1 "True" leak locations and strengths

To prepare synthetic data testing of the NZMB method, we randomly distribute 20 possible leak source locations within a theoretical $2\,\mathrm{km} \times 2\,\mathrm{km}$ domain. This is a reasonable approximation of well density based on high-production regions of the western United States (average well density across the Marcellus and Haynesville shale gas plays is 3+ wells $\mathrm{km^{-2}}$). In the synthetic tests, therefore, $m = 20$. Of the 20 well sites in the domain, we simulate a scenario in which two source locations are leaking. The "true" leak rate at well site number 6 is $4.5 \times 10^{-5}\,\mathrm{kg\,s^{-1}}$ and the "true" leak rate at well site number 19 is $3.0 \times 10^{-5}\,\mathrm{kg\,s^{-1}}$. The remaining 18 well sites are assigned "true" leak rates of $0\,\mathrm{kg\,s^{-1}}$ (Fig. 1).

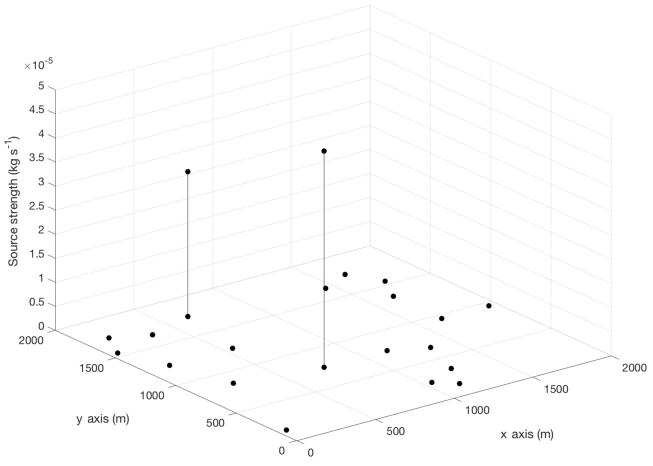

Figure 1. Synthetic test observation area: 2 km × 2 km domain with 20 source locations (black dots) at randomly distributed x and y locations (position shown on x and y axes). Of 20 point sources, well site 6 ($x = 750$, $y = 750$) and well site 19 ($x = 650$, $y = 1750$) have non-zero source strengths (shown on the z axis).

The two non-zero leak strengths are very small: roughly half the size of the smallest leaks found by Rella et al. (2015) in a survey of oil and natural gas well pads. The height above ground level of each leak is 1 m.

2.5.2 Idealized meteorological conditions for synthetic data tests

The meteorological data used for synthetic data tests include many wind directions and a variety of wind speeds during the sampling of each beam in the domain, representing an ideal scenario for the generation of as many independent measurements of the leak strength as possible. Leak strengths are constant through time, such that the time dimension of the meteorology does not need to be considered. This approach assumes that enough time has passed for all meteorological conditions to have occurred during the sampling of each beam, a condition that eliminates complications in comparing synthetic cases with different beam orientations. The idealized meteorological field applies 216 unique wind conditions to all beams: three wind speeds (2, 3, and 6 m s^{-1}) from 72 directions (from 5 to 360°, in 5° increments). The conditions represent a situation in which, over a long period of time, many different wind conditions yield a variety of different measurements downwind of emissions. Given the simple beam configuration presented here, which is independent of potential source locations, increasing the number of measurement conditions improves the conditioning of the problem (Crenna et al., 2008; Flesch et al., 2009).

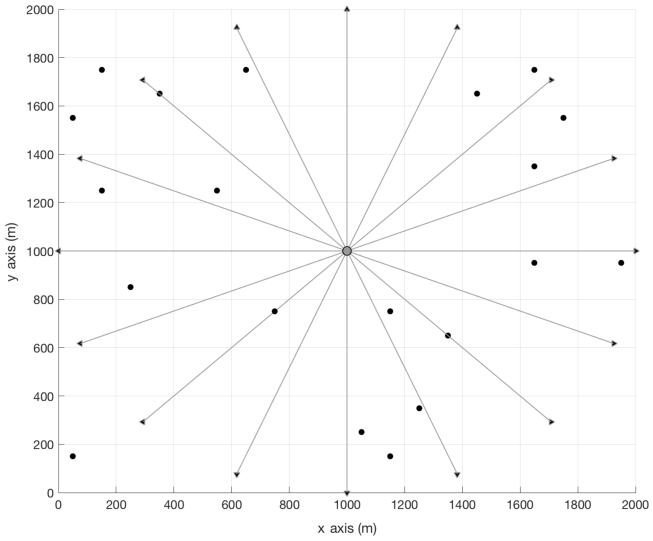

Figure 2. Map view of synthetic tests, with 20 source locations shown as black dots and 16 beams shown as gray lines that extend from the spectrometer (circle at $x = 1000$ m and $y = 1000$ m) to retroreflectors (black triangles).

2.5.3 Measurement system configuration and synthetic observations

The "synthetic" atmospheric measurements are simulated based on the dual frequency comb spectrometer observing system described in Sect. 2.2. The spectrometer is located in the center of the domain, at $x = 1000$ m and $y = 1000$ m (Fig. 2). Configurations of 4, 8, 16, 32, and 64 beams per spectrometer–detector system are tested. In all beam configurations, retroreflectors are placed at an equal distance (1000 m) from the spectrometer and at equal distances from neighboring retroreflectors (e.g., Fig. 2). The hub-and-spoke beam configuration is a simple and repeatable pattern for comparison of different numbers of beams. The height of the spectrometer and retroreflectors is 3 m above ground level (m a.g.l.). Figure 2 shows beams, beam end point locations (retroreflectors), and the spectrometer in a case with 16 beams.

The vector of "true" atmospheric methane concentrations, $\boldsymbol{c}$, is simulated by combining knowledge of atmospheric transport with knowledge of "true" sources and measurement (beam segment) locations with Eq. (1). The influence functions describing the relationships between each element of $\boldsymbol{x}$ and each segment of each beam path for each wind condition, $\mathbf{H}$, are created using the Gaussian plume model described in Sect. 2.1, with neutral stability conditions (Pasquill category D). In order to generate the synthetic measurement data, each beam path is discretized into 100 segments. For each unique wind condition, "true" source fluxes are multiplied by $\mathbf{H}$ to calculate atmospheric enhancements at each of the 100 points along the beam path. Enhancements due to leaks are calcu-

lated independently for each segment of a beam and subsequently averaged for each beam and for each wind condition. This value mimics the actual data output of the spectrometer, which measures the average concentration along the beam length.

The dimensions of n (e.g., the length of the atmospheric concentration vector, $\boldsymbol{c}$) in the synthetic tests vary along with the number of beams per spectrometer–detector system and the number of meteorological conditions. In the configuration of four beams, for example, $n = 216 \times 4$, because each distinct meteorological condition is applied to each beam. In the 8-beam configuration $n = 216 \times 8$, in the 16-beam configuration $n = 216 \times 16$, and so on.

2.5.4 Perturbation of observations with noise equivalent to model–data mismatch uncertainty

Model–data mismatch is the difference between the true atmospheric CH_4 concentration, $\boldsymbol{c}$, and the simulated or measurable atmospheric CH_4 concentration. This difference is expected to be non-zero due, for example, to measurement uncertainty (sampling and instrumental error), transport uncertainty (imperfect knowledge of air flow between source and observation points), and representation error (for example, the assumption that the measured segment of beam appropriately characterizes the atmospheric concentration at the time and space scales that it represents in the model). We assume here that uncertainty due to the imperfectly known background concentration is also part of model–data mismatch uncertainty. We simulate progressively larger levels of model–data mismatch in order to identify differences in model capabilities to locate and size leaks between the NZMB and non-bootstrap methods.

A range of model–data mismatch values are tested with the expectation that both the NZMB and non-bootstrap models will be more likely to locate and source leaks when lower model–data mismatch is added to the data. To simulate different possible magnitudes of model–data mismatch, the simulated true atmospheric concentrations, $\boldsymbol{c}$, are perturbed with random Gaussian noise with mean 0 ppb and standard deviation equal to the following values: 0.1, 0.2, 0.3, 0.4, 0.5, 1.0, 1.5, 2.0, 2.5, 3.0, 3.5, 4.0, 4.5, 5, 6, 7, 8, 9, and 10 ppb, over a 1 km path. Measurement statistical uncertainty alone is expected to be on the order of 3 ppb or lower for a 1 km path (Rieker et al., 2014). As the results of field tests will show, the range of model–data mismatch values tested are an appropriate approximation of observed uncertainty (Sect. 4.4). Model–data mismatch uncertainties are assumed to be uncorrelated, following convention and understanding of the dual frequency comb measurement scheme. In Eq. (5), $\boldsymbol{\epsilon}$ is a vector of model–data mismatch uncertainty corresponding to the vector, $\boldsymbol{c}$. Both vectors are of length n ($i = 1,\ldots,n$), where n is the number of observations, as described in Sect. 2.5.3. The vector $\boldsymbol{y}$ contains the synthetic observations or the true atmospheric concentrations perturbed with measurement noise.

$$y_i = c_i + \epsilon_i \tag{7}$$

2.6 Field data observations

2.6.1 Description of field-deployed dual comb setup

The first measurements from a field-deployed dual frequency comb spectrometer are from the NOAA/ESRL Table Mountain Test Facility, 10 km north of Boulder, Colorado (Fig. 3; Coburn et al., n.d.). The spectrometer is located near the center of a large ($\approx 3 \times 2.5$ km) flat-topped mesa that rises several meters above the surrounding terrain (see Fig. 3). The dual frequency comb is housed inside of a trailer, with telescope transceiver affixed to a rotating gimbal on the trailer roof (roughly 4 m a.g.l.). The actual dual frequency comb spectrometer is contained in a $56 \times 56 \times 61$ cm electronics rack, and the large trailer provides a field deployment home base. The beam transceiver system sends light between 1620 and 1680 nm, with discrete line spacing of 0.002 nm, through a 2 in. telescope. Dual comb spectroscopy uses a large spectral bandwidth and high spectral resolution, which allows for the simultaneous fitting of the absorption pattern for each gas, so that interference among gases is avoided. Background infrared light does not affect the laser signal due to the heterodyne nature of the detection – the detected beat signals between the comb teeth are of high frequency whereas background signals (for example from solar radiation) are of lower frequency. The system emits and senses approximately 28 900 individual comb teeth (Coburn et al., n.d.; Rieker et al., 2014). The wavelength "window" to which the instrument at Table Mountain is tuned is ≈ 50 nm, spanning 625 individual CH_4 features, 2482 CO_2 features, and 133 H_2O features. Intensity feedback, triggered data acquisition, and onboard phase correction are quasi-autonomous, enabling the system to operate continuously for any length of time (Coburn et al., n.d.; Truong et al., 2016; Waxman et al., 2017).

2.6.2 Leak location and strength

For the field experiments at Table Mountain, a cylinder of compressed methane gas is placed roughly 528 m away from the spectrometer (Fig. 3) with the gas outlet 1 m a.g.l. The methane cylinder is outfitted with a regulator and an Alicat mass flow controller (MC-20SLPM-D). The flow controller is set to release methane in a controlled flow of 3.1×10^{-5} kg s^{-1} at source location 1, between 10:08 and 16:30 on 26 January 2017. The flow rate at source location 2 is set to 0.0 kg s^{-1} through the duration of 26 January 2017. The controlled methane release point is roughly 0.43 cm in diameter, and the velocity of gas exiting the tubing is negligible.

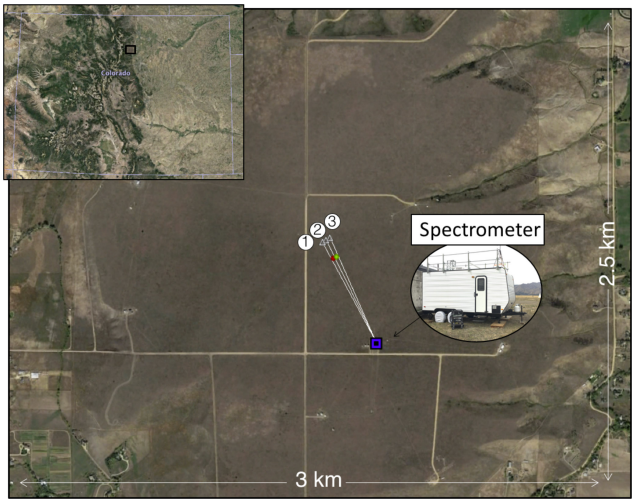

Figure 3. Map view of observation test site at Table Mountain, Colorado (upper left inset shows geographic location of test site), with two source locations (location 1, in red, between beams 1 and 2; location 2, in green, between beams 2 and 3) and three beams shown as white lines that extend from the spectrometer (blue square) to retroreflectors (white triangles, labeled 1–3).

The field tests are arranged so as to approximate the synthetic tests as closely as possible: to emulate the "perfect" background condition of the synthetic tests, the background methane concentration for each source location is measured directly by an upwind beam (Crenna et al., 2008; Flesch et al., 2009). Because the background is assumed to be unique for each source location, each inversion includes only that source location in its solution for fluxes. That is, one inversion is performed for source location 1, and a separate inversion is performed for fluxes at source location 2. The dimensions of m for each test are, therefore, equal to 1, and the dimensions of n for each test are equal to the number of measurements made downwind of the source location.

2.6.3 Retroreflector locations

Three corner-cube retroreflectors are located near source locations 1 and 2 at Table Mountain (see Fig. 3). At their nearest points, the lateral distances between beams 1 and 2 and source location 1 are 11 and 6 m, respectively. The minimum lateral distances between leak location 2 and beams 2 and 3 are 12 and 8 m, respectively. The horizontal distance from the spectrometer to each retroreflector is 584, 585, and 588 m, respectively, for retroreflectors 1, 2, and 3. All retroreflectors are positioned 1 m a.g.l.

2.6.4 Meteorology at Table Mountain

Wind speed and wind direction are measured directly with a 3D Sonic Anemometer (RM Young 81000 Ultrasonic 3D Anemometer with manufacturer-specified accuracy of $\pm 0.05\,\mathrm{m\,s^{-1}}$) located mid-way between the spectrometer and the retroreflectors. It is possible that local wind circulation could lead to meteorological conditions that are not homogenous across the Table Mountain site, which could cause the mean winds measured at the anemometer to not perfectly represent those influencing the plume. Measurement of the entire wind field is not practical, however, so the point measurement is used to characterize meteorology across the site. The suitability of the Gaussian plume model for short-range simulations decreases under low speeds, so all data taken at wind speeds below $0.8\,\mathrm{m\,s^{-1}}$ were removed from this analysis (the reliability of the Gaussian plume model erodes as wind speeds decrease below $\approx 1\,\mathrm{m\,s^{-1}}$; e.g., De Visscher, 2013).

2.6.5 Measurements

We test the bootstrap methodology using measurements taken over the course of 1 day in January 2017. We test the ability of the bootstrap approach to both disprove the null hypothesis (i.e., to correctly ascertain the presence of a non-zero methane emission) and to prove the null hypothesis (i.e., to correctly ascertain the absence of a leak) by gathering measurements along beam paths that bound (1) source location 1, where methane is released in a controlled flow rate of $3.1 \times 10^{-5}\,\mathrm{kg\,s^{-1}}$, and (2) source location 2, where no methane is released. Quasi-continuous (626 Hz) data acquisition occurs for 2 min on each beam. Time averaging over 2 min is performed to maximize gains in measurement precision as well as to average across shorter timescale eddy mixing events. After a measurement is taken, less than 30 s elapse while the gimbal moves to focus the beam on the next retroreflector ("retro") in the measurement sequence. The measurement sequence for the time period of study on 26 January 2017 is retro 1, retro 2, retro 1, retro 3, retro 1, retro 2, and so on. A fourth retroreflector is included in the measurement sequence (leading to a small time delay between measurements made on retro 3 and retro 2), but data from that beam are not analyzed here for simplicity.

In the field tests, the dimensions of n vary along with the number of measurements taken on the beams used in the fit for the methane emission rate vector, $\boldsymbol{x}$. For the fit to the methane emission rate at source location 1, all data (that is, all 2 min measurements) gathered on retroreflectors 1 and 2 are used. For the fit to the emission rate at source location 1, all data gathered on retroreflectors 2 and 3 are used. Upwind measurements are used to constrain background, and downwind measurements are used to determine source strength. The dimensions of n are therefore equal to the number of downwind measurements. For the test at source location 1, $n = 63$, and for the test at source location 2, $n = 30$. The value of n is smaller at source location 2 because of the sampling pattern described above.

2.6.6 Background CH_4 estimation

To most closely approximate the synthetic data testing framework in the field environment, we directly sample background CH_4 concentrations upwind of the leak point. The array of beams shown in Fig. 3 "sandwich" each source location. This configuration means that under most wind conditions (wind directions within $\approx 40°$ of orthogonal to the beam array in either direction), one beam is situated upwind and one beam is situated downwind of each source location. With this method, we attempt to remove the time-varying CH_4 concentration to which enhancements from discrete near-field emissions are added. While the Table Mountain site is relatively removed from expected anthropogenic and biogenic methane sources, the presence of nearby small livestock and oil and gas operations means that the background methane concentration does vary according to wind direction and through time. The "beam sandwich" approach, of placing beams on either side of each source location, represents a plausible solution to future regional-scale monitoring of many potential emitters.

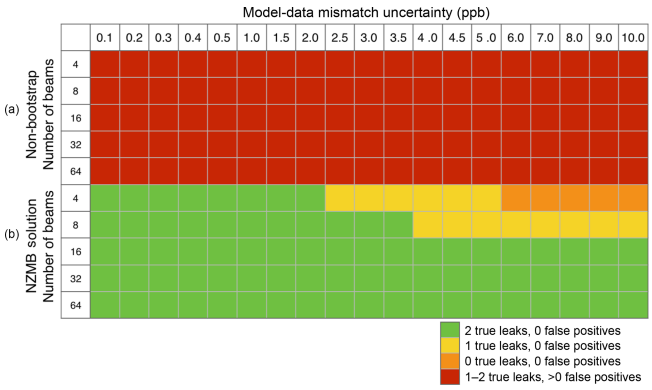

Figure 4. Summary of synthetic data test results. Top 5 rows show results of non-bootstrap inversions and bottom 5 rows show results of NZMB inversions for the 4, 8, 16, 32, and 64 beam cases. Columns indicate results for different values of model–data mismatch added as noise to the synthetic measurements. Color coding of cells indicates summary of model success, as detailed by the legend.

3 Results of synthetic data tests

3.1 Synthetic source location with and without the NZMB method

We calculate solutions for $\boldsymbol{x}$ using NNLS in a single solution without a bootstrap approach for each set of beam configurations and for each model–data mismatch scenario in the synthetic data case. Figure 4 summarizes the findings of each test by categorizing the results into four outcomes: two true leaks found with no false positives, one true leak found with no false positives, zero true leaks found with no false positives, and one or more true leaks found with one or more false positive. The top half of Fig. 4 (for the non-bootstrap method) shows that, of the five different beam configurations tested, all result in false-positive source locations under every model–data mismatch scenario when a non-bootstrap approach is taken. That is, even with very low model–data mismatch (0.1 ppb) and many beam measurement locations (64), the non-bootstrap method fails to positively identify true leak sources without also generating false-positive results. Non-zero solutions are found for source locations where no "true" leak exists.

The bottom half of Fig. 4 shows the results of the same tests, using instead the NZMB method for locating leaks. The results show that success in leak detection is much higher using NZMB compared with the non-bootstrap tests. Indeed, none of the NZMB tests result in the occurrence of a false-positive leak location, and only tests with low numbers of beams relative to the number of source locations (four- and eight-beam cases) fail to find both of the true leaks. The four-beam case results in positive identification of both leaks up to a model–data mismatch threshold of 2 ppb, above which one true leak is found. One leak is consistently found up to a threshold of 5 ppb, and above 5 ppb model–data mismatch no true leaks are identified (but no false positives are generated either). The eight-beam case results in accurate location of both true leaks up to a model–data mismatch threshold of 3.5 ppb, above which 1 true leak is found (with no false positives). One leak is consistently found up to the maximum testing point of 10 ppb. In order to reliably locate both true leaks with no false-positive results under all model–data mismatch scenarios, 16 or more beams are needed for the set of cases that are tested here. Alternate configurations of "true" leaks at well sites other than 6 and 9 are not tested; however, given that meteorological conditions are simulated equally from all directions, we would not expect a different set of results from a different set of "true" leaks.

A subset of the results for the eight-beam NNLS without bootstrap and the NNLS with NZMB cases are shown in Figs. 5 and 6 (for conciseness; all results are shown in the Supplement). It is evident from Fig. 5 that, even with very low model–data mismatch noise (0.5 ppb), the non-bootstrap model results in well sites other than the two true leak locations being erroneously identified as sources of methane. It is evident from Fig. 5 that, as model–data mismatch increases, the strength of incident false-positive results also increases. By contrast, no false-positive leaks are identified in the NZMB case shown in Fig. 6, at any level of model–data mismatch noise. Above a model–data mismatch threshold of 4 ppb, only one of two true leaks is found in the eight-beam case using NZMB. As Fig. 4 shows, 16 or more beams are necessary to consistently find both true leaks at higher thresholds of model–data mismatch uncertainty using the NZMB method, given the hub-and-spoke beam placement scheme tested here. More complex placement of beams (for example

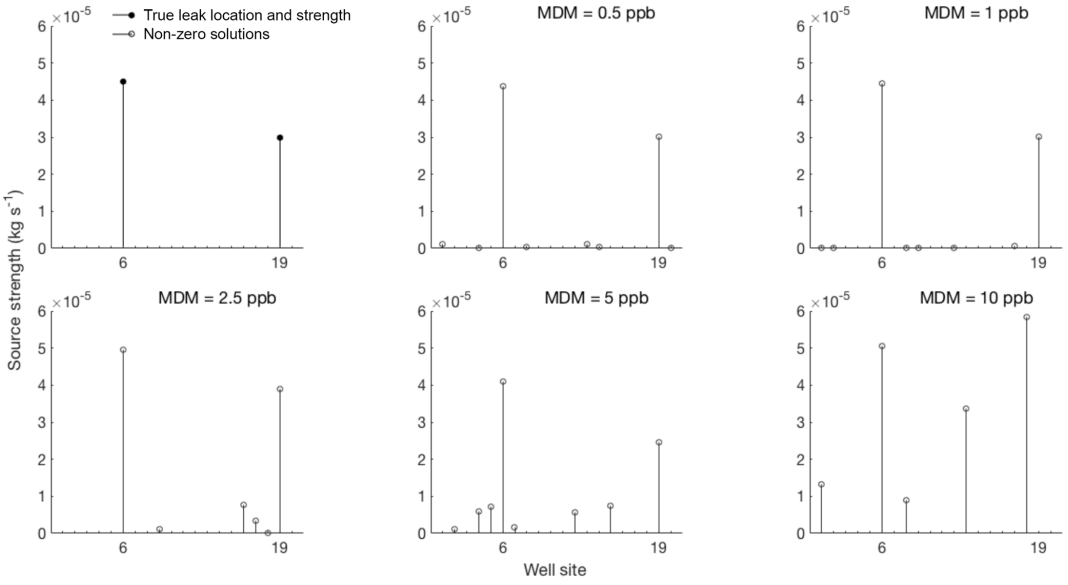

Figure 5. Top left panel shows well site numbers (x axis) and corresponding "true" leak rates (y axis), and remaining panels show resulting leak rate (y axis) at each well site (x axis) from non-bootstrap least squares fit to synthetic observations perturbed with model–data mismatch (MDM) noise shown, for the eight-beam case. Open circles show locations and strengths of all non-zero solutions.

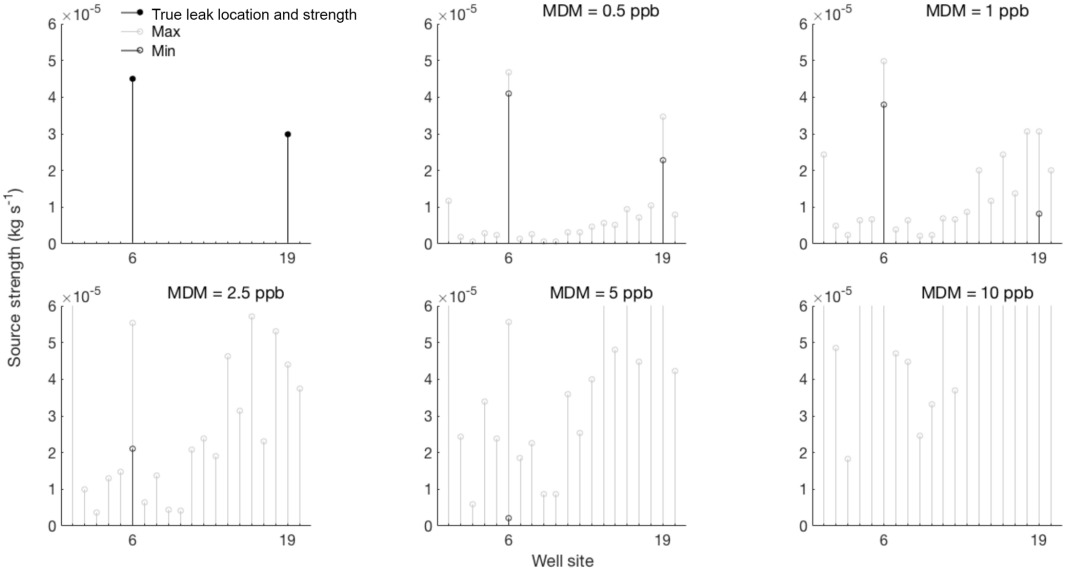

Figure 6. Top left panel shows well site numbers (x axis) and corresponding "true" leak rates (y axis), and remaining panels show NZMB results (y axis) for each well site location (x axis) with synthetic observations perturbed with model–data mismatch (MDM) noise shown, for the eight-beam case. Light gray (black) open circles show locations and strengths of the maximum (minimum) of 1000 bootstrap operations. Minimum values of zero are not plotted.

placing beams closer to known well sites) would likely result in even better ability to locate leaks with fewer beams.

3.2 Synthetic source sizing using the NZMB method

Synthetic data tests of the new bootstrap methodology presented here show high success in leak location, with zero incidence of false-positive leak detections. Figure 6 shows the maximum and minimum values of 1000 bootstrap operations for each model–data mismatch test case for the eight-beam configuration. At low levels of model–data mismatch uncertainty (0.1–0.5 ppb), the maximum and minimum solutions bound a small range that is close to the true leak strength. As higher levels of model–data mismatch noise are added to observations, the maximum and minimum values diverge.

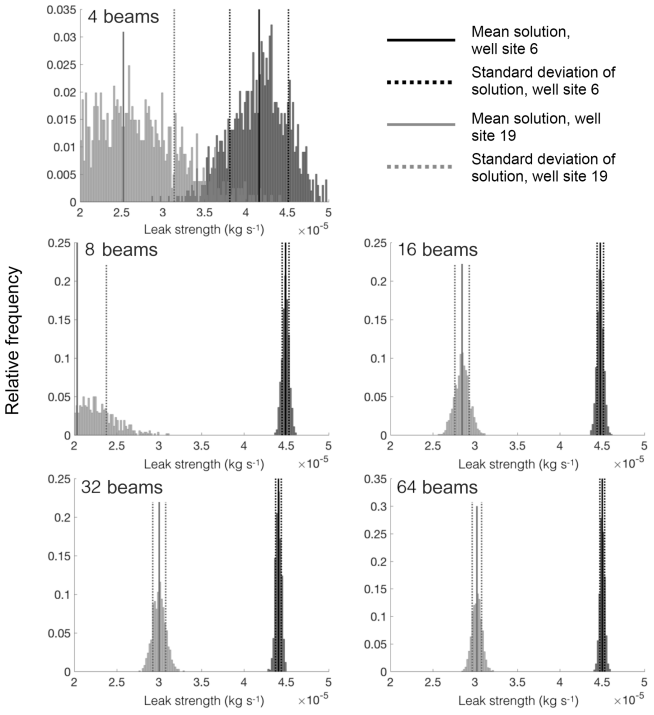

Figure 7. Histograms of source strength, with mean ± 1 standard deviation shown with vertical lines for well site 6 (black) and well site 19 (gray), for each beam configuration, and with 2 ppb model–data mismatch uncertainty. Note that x axes are truncated at 2×10^{-5} kg s^{-1} (lower bound) and 5×10^{-5} kg s^{-1} (lower bound) for scale.

However, even as the maximum and minimum solutions diverge, most cases include the true leak strength within the maximum and minimum bounds.

Using the NZMB method, all beam cases (even the four-beam case) correctly identify that both well sites 6 and 19 are emitting methane when model–data mismatch is 2 ppb or lower (Fig. 4). At that level of model–data mismatch, higher numbers of beams and observations tend to lead to lower standard deviation around the mean estimated leak strength and a more accurate estimate of true leak strength (Table 1). An exception is at well site 19, where the eight-beam case did not perform as well as the four-beam case. It may be that both cases were inadequate for accurately sizing leaks, and that 16 beams are necessary in a dense field of wells such as is tested here. The failure of the eight-beam case to accurately predict the leak rate at well site 19 is also evident from histograms of bootstrap operations, shown for each beam case with model–data mismatch of 2 ppb in Fig. 7.

Histograms of the results for the 16, 32, and 64 beam cases with 10 ppb model–data mismatch are shown in Fig. 8. It is clear from Fig. 8 that, even with very high model–data mismatch uncertainty, simple hub-and-spoke configurations of between 16 and 64 beams are able to locate and estimate leak flow rates to within reasonable bounds of uncertainty.

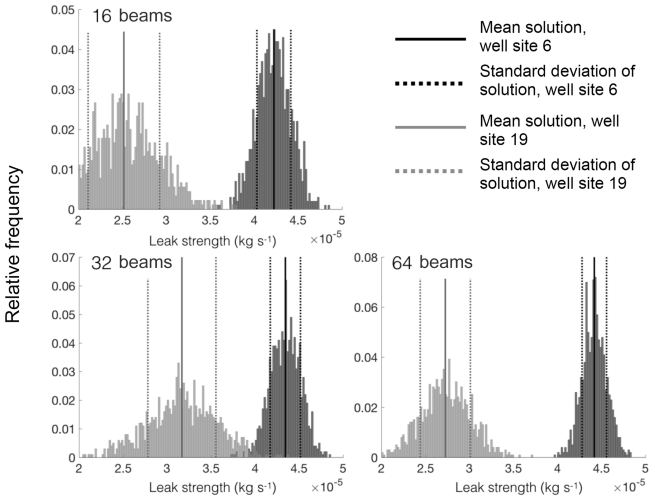

Figure 8. Histograms of source strength, with mean ± 1 standard deviation shown with vertical lines for well site 6 (black) and well site 19 (gray), for 16, 32, and 64 beam configurations, and with 10 ppb model–data mismatch uncertainty.

4 Results of field data tests

4.1 Performance overview of field-deployed DCS

Atmospheric observations were made over the course of 1 day on 26 January 2017 at the Table Mountain site. A set of three retroreflectors created long-range open-path beams of ≈ 585 m (Fig 3). Spectrometer performance in the field demonstrated no loss of precision or reliability compared with laboratory performance, as demonstrated by Coburn et al. (n.d.). Figure 9 shows a plot of Allan deviations for 26 January 2017, demonstrating measurement precision of 5–6 ppb when measurements are averaged for 2 min. Precision of field measurements is limited by repeatability of measurements and atmospheric variability of CH_4 because measurements are time averaged; the latter is likely a dominant driver of uncertainty in this case, as will be discussed in Sect. 4.3. The Allan deviation in Fig. 9 shows improvement of precision with averaging time, to a minimum at ≈ 70 s, followed by an increase that is likely due to atmospheric variability.

4.2 Atmospheric observations of CH_4 at Table Mountain

On 26 January 2017, measurements are made throughout the day, including during a 6.5 h controlled release of methane at source location 1. At adjacent source location 2, no methane release is emitted. A series of three retroreflectors is oriented such that each source region is monitored independently from the other; one beam on either side of each source location serves as a "background" measurement. We examine the results of two separate inversion tests: (1) a day-long set of observations of source location 1 (with the controlled

Table 1. NZMB solutions for leak strength of true leaks, given 2 ppb model–data mismatch uncertainty, for each beam configuration.

Number of beams	Well site 6 mean strength	Well site 6, 1 SD	Well site 19 mean strength	Well site 19, 1 SD
4	4.2×10^{-5} kg s^{-1}	0.4×10^{-5} kg s^{-1}	2.5×10^{-5} kg s^{-1}	0.6×10^{-5} kg s^{-1}
8	4.5×10^{-5} kg s^{-1}	0.4×10^{-6} kg s^{-1}	2.0×10^{-5} kg s^{-1}	0.3×10^{-5} kg s^{-1}
16	4.5×10^{-5} kg s^{-1}	0.4×10^{-6} kg s^{-1}	2.8×10^{-5} kg s^{-1}	0.9×10^{-6} kg s^{-1}
32	4.4×10^{-5} kg s^{-1}	0.3×10^{-6} kg s^{-1}	3.0×10^{-5} kg s^{-1}	0.8×10^{-6} kg s^{-1}
64	4.5×10^{-5} kg s^{-1}	0.3×10^{-6} kg s^{-1}	3.0×10^{-5} kg s^{-1}	0.6×10^{-6} kg s^{-1}
	True leak: 4.5×10^{-5} kg s^{-1}		True leak: 3.0×10^{-5} kg s^{-1}	

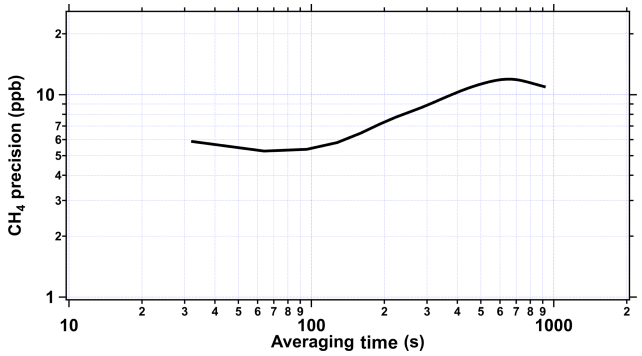

Figure 9. Allan deviation plot showing changes in measurement precision with averaging time from field data collected at Table Mountain on 26 January 2017.

release) that is situated between retroreflectors 1 and 2 and (2) a day-long set of observations of non-leaking source location 2 that is situated between retroreflectors 2 and 3. These tests are performed simultaneously, such that contamination from source location 1 could result in background contamination for monitoring of source location 2.

On 26 January 2017, mean wind speeds are 2.1 m s^{-1} and winds are primarily from the east and northeast, so that retroreflector 1 is downwind of the controlled release and retroreflector 2 is upwind of the controlled release. Similarly, retroreflector 2 is downwind of non-leaking source location 2 and retroreflector 3 is upwind of non-leaking source 2 (Fig. 3). Stability classes range from B (moderately unstable) to D (neutral) throughout the course of the day (see Supplement for a time series of stability and detailed description of its calculation). We use the Griffiths (1994) corrections to the Briggs (1974) parameterizations to calculate σ_y and σ_z.

At source location 1 (Fig. 10a), during the period when the controlled release is on (non-zero flow), the downwind retroreflector (Retro 1) shows a clear enhancement above the concentration measured on the upwind retroreflector (Retro 2), except during the middle of the day when the winds shift briefly to the south (Fig. 10c). The mean of all CH_4 measurements along beam 1 during the period that the leak is on is 2046 ppb; the mean CH_4 measured along beam 2 during the same period is 2025 ppb. Both retroreflectors demonstrate changes in background CH_4 concentrations over the course of the day; the range in values measured on the upwind retroreflector is 65 ppb. There may be a relationship between ambient CH_4 concentration and wind direction, as both retroreflectors show a drastic decrease in concentration when the winds abruptly shift to the west at 16:30 (which happens to coincide with the time the leak was turned off).

At source location 2, no leak is released during the period of study, and throughout the course of the day, both retroreflectors 2 and 3 measure similar changes in atmospheric CH_4 variability (Fig. 10b). The range of measured values over the course of the entire day are 128 ppb on beam 2 and 124 ppb on beam 3. The mean of all CH_4 measurements (throughout the course of the day) is 2016 ppb on beam 2 and 2019 ppb on beam 3.

4.3 Background CH_4 observations

The beams stationed upwind of each source location provide estimates of the background CH_4 concentration inflow for that location. After a linear interpolation to upwind measurements has been applied, this background is subtracted from measurements on the downwind beam to yield a measure of the CH_4 enhancement due to fluxes at the source location. Applying this method, the mean and standard deviation of the enhancement above background on retroreflector 1 – which is downwind of source location 1 (leak rate of 3.1×10^{-5} kg s^{-1}) – is 17.4 ± 10.1 ppb. Applying this method to source location 2, we find the mean and standard deviation of the enhancement on retroreflector 2 – which is downwind of source location 2 (leak rate of 0 kg s^{-1}) – is 3.1 ± 7.3 ppb, a value within the range of variability expected from combined measurement and background uncertainty.

4.4 Field-based estimates of model–data mismatch

We examine measurements at source location 2, where no leak is present, in order to estimate model–data mismatch in the field, for comparison with the model–data mismatch values applied in the synthetic data tests. By examining the difference between measurements made on different retrore-

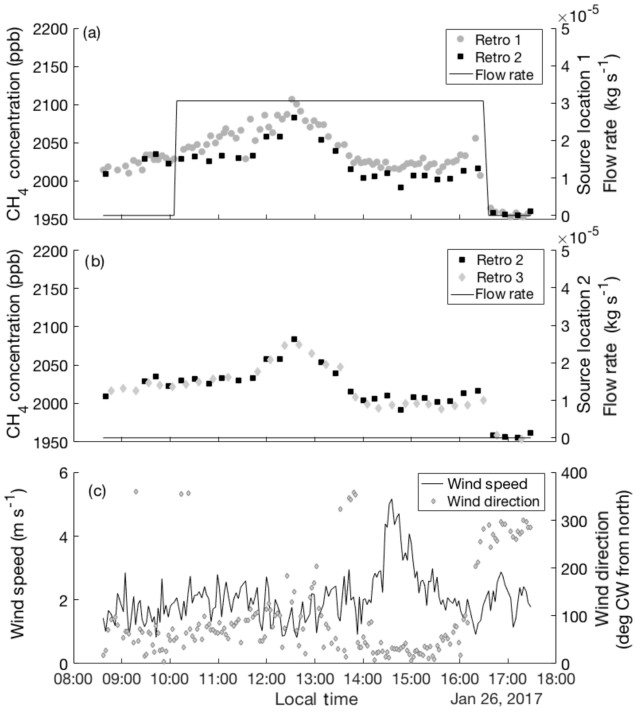

Figure 10. Line-integrated atmospheric CH_4 concentrations measured on 26 January 2017 along beam paths to retroreflectors 1 and 2 **(a)** and to retroreflectors 2 and 3 **(b)**, as well as wind speed and wind direction **(c)**. Gray and black points and left-hand axes of panels **(a)** and **(b)** show CH_4 concentration. The black line and right-hand axis in panel **(a)** show the flow rate at source location 1 (bounded by retroreflectors 1 and 2) and the black line and right-hand axis in panel **(b)** show the flow rate at source location 2 (bounded by retroreflectors 2 and 3). In panel **(c)**, the black line and left-hand axis show wind speed and the gray diamonds and right-hand axis show wind direction (according to meteorological convention, 0° is north, 90° is east, 180° is south, 270° is west, and 360° is north). All data reflects 2 min averaging time.

flectors (retroreflectors 2 and 3) at similar points in time (within 5 min), we obtain an approximation of the combined contributions to model–data mismatch arising from measurement uncertainty, representation uncertainty, background construction (the method of background estimation), and background sampling (the method of sampling background concentrations). We find a standard deviation of 5 ppb. This value differs from the standard deviation of the enhancement for the entire time series (reported above in Sect. 4.3) because it compares differences in upwind and downwind concentrations measured at approximately the same time. For estimation of total model–data mismatch, we add (in quadrature) an estimate of the transport uncertainty that includes uncertainties in measurement of wind speed and wind direction, atmospheric stability parameterization, and placement of the sonic anemometer relative to the leak location (see Supplement for detail). Transport uncertainty estimation is for a plume that interacts with any location along the beam and therefore requires knowledge of the mean distance between the leak point and each segment of the beam. The estimated transport uncertainty, calculated in this way, is 0.8 ppb. If, for example, the wind direction is perfectly perpendicular to the beam for the entirety of the measurement period (which does not occur on 26 January 2017), then the leak-to-beam distance used in the calculation should collapse to the minimum lateral distance between the leak and the beam. Using that value instead, transport uncertainty is 12.2 ppb. The overall value of model–data mismatch (reflecting combined measurement, background, and transport uncertainty), estimated in this way, is therefore 5.1 ppb with a maximum range of 13.2 ppb, which suggests that the range of model–data mismatch values tested in the synthetic data experiments are appropriate. The Allan deviation in Fig. 9 shows a similar level of measurement uncertainty, suggesting that most of the uncertainty observed in our record is captured in this estimate of model–data mismatch, which includes effects of atmospheric variability. Precision could be improved by averaging data over a shorter time span (70 s), but those gains would be minimal (Fig. 9).

4.5 Results of inversions using Table Mountain observations

Both the non-bootstrap and the NZMB approaches accurately predict the presence of methane emissions at source location 1 (Table 2). The average bootstrapped flux value is within 2σ of the true flux value measured at the flow meter at source location 1 (Fig. 11). At source location 2, the non-bootstrap approach falsely predicts a positive emission rate of 0.5×10^{-5} kg s^{-1} (Table 2) where no leak is present. The NZMB approach, by contrast, is able to accurately predict that there is no leak present at source location 2, because the minimum of the 1000 bootstrap solutions is zero (Fig. 11). As the synthetic data tests also demonstrate, the NZMB method is necessary to avoid false identification of leaking source locations. The field data tests corroborate that the new bootstrap approach enables higher confidence of accurate attribution of emissions to source locations without generating "false alarms".

5 Discussion

The results of this study demonstrate success of the new observing system in finding one or more leaks of methane in a field of wells, using synthetic and field data for confirmation. The methods presented here for locating and sizing leaks of methane in a field of natural gas production facilities succeeds not only in identifying the location of a leak, but it also does so with no incidences of "false-positive" leak detection in either the synthetic or field data tests.

Table 2. Controlled methane release flow rates and 1 standard deviation for each field experiment, including local time that leak was turned on and off.

	Source location 1	Source location 2
Controlled leak time on:	10:08	n/a
Controlled leak time off:	16:30	n/a
Measured mean flow rate:	$3.1 \times 10^{-5} \pm 0.01 \times 10^{-5}$ kg s^{-1}	0.0 ± 0.0 kg s^{-1}
Non-bootstrap solution:	2.4×10^{-5} kg s^{-1}	0.5×10^{-5} kg s^{-1}
NZMB solution:	$2.6 \times 10^{-5} \pm 0.5 \times 10^{-5}$ kg s^{-1}	0.0 ± 0.0 kg s^{-1}

n/a: not applicable.

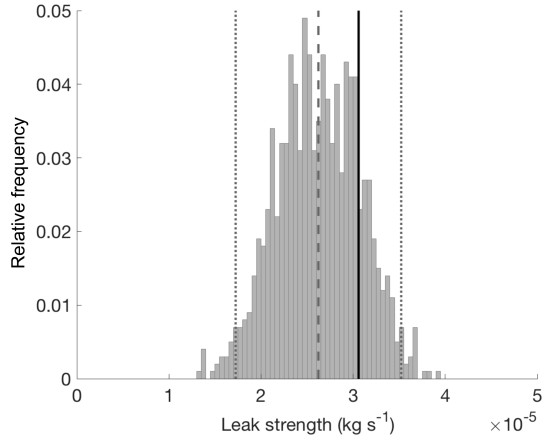

Figure 11. Histogram of NZMB estimated source strength at source location 1, with dashed line showing the bootstrap mean and thin dotted lines showing ±2 standard deviation. The thick black line shows the true leak strength at source location 1 (3.1×10^{-5} kg s^{-1}).

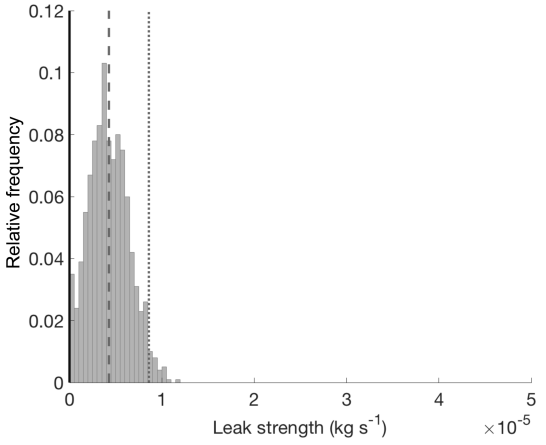

Figure 12. Histogram of NZMB estimated source strength at source location 2, with dashed line showing the bootstrap mean and thin dotted lines showing ±2 standard deviation. The thick black line shows the true leak strength at source location 2 (0 kg s^{-1}). The presence of 0 kg s^{-1} in the histogram triggers acceptance of the null hypothesis (that the emissions rate at this site is zero).

5.1 Synthetic data tests

The results of the synthetic data tests demonstrate how the observing system tested in the field for a single source location can be expanded for simultaneous monitoring of many source locations. We find that synthetic tests performed without the NZMB methodology failed to identify the presence of leaks as reliably as synthetic tests performed with the NZMB method, demonstrating the improved robustness of this new statistical method for leak detection. In the non-bootstrap tests, all synthetic data cases resulted in false-positive solutions (Fig. 4). By contrast, the NZMB method succeeds in correctly identifying two leaks of strength 3.0×10^{-5} and 4.5×10^{-5} kg s^{-1} with four or more beams monitoring 20 wells in a 4 km^2 area, with 2 ppb model–data mismatch uncertainty (a condition that could conceivably also be met in the field given low background uncertainty and high measurement precision). The NZMB method also consistently succeeds in finding both leaks with 16 or more beams with at least 10 ppb model–data mismatch uncertainty. Notably, the NZMB method locates and sizes both leaks with no false-positive results. Determination of leak strength was successful to within 25 % (and all but a few cases well below 10 %) for all cases with 16 or more beams, using the NZMB method.

5.2 Field data tests

Field data testing of the NZMB method corroborates the synthetic data findings: that the new atmospheric observing system presented here results in high accuracy of leak detection without false-positive results. The ability of the dual frequency comb spectrometer to identify a very small leak (3.1×10^{-5} kg s^{-1}), relying on very small methane enhancements (17 ppb) against a highly variable background (range of 65 ppb), demonstrates the potential utility of this method for methane leak detection over large areas.

An important caveat to the methodology presented here is the short length of the measurement averaging time, which presents a mismatch with the ideal application of most dispersion models (for which practice is generally to use averaging times longer than 2 min). This requirement in our

methodology is due to two factors: the first is that rapid scanning for potential leaks is an important feature in areas where many sites must be monitored and leaks can be intermittent. The second factor is that background methane concentrations can vary with high frequency (order minutes) in proximity to areas of oil and natural gas production (Dlugokencky et al., 1995). We attempt to mitigate uncertainties arising from using dispersion parameters developed for longer timescale modeling over a 2 min period in several ways. First, n 2 min dispersion calculations gathered over longer timescales (n is between 30 and 63 for field data tests shown here) are aggregated for use in a single inversion, which is accepted practice (Scire et al., 2000). Second, both sources and receptors are close to the surface, which may help to mitigate crosswind-integrated concentration fluctuation intensity (Weil et al., 2012). Third, a sensitivity test in which we adjust the horizontal dispersion coefficient, σ_y, for shorter time averaging, using the methods of Gifford (1976), shows negligible changes in the results (Supplement). We find that the potential value of a method for rapid detection of methane emissions over large scales and against a highly variable background means that the uncertainties introduced from modeled eddy diffusivity parameterization are a complicating but not irreconcilable caveat.

6 Conclusions

The focus of this study is to show the powerful potential of the combination of a new statistical method with dual frequency comb spectroscopy for the location and sizing of point source emissions. The synthetic and field tests presented here rely on near-perfect (in the synthetic data tests) or well-constrained (in the field data tests) background concentration estimation. Future studies are needed to address the potential complications of more complex background conditions and meteorological conditions under which it is not possible to obtain sequential "upwind" and "downwind" samples. Similarly, the tests here rely on the assumption of constant leak rates, which may not be a realistic assumption that can be made for methane emissions from oil and gas operations. Future work to address these complexities will be necessary. Future studies are also needed to examine the gains that can be made from optimization of beam configurations for improved leak detection given variable wind and background conditions. In particular, previous work has shown the critical impact that sensor placement can have on the conditioning of the source–receptor relationship matrix (**H**) and suggests paths forward for optimization of sensor placement (Crenna et al., 2008; Flesch et al., 2009). Specifically, the placement of one beam or sensor between each source to be apportioned would be expected to lead to a lower condition number and therefore a more reliable result (Crenna et al., 2008; Flesch et al., 2009). Work aimed at addressing these complications is underway, as are inversion efforts to resolve issues of leak intermittency.

A notable aspect of the micrometeorological modeling used here to demonstrate the NZMB methodology is the simple representation of atmospheric transport (the Gaussian plume model). The choice to use a simple model that is familiar to the broader scientific community is intentional, but its use belies the complex nature of turbulent mixing and dispersion in the atmospheric surface layer. What is gained in simplicity and in providing a baseline for the most basic performance of the methodology in a field setting may come at the cost of recommending a model that may not ultimately be well-suited for such an endeavor. The Gaussian plume model neglects important aspects of atmospheric mixing such as wind shear and the height dependence of eddy diffusivity, and better models exist for simulation of atmospheric flow at this scale. It is assumed that more sophisticated models of atmospheric dispersion could, therefore, lead to better flux estimation. We suggest that future applications in field settings of the methodology presented here consider their use. Importantly, despite its drawbacks, the Gaussian plume model proves sufficient in the tests here for the accurate identification (and, importantly, avoidance of misidentification) of controlled, field-based methane leaks. Future studies of the best transport model for the application of DCS measurements and the NZMB method for leak detection is warranted.

The initial work presented here demonstrates the promising potential of dual frequency comb spectroscopy for detection of leaks in the natural gas supply chain and the valuable gains that can be provided by using the NZMB method over the NNLS fitting technique alone.

Data availability. Data are accessible at the following URL: ftp://aftp.cmdl.noaa.gov/user/alden/Alden_AMT_2018/.

The Supplement related to this article is available online at https://doi.org/10.5194/amt-11-1565-2018-supplement.

Author contributions. SG, KP, and CA implemented the statistical NZMB technique. CA, SC, RW, CS, KP, SG, and GR designed the experiments and SC, RW, and CA carried them out. AK provided expert guidance and experimental design input. CA prepared the manuscript with contributions from all co-authors.

Competing interests. The authors declare that they have no conflict of interest.

Acknowledgements. The information, data, or work presented herein was funded in part by the Advanced Research Projects Agency-Energy (ARPA-E), US Department of Energy, under Award Number DE-AR0000539. The views and opinions of authors expressed herein do not necessarily state or reflect those of the United States Government or any agency thereof.

Edited by: Dietrich G. Feist
Reviewed by: two anonymous referees

References

Allen, D. T., Torres, V. M., Thomas, J., Sullivan, D. W., Harrison, M., Hendler, A., Herndon, S. C., Kolb, C. E., Fraser, M. P., Hill, A. D., Lamb, B. K., Miskimins, J., Sawyer, R. F., and Seinfeld, J. H.: Measurements of methane emissions at natural gas production sites in the United States, P. Natl. Acad. Sci. USA, 110, 17768–17773, https://doi.org/10.1073/pnas.1304880110, 2013.

Allen, D. T., Sullivan, D. W., Zavala-Araiza, D., Pacsi, A. P., Harrison, M., Keen, K., Fraser, M. P., Hill, A. D., Lamb, B. K., Sawyer, R. F., and Seinfeld, J. H.: Methane Emissions from Process Equipment at Natural Gas Production Sites in the United States: Liquid Unloadings, Environ. Sci. Technol., 49, 641–648, https://doi.org/10.1021/es504016r, 2015a.

Allen, D. T., Pacsi, A. P., Sullivan, D. W., Zavala-Araiza, D., Harrison, M., Keen, K., Fraser, M. P., Hill, A. D., Sawyer, R. F., and Seinfeld, J. H.: Methane emissions from process equipment at natural gas production sites in the United States: pneumatic controllers, Environ. Sci. Technol., 49, 633–640, https://doi.org/10.1021/es5040156, 2015b.

Alvarez, R. A., Pacala, S. W., Winebrake, J. J., Chameides, W. L., and Hamburg, S. P.: Greater focus needed on methane leakage from natural gas infrastructure, P. Natl. Acad. Sci. USA, 109, 6435–6440, https://doi.org/10.1073/pnas.1202407109, 2012.

Akagi, S. K., Yokelson, R. J., Wiedinmyer, C., Alvarado, M. J., Reid, J. S., Karl, T., Crounse, J. D., and Wennberg, P. O.: Emission factors for open and domestic biomass burning for use in atmospheric models, Atmos. Chem. Phys., 11, 4039–4072, https://doi.org/10.5194/acp-11-4039-2011, 2011.

Brandt, A. R., Heath, G. A., Kort, E. A., O'Sullivan, F., Petron, G., Jordaan, S. M., Tans, P., Wilcox, J., Gopstein, A. M., Arent, D., Wofsy, S., Brown, N. J., Bradley, R., Stucky, G. D., Eardley, D., and Harriss, R.: Methane Leaks from North American Natural Gas Systems, Science, 343, 733–735, https://doi.org/10.1126/science.1247045, 2014.

Brantley, H. L., Thoma, E. D., Squier, W. C., Guven, B. B., and Lyon, D.: Assessment of Methane Emissions from Oil and Gas Production Pads using Mobile Measurements, Environ. Sci. Technol., 48, 14508–14515, https://doi.org/10.1021/es503070q, 2014.

Briggs, G. A.: Diffusion estimation for small emissions, in ATDL Contribution File No. 79, Air Resources Atmospheric Turbulence and Diffusion Laboratory, NOAA, Oak Ridge, Tennessee, 1974.

Coburn, S., Alden, C. B., Wright, R., Cossel, K., Baumann, E., Truong, G.-W., Giorgetta, F., Sweeney, C., Newbury, N. R., Prasad, K., Coddington, I., and Rieker, G. B.: Regional trace gas source attribution using a field-deployed dual frequency comb spectrometer, Optica, accepted, 2018.

Crenna, B. P., Flesch, T. K., and Wilson, J. D.: Influence of source – sensor geometry on multi-source emission rate estimates, Atmos. Environ., 42, 7373–7383, https://doi.org/10.1016/j.atmosenv.2008.06.019, 2008.

De Visscher, A.: Air Dispersion Modeling: Foundations and Applications, John Wiley & Sons, New York., 2013.

Dlugokencky, E. J., Steele, L. P., Lang, P. M., and Masarie, K. A.: Atmospheric methane at Mauna Loa and Barrow observatories Presentation and analysis of in situ measurements Edward, J. Geophys. Res., 100, 23103–23113, 1995.

Dobler, J., Zaccheo, T. S., Blume, N., Braun, M., Botos, C., and Pernini, T. G.: Spatial mapping of greenhouse gases using laser absorption spectrometers at local scales of interest, Proc. SPIE, 9645, 96450K1–9645K13, https://doi.org/10.1117/12.2197713, 2015.

Efron, B.: Bootstrap methods: Another look at the jackknife, Ann. Stat., 7, 1–26, https://doi.org/10.1214/aos/1176344552, 1979.

Environmental Protection Agency: Inventory of U.S. greenhouse gas emissions and sinks: 1990–2013, Washington, D.C., 2015.

Flesch, T. K., Wilson, J. D., and Yee, E.: Backward-Time Lagrangian Stochastic Dispersion Models and Their Application to Estimate Gaseous Emissions, J. Appl. Meteorol., 34, 1320–1332, https://doi.org/10.1175/1520-0450(1995)034<1320:BTLSDM>2.0.CO;2, 1995.

Flesch, T. K., Wilson, J. D., Harper, L. A., Crenna, B. P., and Sharpe, R. R.: Deducing Ground-to-Air Emissions from Observed Trace Gas Concentrations: A field trial, J. Appl. Meteorol., 43, 487–502, https://doi.org/10.1175/1520-0450(2004)043<0487:DGEFOT>2.0.CO;2, 2004.

Flesch, T. K., Harper, L. A., Desjardins, R. L., Gao, Z., and Crenna, B. P.: Multi-Source Emission Determination Using an Inverse-Dispersion Technique, Bound.-Lay. Meteorol., 132, 11–30, https://doi.org/10.1007/s10546-009-9387-1, 2009.

Frankenberg, C., Thorpe, A. K., Thompson, D. R., Hulley, G., Kort, E. A., Vance, N., Borchardt, J., Krings, T., Gerilowski, K., Sweeney, C., Conley, S., Bue, B. D., Aubrey, A. D., Hook, S., and Green, R. O.: Airborne methane remote measurements reveal heavy-tail flux distribution in Four Corners region, P. Natl. Acad. Sci. USA, 113, 9734–9739, https://doi.org/10.1073/pnas.1605617113, 2016.

Gifford, F. A.: Atmospheric dispersion models for environmental pollution, in Lectures on Air Pollution and Environmental Impact Analysis, edited by: Haigen, D. A., Boston, Mass, 35–58, 1976.

Green, A. E. S., Singhal, R. P., and Venkateswar, R.: Analytic Extensions of the Gaussian Plume Model, J. Air Pollut. Control Assoc., 30, 773–776, https://doi.org/10.1080/00022470.1980.10465108, 1980.

Griffiths, R. F.: Errors in the use of the Briggs parameterization for atmospheric dispersion coefficients, Atmos. Environ., 28, 2861–2865, https://doi.org/10.1016/1352-2310(94)90086-8, 1994.

Groth, A., Maurer, C., Reiser, M., and Kranert, M.: Determination of methane emission rates on a biogas plant using data from laser absorption spectrometry, Bioresource Technol., 178, 359–361, https://doi.org/10.1016/j.biortech.2014.09.112, 2015.

Hanna, S. R., Briggs, G. A., and Hosker Jr., Rayford P. J.: Handbook on atmospheric diffusion, edited by: Smith, J. S., Technical Information Center, US Department of Energy, 1982.

Hashmonay, R. A, Yost, M. G., Mamane, Y., and Benayahu, Y.: Emission rate apportionment from fugitive sources using open-path FTIR and mathematical inversion, Atmos. Environ., 33, 735–743, https://doi.org/10.1016/S1352-2310(98)00228-3, 1999.

Hayhoe, K., Kheshgi, H. S., Jain, A. K., and Wuebbles, D. J.: Substitution of natural gas for coal: Climatic effects of utility sector emissions, Climate Change, 54, 107–139, https://doi.org/10.1023/A:1015737505552, 2002.

Hirst, B., Gibson, G., Gillespie, S., Archibald, I., Podlaha, O., Skeldon, K. D., Courtial, J., Monk, S., and Padgett, M.: Oil and gas prospecting by ultra-sensitive optical gas detection with inverse gas dispersion modelling, Geophys. Res. Lett., 31, 1–4, https://doi.org/10.1029/2004GL019678, 2004.

Jones, F. M., Phillips, F. A., Naylor, T., and Mercer, N. B.: Methane emissions from grazing Angus beef cows selected for divergent residual feed intake, Anim. Feed Sci. Tech., 166–167, 302–307, https://doi.org/10.1016/j.anifeedsci.2011.04.020, 2011.

Karion, A., Sweeney, C., Pétron, G., Frost, G., Michael Hardesty, R., Kofler, J., Miller, B. R., Newberger, T., Wolter, S., Banta, R., Brewer, A., Dlugokencky, E., Lang, P., Montzka, S. A., Schnell, R., Tans, P., Trainer, M., Zamora, R., and Conley, S.: Methane emissions estimate from airborne measurements over a western United States natural gas field, Geophys. Res. Lett., 40, 4393–4397, https://doi.org/10.1002/grl.50811, 2013.

Künsch, H. R.: The jackknife and the bootstrap for general stationary observations, Ann. Stat., 17, 1217–1241, 1989.

Lawson, C. L. and Hanson, R. J.: Solving Least Squares Problems, Prentice-Hall, Jet Propulsion Laboratory, 1995.

Leuning, R., Etheridge, D., Luhar, A., and Dunse, B.: Atmospheric monitoring and verification technologies for CO2 geosequestration, Int. J. Greenh. Gas Con., 2, 401–414, https://doi.org/10.1016/j.ijggc.2008.01.002, 2008.

Levine, Z. H., Pintar, A. L., Dobler, J. T., Blume, N., Braun, M., Zaccheo, T. S., and Pernini, T. G.: The detection of carbon dioxide leaks using quasi-tomographic laser absorption spectroscopy measurements in variable wind, Atmos. Meas. Tech., 9, 1627–1636, https://doi.org/10.5194/amt-9-1627-2016, 2016.

McBain, M. C. and Desjardins, R. L.: The evaluation of a backward Lagrangian stochastic (bLS) model to estimate greenhouse gas emissions from agricultural sources using a synthetic tracer source, Agr. Forest Meteorol., 135, 61–72, https://doi.org/10.1016/j.agrformet.2005.10.003, 2005.

Mitchell, A. L., Tkacik, D. S., Roscioli, J. R., Herndon, S. C., Yacovitch, T. I., Martinez, D. M., Vaughn, T. L., Williams, L., Sullivan, M., Floerchinger, C., Omara, M., Subramanian, R., Zimmerle, D., Marchese, A. J., and Robinson, A. L.: Measurements of Methane Emissions from Natural Gas Gathering Facilities and Processing Plants: Measurement Results, Environ. Sci. Technol., 49, 12602, https://doi.org/10.1021/acs.est.5b04018, 2015.

Myhre, G., Shindell, D., Breìon, F.-M., Collins, W., Fuglestvedt, J., Huang, J., Koch, D., Lamarque, J.-F., Lee, D., Mendoza, B., Nakajima, T., Robock, A., Stephens, G., Takemura, T., and Zhang, H.: Anthropogenic and Natural Radiative Forcing, in Climate Change 2013: The Physical Science Basis, Contribution of Working Group I to the Fifth Assessment Report of the Intergovernmental Panel on Climate Change, edited by: Stocker, T. F., Qin, D., Plattner, G.-K., Tignor, M., Allen, S. K., Boschung, J., Nauels, A., Xia, Y., Bex, V., and Midgley, P. M., Cambridge University Press, Cambridge, United Kingdom and New York, NY, USA, 2013.

Nikodem, M., Plant, G., Sonnenfroh, D., and Wysocki, G.: Open-path sensor for atmospheric methane based on chirped laser dispersion spectroscopy, Appl. Phys. B., 119, 3–9, https://doi.org/10.1007/s00340-014-5938-3, 2015.

Perry, S., Cimorelli, A., Lee, R., Paine, R., Venkatram, A., Weil, J., and Wilson, R.: AERMOD: a dispersion model for industrial source applications, Washington, D.C., 1994.

Ravikumar, A. P., Wang, J., and Brandt, A. R.: Are Optical Gas Imaging Technologies Effective For Methane Leak Detection?, Environ. Sci. Technol., 51, 718–724, https://doi.org/10.1021/acs.est.6b03906, 2016.

Rella, C. W., Tsai, T. R., Botkin, C. G., Crosson, E. R., and Steele, D.: Measuring emissions from oil and natural gas well pads using the mobile flux plane technique, Environ. Sci. Technol., 49, 4742–4748, https://doi.org/10.1021/acs.est.5b00099, 2015.

Rieker, G. B., Giorgetta, F. R., Swann, W. C., Kofler, J., Zolot, A. M., Sinclair, L. C., Baumann, E., Cromer, C., Petron, G., Sweeney, C., Tans, P. P., Coddington, I., and Newbury, N. R.: Frequency-comb-based remote sensing of greenhouse gases over kilometer air paths, Optica, 1, 290–298, https://doi.org/10.1364/OPTICA.1.000290, 2014.

Scire, J. S., Strimaitis, D. G., and Yamartino, R. J.: A User's Guide for the CALPUFF Dispersion Model, Concord, MA, 2000.

Subramanian, R., Williams, L. L., Vaughn, T. L., Zimmerle, D., Roscioli, J. R., Herndon, S. C., Yacovitch, T. I., Floerchinger, C., Tkacik, D. S., Mitchell, A. L., Sullivan, M. R., Dallmann, T. R., and Robinson, A. L.: Methane emissions from natural gas compressor stations in the transmission and storage sector: Measurements and comparisons with the EPA greenhouse gas reporting program protocol, Environ. Sci. Technol., 49, 3252–3261, https://doi.org/10.1021/es5060258, 2015.

Truong, G.-W., Waxman, E. M., Cossel, K. C. C., Baumann, E., Klose, A., Giorgetta, F. R., Swann, W. C., Newbury, N. R., and Coddington, I. C.: Accurate frequency referencing for fieldable dual-comb spectroscopy, Opt. Express, 24, 30495–30504, https://doi.org/10.1364/OE.24.030495, 2016.

U.S. Energy Information Administration: Annual Energy Outlook 2015, available at: www.eia.gov/forecasts/aeo (last access: 1 September 2016), 2015.

Wagner, G. A. and Plusquellic, D. F.: Ground-based, integrated path differential absorption LIDAR measurement of CO2, CH4, and H2O near 1.6 μm, Appl. Opt., 55, 6292–6310, https://doi.org/10.1364/AO.55.006292 1., 2016.

Waxman, E. M., Cossel, K. C., Truong, G.-W., Giorgetta, F. R., Swann, W. C., Coburn, S., Wright, R. J., Rieker, G. B., Coddington, I., and Newbury, N. R.: Intercomparison of open-path trace gas measurements with two dual-frequency-comb spectrometers, Atmos. Meas. Tech., 10, 3295–3311, https://doi.org/10.5194/amt-10-3295-2017, 2017.

Weil, J. C., Sullivan, P. P., Patton, E. G., and Moeng, C. H.: Statistical Variability of Dispersion in the Convective Boundary Layer: Ensembles of Simulations and Observations, Bound.-Lay. Meteorol., 145, 185–210, https://doi.org/10.1007/s10546-012-9704-y, 2012.

Wilson, J. D. and Sawford, B. L.: Review of Lagrangian stochastic models for trajectories in the turbulent atmosphere, Bound.-Lay.

Meteorol., 78, 191–210, https://doi.org/10.1007/BF00122492, 1996.

Wu, C. F., Wu, T. gang, Hashmonay, R. A., Chang, S. Y., Wu, Y. S., Chao, C. P., Hsu, C. P., Chase, M. J., and Kagann, R. H.: Measurement of fugitive volatile organic compound emissions from a petrochemical tank farm using open-path Fourier transform infrared spectrometry, Atmos. Environ., 82, 335–342, https://doi.org/10.1016/j.atmosenv.2013.10.036, 2014.

Zavala-Araiza, D., Lyon, D. R., Alvarez, R. A., Davis, K. J., Harriss, R., Herndon, S. C., Karion, A., Kort, E. A., Lamb, B. K., Lan, X., Marchese, A. J., Pacala, S. W., Robinson, A. L., Shepson, P. B., Sweeney, C., Talbot, R., Townsend-Small, A., Yacovitch, T. I., Zimmerle, D. J., and Hamburg, S. P.: Reconciling divergent estimates of oil and gas methane emissions, P. Natl. Acad. Sci. USA, 112, 15597–15602, https://doi.org/10.1073/pnas.1522126112, 2015a.

Zavala-Araiza, D., Lyon, D., Alvarez, R. A., Palacios, V., Harriss, R., Lan, X., Talbot, R., and Hamburg, S. P.: Toward a Functional Definition of Methane Super-Emitters: Application to Natural Gas Production Sites, Environ. Sci. Technol., 49, 8167–8174, https://doi.org/10.1021/acs.est.5b00133, 2015b.

Research Article Vol. 1, No. 5 / November 2014 / Optica 290

Frequency-comb-based remote sensing of greenhouse gases over kilometer air paths

G. B. Rieker,[1,2,*] F. R. Giorgetta,[1] W. C. Swann,[1] J. Kofler,[3] A. M. Zolot,[1] L. C. Sinclair,[1] E. Baumann,[1] C. Cromer,[1] G. Petron,[3] C. Sweeney,[3] P. P. Tans,[3] I. Coddington,[1] and N. R. Newbury[1,4]

[1]National Institute of Standards and Technology, Boulder, Colorado 80305, USA

[2]University of Colorado-Boulder, Boulder, Colorado 80309, USA

[3]National Oceanic and Atmospheric Administration, Boulder, Colorado 80305, USA

[4]e-mail: nathan.newbury@nist.gov

*Corresponding author: greg.rieker@colorado.edu

Received 18 July 2014; revised 30 August 2014; accepted 21 September 2014 (Doc. ID 217215); published 29 October 2014

Increasing our understanding of regional greenhouse gas transport, sources, and sinks requires accurate, precise, continuous measurements of small gas enhancements over long ranges. We demonstrate a coherent dual frequency-comb spectroscopy technique capable of achieving these goals. Spectra are acquired spanning 5990 to 6260 cm^{-1} (1600–1670 nm) covering ~700 absorption features from CO_2, CH_4, H_2O, HDO, and $^{13}CO_2$, across a 2 km path. The spectra have sub-1-kHz frequency accuracy, no instrument lineshape, and a 0.0033 cm^{-1} point spacing. They are fit with different absorption models to yield dry-air mole fractions of greenhouse gases. These results are compared with a point sensor under well-mixed conditions to evaluate the accuracy of models critical to global satellite-based trace gas monitoring. Under heterogeneous conditions, time-resolved data demonstrate tracking of small variations in mole fractions, with a precision <1 ppm for CO_2 and <3 ppb for CH_4 in 5 min. Portable systems could enable regional monitoring.

OCIS codes: (300.6300) Spectroscopy, Fourier transforms; (280.1120) Air pollution monitoring; (010.0280) Remote sensing and sensors.

http://dx.doi.org/10.1364/OPTICA.1.000290

1. INTRODUCTION

Absorption spectroscopy over open paths provides a means of remotely sensing changes in greenhouse gas mole fractions—a critical need for greenhouse gas transport, source, and sink studies as well as future regulatory monitoring [1–3]. It is implemented in satellite instruments, upward-looking Fourier transform spectrometers (FTS), and ground-based FTS and laser spectrometers [4–11]. Ideally, these systems should detect the dry-air mole fractions (which correct for variable dilution by water vapor) of multiple gases over long paths with high precision and reproducibility to enable mapping of small gradients in both space and time. However, absorption spectroscopy faces two distinct challenges. First, spectral databases required to convert absorption to concentrations cannot support the desired reproducibility between instruments of 0.1 ppm CO_2 and 2 ppb CH_4 for background greenhouse gas monitoring [12], and less than 1 ppm CO_2 for urban enhancement monitoring [13–15]. Second, there is a lack of portable, long-path, multigas sensors with high reproducibility to support regional monitoring. Portable FTS is limited to sub-kilometer paths and ~5%–10% uncertainty because of divergent sources and broad instrument lineshapes [10,16]. Therefore, regional studies use flushed-cell point sensors calibrated via a reference gas [17,18]. In contrast, accurate open-air path systems could provide continuous path-averaged mole fractions that avoid representation errors associated with point sensors [3,19].

Dual frequency-comb spectroscopy (DCS) is a promising solution to both challenges. DCS [20–31] has broadband spectral coverage for multispecies detection, a bright diffraction-limited source for high signal-to-noise ratio (SNR) over multikilometer ranges, a rapid update rate for immunity to turbulence-induced optical intensity fluctuations, and, importantly, can sample the transmission on a comb tooth-by-tooth basis for high-accuracy spectra. Here, we show that the full advantages of DCS can be applied to quantitative outdoor sensing of greenhouse gases. Our measured spectra span 80,000 comb teeth covering 5990 to 6260 cm^{-1} (1600 to 1670 nm) with absorbance noise below 5×10^{-4}. Data are acquired at the comb-tooth separation of 0.0033 cm^{-1} (100 MHz), with negligible instrument lineshape since the comb teeth are essentially delta functions in frequency. We demonstrate simultaneous retrieval of dry-air mole fractions of CO_2, CH_4, H_2O, HDO, and $^{13}CO_2$ and air temperature over a 2 km turbulent air path. During well-mixed atmospheric conditions, these data enable high-resolution evaluation of spectral absorption models and, when combined with laboratory measurements, should lead to improved spectral absorption models critical for open long-path remote sensing [13,32].

Moreover, the advent of portable frequency combs [33] should enable field-deployable DCS to support verification and monitoring of emissions of distributed sources (e.g., carbon sequestration [11] and gas development sites [2,34]) and larger-scale monitoring networks. As an initial demonstration, time-resolved dry-air mole fractions were acquired continuously over three days. The DCS data compare well with a nearby point sensor for large-scale fluctuations with much lower sensitivity to local concentration spikes. One-sigma stabilities of <1 ppm (μ mol/mol) for CO_2 and <3 ppb (nmol/mol) for CH_4 are reached at 5 min averaging. Absolute agreement is limited by the current spectral databases to ~1%–2% and by variability in sampled regions. Future optimized systems with higher power and extended spectral coverage [29,35–40] could reach similar stabilities in seconds, over 10 km, while sensing additional species, isotopologues, and oxygen [28]. Finally, the absence of instrument lineshapes should enable direct cross comparison of retrievals between systems, times, and locations.

2. OPEN-AIR DUAL-COMB SPECTROMETER

Figure 1 shows the experimental setup. In dual-comb spectroscopy [20–30], two frequency combs are arranged to have offset repetition rates (f_r and $f_r + \Delta f_r$). When combined, the resulting heterodyne signal is an rf frequency comb, where each rf comb tooth is spaced by Δf_r, and has a one-to-one relationship with a specific pair of optical comb teeth [see Fig. 1(a)]. Therefore, this rf spectrum is simply scaled to reproduce the optical spectrum.

Here, we implement DCS with two mutually coherent erbium-doped fiber frequency combs ($f_r \sim 100$ MHz, $\Delta f_r = 444$ Hz) with relative ~1 Hz comb linewidth and with each comb tooth's frequency known to better than 1 kHz [23] (see Supplement 1). The comb spectra are centered within the atmospheric water-vapor window near 1.6 μm and further shaped to cover both a portion of the CH_4 tetradecad and a CO_2 combination band. The choice of $\Delta f_r = 444$ Hz allows an alias-free optical bandwidth of $f_r^2/(2\Delta f_r) = 375$ cm^{-1}, which covers both absorption bands simultaneously [22]. The comb outputs are combined and transmitted over a 2 km folded open-air path on the NIST Boulder campus [see Figs. 1(b) and 1(c)]. This 2 km path length exceeds previous laboratory-based DCS using either multipass cells or resonant cavities.

Figures 1(d) and 1(e) show the resulting high SNR transmission spectrum acquired over ~170 min under relatively constant temperature and pressure across the measurement path (see Supplement 1). The overall shape corresponds to the spectrally filtered comb light. The stronger CO_2, H_2O, and CH_4 absorption lines appear as sharp dips of up to 15% with many weaker CH_4, CO_2, and H_2O, HDO, and $^{13}CO_2$ lines observed down to 10^{-3} absorbance. There are ~80,000 comb-tooth pairs across the 267 cm^{-1} window. With the spectral shaping, about half of these, or ~40,000 comb-tooth pairs, compose the measured spectrum. Each comb-tooth pair contributes a distinct data point in the transmitted spectrum with kilohertz-level frequency uncertainty (corresponding to a resolving power of 10^{11}), spaced at $f_r = 100$ MHz (0.0033 cm^{-1}), and with SNR in the signal intensity exceeding 3000:1 for these long time-averaged data. Even higher SNR values would be possible except that we aggressively limited the transmitted power to avoid any lineshape distortions due to detector nonlinearity [23,29]. These data were acquired with coherent summing (see Supplement 1), but continuous time data confirmed ~Hz linewidth between the detected pairs of frequency-comb teeth. The quality of these data is consistent with previous ultrahigh-resolution laboratory DCS spectra and demonstrates that the fundamental properties of coherent DCS—namely high resolution, high accuracy, broad bandwidth, and high SNR—can be directly translated to field-based measurements.

Turbulence is a concern for high-resolution open-air path spectroscopy as it can easily cause strong (100%) and fast (>100 Hz) optical intensity modulation, potentially leading to excess noise in the measured optical transmission spectrum. The power spectral density related to turbulence-induced intensity noise falls off strongly as $f^{-8/3}$ beyond the characteristic cutoff Fourier frequency, $f_c \approx U/\sqrt{2\pi L\lambda}$, where U is the wind speed, λ is the optical wavelength, and L is the path length [41]. Here, f_c is tens of hertz. In comparison, the DCS effectively acquires a single spectrum within $1/\Delta f_r = 1/444$ s. In other words, since $f_c < \Delta f_r$, the turbulence intensity noise is effectively frozen during a single spectrum. Rain, light fog, or clipping of the beam at the telescope will reduce the SNR if there is significant attenuation, but should not distort the spectrum for similar reasons. Of course, some turbulence-induced fluctuations do occur on the timescale of a single interferogram, but a more rigorous discussion (see Fig. 1 of Supplement 1) shows they appear as multiplicative noise that is below the overall noise floor. Turbulence can also cause optical

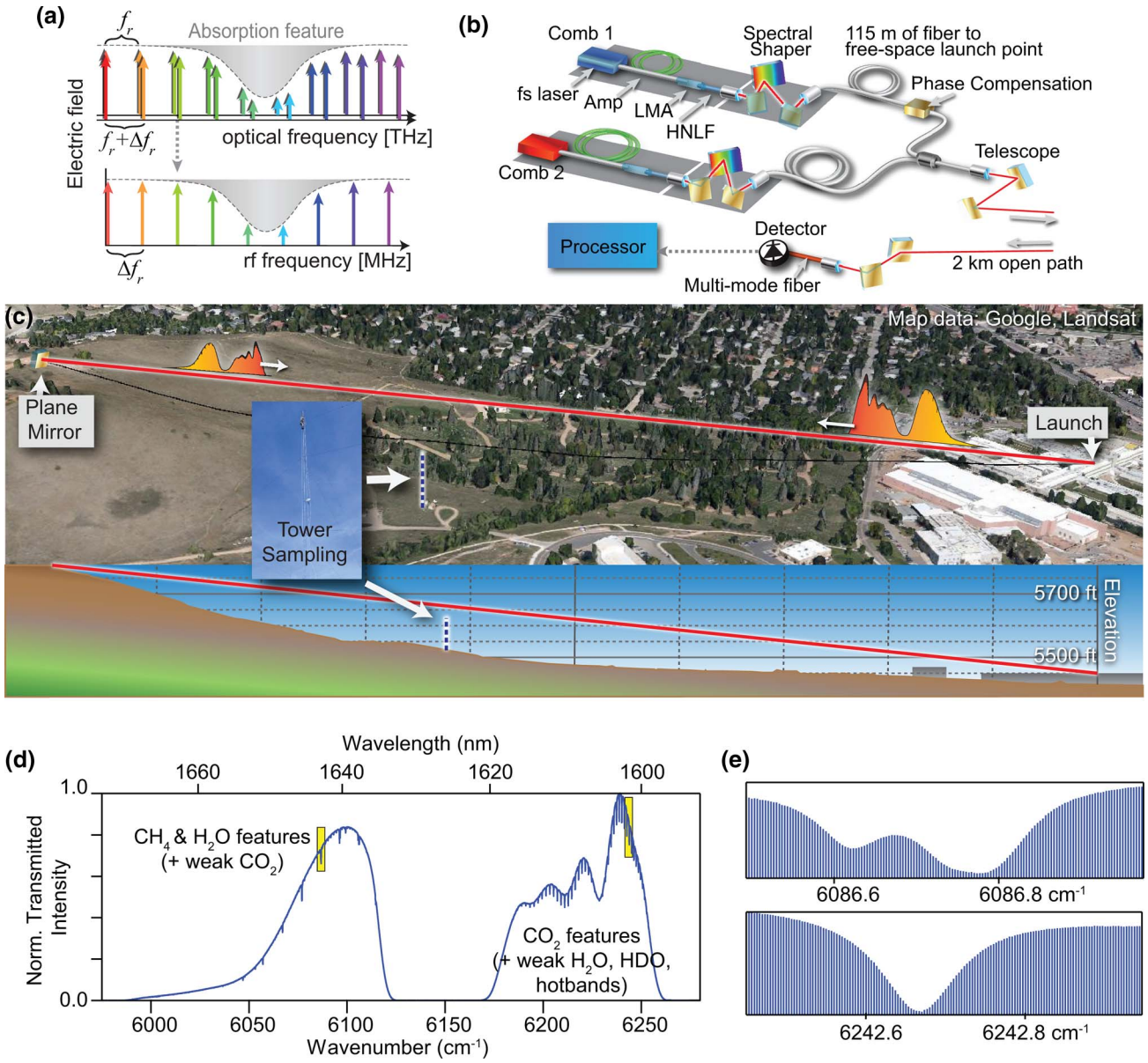

Fig. 1. Open-air path greenhouse gas sensing through dual-comb spectroscopy. (a) DCS concept: two combs with slightly different tooth spacing interfere on a detector, giving a third rf comb with a one-to-one mapping to the optical comb teeth. (The actual experiment spans ~10^5 comb teeth.) (b) Experimental setup: two combs are amplified, pulse-compressed in large mode area (LMA) fiber, spectrally broadened in highly nonlinear fiber (HNLF), and filtered to generate light covering the spectral bands of interest. Two fibers carry the comb light to the rooftop, where the light is combined and launched in a ~40 mm beam ($1/e^2$ diameter), and reflected from a 50 cm diameter plane mirror located 1 km distant. The return light is coupled to a multimode fiber and detected. The transmitted light power was limited to 1.5 mW so that the maximum received power was always below a conservative detector nonlinearity threshold of 50 μW average power (500 fJ pulse energy). (c) Location of the 2 km interrogation path (red line, ground projection represented by black line), the tower with the point sensor intake (inset), and elevation of the beam path (bottom inset). (d) Example transmitted intensity showing the smoothly varying comb intensity and abrupt dips due to absorption. (e) Expanded view of absorption features. The typical gas absorption lines have ~40 teeth across each ~4 GHz wide line (top, several transitions from the $2\nu 3$ level of the CH_4 tetradecad; bottom, R20 transition of the 30013←00001 band of CO_2).

wavefront distortions and phase noise on the comb lines [41,42]. However, since both combs are copropagating, these effects are common mode and ultimately negligible. This relative immunity of DCS to turbulence is in strong contrast to high-resolution FTS or conventional swept laser spectroscopy, which have longer acquisition periods. Finally, as a coherent system, DCS is unaffected by collected sunlight because of the narrow heterodyne detection bandwidth.

3. MEASUREMENTS UNDER WELL-MIXED ATMOSPHERIC CONDITIONS

The DCS spectra provide a direct means to validate current and future spectral databases and absorption models since the spectra are free from instrument distortions and the DCS horizontal path avoids the atmospheric modeling that is required with up-looking total column measurements [7,14]. The transmission spectrum shown in Fig. 1(d) is

converted to absorbance by normalizing out the overall comb spectrum and applying Beer's law. Initially, we acquired a reference spectrum without the air path, but this approach introduced additional baseline etalons. Therefore, we instead normalized out the smoothly varying comb spectrum through piecewise baseline fitting (see Supplement 1), as is done for FTIR spectra. The resulting absorbance spectrum, shown in Fig. 2, can then be fit using different absorption models to both assess those models and find the path-averaged dry-air mole fractions of various greenhouse gas species.

We separately fit the lower (6050 to 6120 cm^{-1}) and upper (6180 to 6260 cm^{-1}) spectral windows. Within a spectral window, we fit the entire absorption spectrum at once. The only inputs to the fits are the measured atmospheric pressure (from calibrated pressure gauges at each end of the path) and the absorption models. The fitted parameters are the overall gas

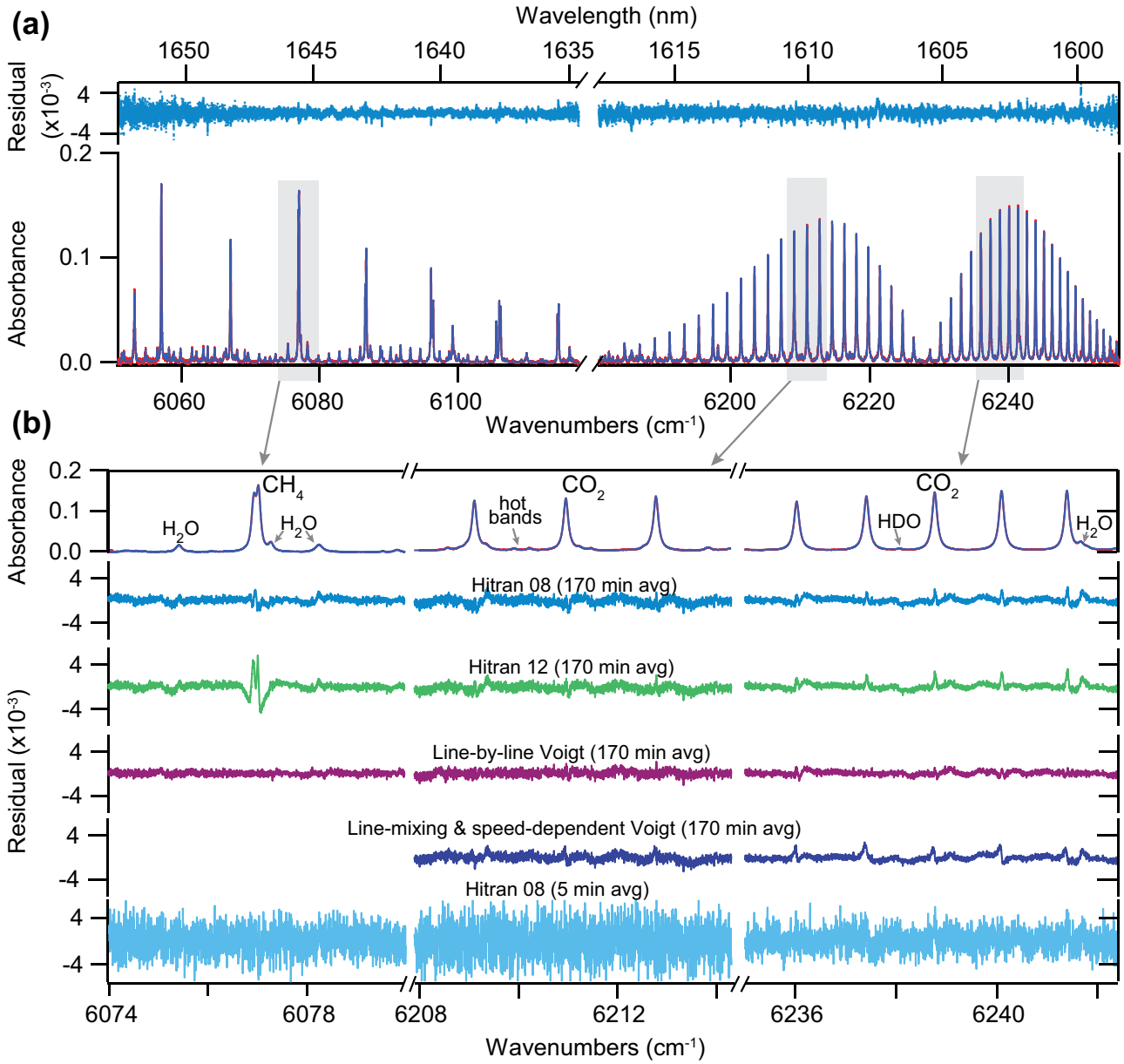

Fig. 2. Baseline-corrected absorbance from the transmission spectrum of Fig. 1(d). (a) The left spectrum mainly comprises CH_4 and H_2O lines, with some weaker CO_2 lines, while the right spectrum shows the 30013 ← 00001 CO_2 band, CO_2 hot bands, and H_2O, $^{13}CO_2$, and HDO features. The data (red line), fit with HITRAN 2008 (blue line, indistinguishable from the data), and residuals (upper blue line) are shown. There are ~40, 000 data points, or comb teeth, spaced at 100 MHz across the spectral windows. (b) Expanded view of a few representative lines along with residuals for fits to the HITRAN 2008 model [44], the HITRAN 2012 model [43], the line-mixing and speed-dependent model of Ref. [14], and line-by-line Voigt fits to each line. Also shown are the fit residuals for a 5 min time average, identical to those used in the time-resolved data of Fig. 3. The noise per comb tooth (in absorbance units) for the 5 min averaged spectra is 2.0×10^{-3}, 2.7×10^{-3}, and 1.7×10^{-3} for the three windows shown, with the differences attributable to different spectral intensities. For the 170 min average, the noise decreases with the square root of time, as expected, to 3.5×10^{-4}, 5.1×10^{-4}, and 3.0×10^{-4}, respectively. However, there are clear residuals near the spectral lines due to mismatch between the measured lineshapes and absorption models.

Table 1. Mole Fractions Retrieved from Fits of the Absorbance Spectrum of Fig. 2 with Four Absorption Models: HITRAN 2008 [44], HITRAN 2012 [43], Line-Mixing Speed-dependent Voigt (LM/SD) [14], and Toth *et al.* [48][a]

	Mole Fraction Retrieval (ppm)				Systematic Unc. (ppm)	
	Hitran 08	Hitran 12	LM/SD	Toth	Excluding Spectral Model	
CO_2	408.7	407.7	404.7	406.2	0.8	0.21%
CH_4	1.878	1.985	—	—	0.009	0.45%
H_2O	3223	3217	—	—	22	0.73%
HDO	1.13	0.97	—	—	0.13	11%
$^{13}CO_2$	4.5	4.4	—	4.2	1.7	37%

[a]The final column reports the systematic (type B) uncertainty of the dual-comb spectrometer, excluding the model dependence captured in the first columns (see text).

concentrations of CO_2, $^{13}CO_2$, H_2O, CH_4, and HDO, and temperature. The fit to the upper spectral window includes a fit for temperature based on the band-wide CO_2 absorption; in this way the path-averaged temperature is extracted directly instead of using colocated temperature sensors that can suffer from solar loading. The CO_2 and $^{13}CO_2$ mole fractions were extracted from the fit to the upper spectral region, while the CH_4, H_2O, and HDO mole fractions were extracted from the fit to the lower spectral region (although there are CO_2 lines present as well). More than 300 spectral lines are included in the lower spectral window and 400 in the upper spectral window.

Absorption models for species in this region are evolving. The models consist of a set of spectral parameters that describe the temperature-, pressure-, and concentration-dependent strength, location, and width of each absorption feature, along with a lineshape profile model. Figure 2 shows the results of fits using the High-Resolution Transmission Molecular Absorption Database (HITRAN) 2012 [43] and 2008 [44]. The standard deviation of the residuals is $\sim 2 \times 10^{-3}$ absorbance units for 5 min averages at the 100 MHz (0.0033 cm^{-1}) point spacing, dropping to $< 5 \times 10^{-4}$ at 170 min. When scaled to the same resolution, this SNR is comparable to high-resolution solar, up-looking FTS spectra (but in a more compact, potentially portable instrument package without long, moving interferometer arms). For the upper spectral region, fits using the similar HITRAN 2012 [43] and 2008 [44] databases result in peak residuals below 3×10^{-3}, except for one errant line near 187.38 THz (coincident with a reported weak HDO line in HITRAN 2008). For the lower spectral region, HITRAN 2012 has methane parameters quite different from HITRAN 2008, and this difference is strongly reflected in the residuals, as well as the concentrations as discussed in Table 1.

The Voigt profile used with the HITRAN databases [43,44] neglects, among other things, coupling between energy states of nearby transitions (line mixing) and the effect of collisions on the Doppler contribution to the lineshape (speed dependence). Therefore, concentrations extracted using the Voigt profiles have been shown to lead to inaccurate atmospheric retrievals [45]. Figure 2(b) also shows residuals to a fit using a lineshape model and a corresponding spectral parameter database that includes line-mixing and speed-dependent Voigt profiles and was developed to support accurate satellite-based trace gas monitoring [14,46,47]. Residuals remain, with quite different structures compared to the other models; however, the fitted concentration using the line-mixing and speed-dependent model should have the highest accuracy.

Figure 2(b) also contains residuals resulting from a line-by-line Voigt profile fit where the collisional linewidth, line center, and line strength are finally allowed to vary on a line-by-line basis. Though this fit overlooks the quantum-mechanical basis of the previous spectral databases, the small residual may indicate that the largest sources of error in absorption models are the spectral parameters (line strength, line center, broadening coefficients, etc.) rather than deviations from the Voigt lineshape model.

Table 1 compares the mole fractions extracted using the different absorption models. There is a significant model-dependent spread. For CO_2, all four absorption models rely on analysis of the same underlying laboratory FTS data, so this spread emphasizes the consequences of different lineshape models. As mentioned above, among the models considered here the line-mixing, speed-dependent Voigt profile (LM/SD) and corresponding spectral parameter database [14,46,47] is expected to yield the most accurate results for CO_2. Table 1 also reports the DCS systematic uncertainty excluding the model-dependent effects. The uncertainty is based on the root-mean-square of the sensitivities of the retrieved mole fractions to several different factors: maximum pressure and temperature path inhomogeneities (±500 Pa and 6 K, respectively), uncertainty in path length (±20 cm) and air pressure (±30 Pa), and baseline correction. Baseline correction is the largest contributor (by a factor of 10 or more) in particular due to an etalon ripple with absorbance amplitude 10^{-3} (see Supplement 1). For CO_2, the other factors contribute below 0.06 ppm uncertainty.

Table 2. Comparison of the Mole Fractions Obtained with the Dual-Comb Spectrometer and the Tower-Mounted Point Sensor under the Well-Mixed, Stable Atmospheric Conditions of Fig. 2[a]

Mole Fraction (ppm)	DCS	Tower Sensor	Difference	
CO_2	404.7 ± 0.8	397.6 ± 0.06	7.1	1.78%
CH_4	1.878 ± 0.009	1.874 ± 0.002	0.004	0.20%
H_2O	3223 ± 22	3168 ± 95	55	1.74%

[a]For the DCS, the dry-air mole fraction of CO_2 is retrieved from the LM/SD fit, and the dry-air CH_4 and H_2O ratios are retrieved from the HITRAN 2008 fit.

Table 2 compares the DCS to the tower-mounted point sensor. For CO_2, there is 1.8% offset with the LM/SD fits, which increases to 2.8% for the HITRAN 2008 fits. Under the windy, well-mixed atmospheric conditions for these data, the DCS and tower-mounted point sensor should measure almost identical mole fractions. Given that the point sensor is calibrated directly against the World Meteorological Organization (WMO) reference gas (see Supplement 1), we attribute most of the offset to the DCS retrieval and specifically to the line strengths of the absorption model. For CH_4, the DCS analyzed with the HITRAN 2008 database is in excellent agreement with the tower sensor (although the fits to HITRAN 2012 exhibit a 5.7% offset from the tower sensor). For H_2O, the two systems agree to within the uncertainty of the tower sensor.

The main conclusion—that better absorption models are needed to support accurate greenhouse gas monitoring—very much echoes the significant body of work in support of satellite measurements. Subpercent uncertainties in retrieved gas concentrations will require improvements in the spectral database, possibly through laboratory frequency-comb or cavity ring-down systems [23,29,49,50]. Finally, while DCS does rely on accurate spectral databases (as with any open-air path absorption technique), it should be straightforward to reanalyze DCS spectra as the databases are refined. In fact, this feature of the dual-comb spectra is important for accurate greenhouse gas monitoring. Whereas extractive flushed-cell sampling instruments rely on reference gas calibrations that must be performed periodically to maintain accuracy and cross-instrument comparability, the measured dual-comb

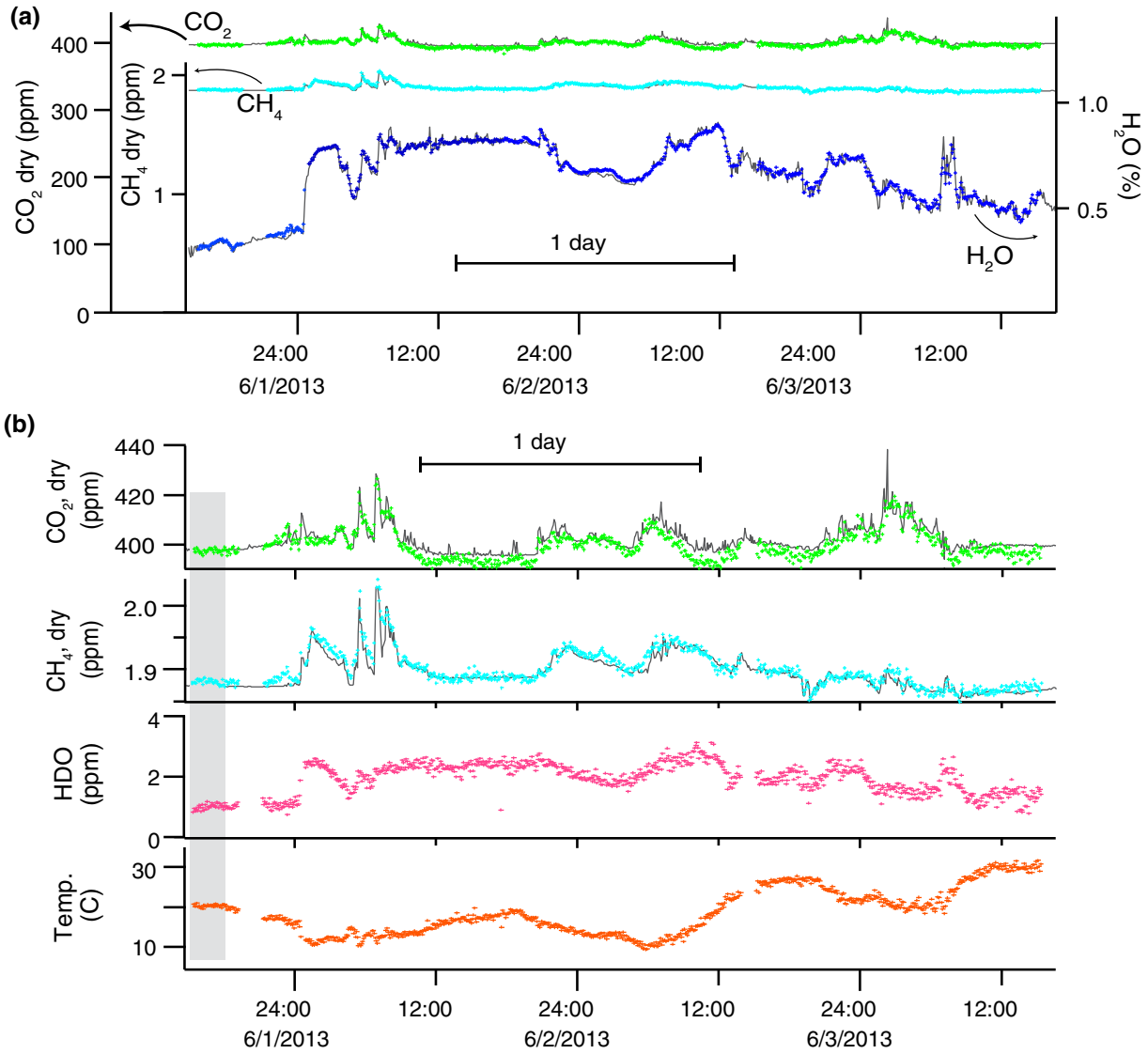

Fig. 3. Time-resolved mole fractions. (a) Time dependence of the dry-air mole fraction for CO_2 (green), CH_4 (light blue), and water (dark blue) retrieved from the DCS and the corresponding values from the tower-mounted point sensor (black line) at 5 min periods over three days. (b) Time dependence of CO_2 and CH_4 with an expanded y axis. Also shown are the time dependence of HDO (pink) and the retrieved path-averaged temperature (orange). All data are from the fit with the absorption model based on HITRAN 2008. The DCS CO_2 mole fraction has been scaled to remove the 2.8% offset between the DCS and the tower-mounted sensor over the initial ~3 h period (shaded region) where the atmosphere was well-mixed and the measurement path was upwind from the NIST central utility plant.

spectra from multiple instruments can be compared directly and indefinitely. Therefore, the retrieved mole fractions can be similarly compared when the spectra are fit with an accurate, bias-free absorption model. For example, as water-broadening coefficients for CO_2 and CH_4 become available, these effects can be included without the empirical corrections needed with flushed-cell point sensors [18].

4. TIME-RESOLVED MEASUREMENTS OF THE DRY-AIR MOLE FRACTIONS OVER A THREE-DAY PERIOD

The data of Fig. 2 were acquired over a windy, well-mixed period in which the mole fractions were quite stable. Normally, the mole fractions will vary significantly from nearby sources and sinks, and as the planetary boundary-layer height changes. We can analyze these time variations using the same fitting procedures described above. Figure 3 shows the results over a three-day period at 5 min averaging, analyzed with the HITRAN 2008 spectral database. The path-averaged air temperature is extracted directly from the fit to the

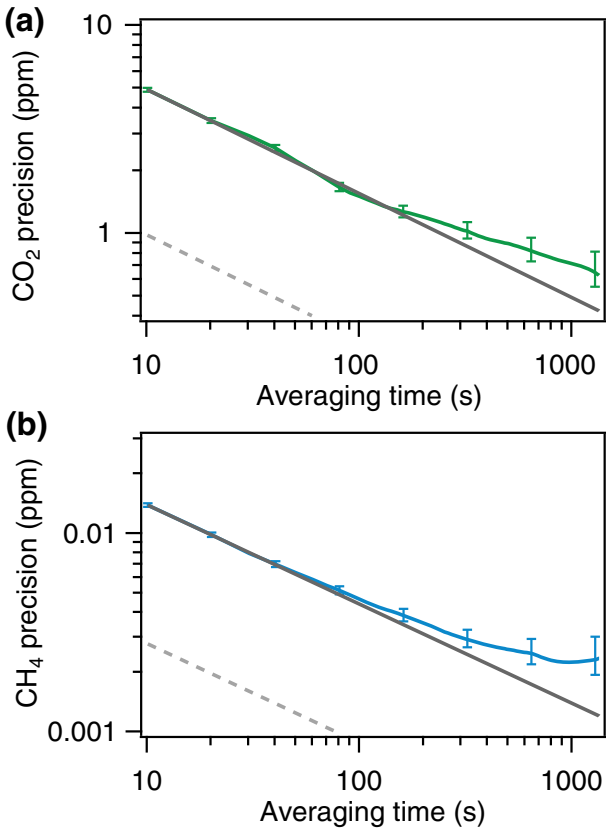

Fig. 4. Precision (Allan deviation) from data acquired during high-wind periods with a stable, well-mixed atmosphere. (a) CO_2 precision (green) versus averaging time, τ, which follows $15\sqrt{\tau}$/ppm, where τ is in seconds (gray line), or 0.86 ppm at 5 min. At longer times, actual atmospheric mole fraction variations cause a decrease in the slope. A modest increase of the launched power up to the eye-safe limit of 9.6 mW (or alternatively an increased receive aperture) would yield the improved precision of $3\sqrt{\tau}$/ppm (dashed gray line). (b) CH_4 precision (blue) follows a scaling of $40\sqrt{\tau}$/ppb (gray line) or 2.3 ppb at 5 min. Again, modest power increases, or increased receive aperture, would yield the improved precision of $8\sqrt{\tau}$/ppb (dashed gray line).

30013←00001 CO_2 spectral band, placing even greater reliance on accurate spectral parameters.

During periods of wind and daytime thermal turbulence, the dry-air mole fractions reported by both the DCS and the tower-mounted point sensor are relatively flat. During low wind and nighttime boundary-layer settling, both show strong variations in time. However, as expected, the point sensor is much more susceptible to short spikes from local plumes. (For comparison purposes, the tower-sensor data are averaged to 5 min here; at shorter timescales the spikes are even more pronounced.) Moreover, statistically significant offsets are common between the point sensor and the path-averaged DCS results, which is not surprising given the presence of localized emissions from vehicles, the NIST central utility plant (just south of the air path), and a nearby roadway. The comparison emphasizes the quantitative differences that can arise between a single point sensor and a path-averaged system. One expects the path-averaged system to connect more directly to kilometer-scale regional transport models. Moreover, with the addition of multiple reflectors the same DCS system could interrogate multiple displaced paths [11], providing even greater utility to regional models.

The overall sensitivity, or precision, of the DCS is calculated directly as the Allan deviation over a period of relative stability, as shown in Fig. 4. The optimal averaging time period depends on the timescale of the atmospheric fluctuations; we selected 5 min for Fig. 3, which also leads to a precision comparable to the systematic uncertainty (Table 2). However, operation over longer distances, at the full eye-safe power level of 9.6 mW, or at longer wavelengths where the absorption is tenfold stronger, will all dramatically improve the precision. In addition, stronger absorption lines will reduce the systematic uncertainty that is dominated by baseline ripple (etalons).

5. CONCLUSION

We demonstrate that DCS is ideally suited to the challenges associated with accurate sensing of atmospheric trace gases across open-air paths; it combines broadband spectral coverage for accurate multispecies detection with a diffraction-limited laser output for high sensitivity over multikilometer air paths. Equally important, its high acquisition speed achieves immunity to turbulence-induced intensity noise, and its negligible instrument lineshape enables high accuracy and ultimately accurate cross comparison of spectra (and therefore concentrations) acquired with different systems, at different times and locations. We demonstrate these capabilities over a 2 km open-air path with an initial system that measures CO_2, $^{13}CO_2$, CH_4, H_2O, HDO, and air temperature. Future broader bandwidth systems will detect more species, while higher power output will further improve the sensitivity. DCS data can support the development of accurate absorption models used in global, satellite-based greenhouse gas monitoring. Moreover, with the recent advancement of portable, high-performance frequency combs [33], there is no technological barrier to regional deployment of fielded DCS systems that have costs comparable to high-performance point sensors and are capable

of autonomous, eye-safe, around-the-clock monitoring of multiple gas species over multiple optical paths.

FUNDING INFORMATION

National Institute of Standards and Technology (NIST) (Greenhouse Gas and Climate Science Measurements); National Research Council (Research associateship award).

ACKNOWLEDGMENTS

We thank James Whetstone, Joe Hodges, and Scott Diddams for helpful discussions, Anna Karion for calibration of the point sensor, Terry Bullett for use of the radio tower, and Masaaki Hirano and Jeff Nicholson for donation of specialty optical fiber.

See Supplement 1 for supporting information.

REFERENCES

1. C. Le Quere, M. R. Raupach, J. G. Canadell, G. Marland, L. Bopp, P. Ciais, T. J. Conway, S. C. Doney, R. A. Feely, P. Foster, P. Friedlingstein, K. Gurney, R. A. Houghton, J. I. House, C. Huntingford, P. E. Levy, M. R. Lomas, J. Majkut, N. Metzl, J. P. Ometto, G. P. Peters, I. C. Prentice, J. T. Randerson, S. W. Running, J. L. Sarmiento, U. Schuster, S. Sitch, T. Takahashi, N. Viovy, G. R. van der Werf, and F. I. Woodward, "Trends in the sources and sinks of carbon dioxide," Nat. Geosci. **2**, 831–836 (2009).
2. D. R. Caulton, P. B. Shepson, R. L. Santoro, J. P. Sparks, R. W. Howarth, A. R. Ingraffea, M. O. L. Cambaliza, C. Sweeney, A. Karion, K. J. Davis, B. H. Stirm, S. A. Montzka, and B. R. Miller, "Toward a better understanding and quantification of methane emissions from shale gas development," Proc. Natl. Acad. Sci. USA **111**, 6237–6242 (2014).
3. M. R. Raupach, P. J. Rayner, D. J. Barrett, R. S. DeFries, M. Heimann, D. S. Ojima, S. Quegan, and C. C. Schmullius, "Model-data synthesis in terrestrial carbon observation: methods, data requirements and data uncertainty specifications," Glob. Chang. Biol. **11**, 378–397 (2005).
4. D. M. Hammerling, A. M. Michalak, C. O'Dell, and S. R. Kawa, "Global CO_2 distributions over land from the Greenhouse Gases Observing Satellite (GOSAT)," Geophys. Res. Lett. **39**, paper L08804 (2012).
5. J. O. Day, C. W. O'Dell, R. Pollock, C. J. Bruegge, D. Rider, D. Crisp, and C. E. Miller, "Preflight spectral calibration of the orbiting carbon observatory," IEEE Trans. Geosci. Remote Sens. **49**, 2793–2801 (2011).
6. C. Frankenberg, J. F. Meirink, M. van Weele, U. Platt, and T. Wagner, "Assessing methane emissions from global space-borne observations," Science **308**, 1010–1014 (2005).
7. D. Wunch, G. C. Toon, J.-F. L. Blavier, R. A. Washenfelder, J. Notholt, B. J. Connor, D. W. T. Griffith, V. Sherlock, and P. O. Wennberg, "The total carbon column observing network," Phil. Trans. R. Soc. B **369**, 2087–2112 (2011).
8. A. Ramanathan, J. Mao, G. R. Allan, H. Riris, C. J. Weaver, W. E. Hasselbrack, E. V. Browell, and J. B. Abshire, "Spectroscopic measurements of a CO_2 absorption line in an open vertical path using an airborne lidar," Appl. Phys. Lett. **103**, 214102 (2013).
9. D. K. MikelU. S. Environmental Protection Agency, Optical Remote Sensing for Measurement and Monitoring of Emissions Flux (n.d.), EPA Handbook, Office of Air Quality Planning and Standards, Air quality analysis division, Measurement technology group.
10. G. M. Russwurm and J. W. Childers, "Open-path Fourier transform infrared spectroscopy," in *Handbook of Vibrational Spectroscopy* (Wiley, 2006), pp. 1750–1773
11. S. D. Humphries, A. R. Nehrir, C. J. Keith, K. S. Repasky, L. M. Dobeck, J. L. Carlsten, and L. H. Spangler, "Testing carbon sequestration site monitor instruments using a controlled carbon dioxide release facility," Appl. Opt. **47**, 548–555 (2008).
12. W. Brand, ed., "15th WMO/IAEA Meeting on Carbon Dioxide, Other Greenhouse Gases, and Related Measurement Techniques," GAW Report No. 194 (World Meteorological Organization, 2009).
13. C. E. Miller, D. Crisp, P. L. DeCola, S. C. Olsen, J. T. Randerson, A. M. Michalak, A. Alkhaled, P. Rayner, D. J. Jacob, P. Suntharalingam, D. B. A. Jones, A. S. Denning, M. E. Nicholls, S. C. Doney, S. Pawson, H. Boesch, B. J. Connor, I. Y. Fung, D. O'Brien, R. J. Salawitch, S. P. Sander, B. Sen, P. Tans, G. C. Toon, P. O. Wennberg, S. C. Wofsy, Y. L. Yung, and R. M. Law, "Precision requirements for space-based X-CO_2 data," J. Geophys. Res.: Atmos. **112**, D10314 (2007).
14. D. R. Thompson, D. Chris Benner, L. R. Brown, D. Crisp, V. Malathy Devi, Y. Jiang, V. Natraj, F. Oyafuso, K. Sung, D. Wunch, R. Castaño, and C. E. Miller, "Atmospheric validation of high accuracy CO_2 absorption coefficients for the OCO-2 mission," J. Quant. Spectrosc. Radiat. Transfer **113**, 2265–2276 (2012).
15. K. L. Mays, P. B. Shepson, B. H. Stirm, A. Karion, C. Sweeney, and K. R. Gurney, "Aircraft-based measurements of the carbon footprint of Indianapolis," Environ. Sci. Technol. **43**, 7816–7823 (2009).
16. T. E. L. Smith, M. J. Wooster, M. Tattaris, and D. W. T. Griffith, "Absolute accuracy and sensitivity analysis of OP-FTIR retrievals of CO_2, CH_4 and CO over concentrations representative of "clean air" and "polluted plumes"," Atmos. Meas. Tech. **4**, 97–116 (2011).
17. W. Peters, A. R. Jacobson, C. Sweeney, A. E. Andrews, T. J. Conway, K. Masarie, J. B. Miller, L. M. P. Bruhwiler, G. Pétron, A. I. Hirsch, D. E. J. Worthy, G. R. van der Werf, J. T. Randerson, P. O. Wennberg, M. C. Krol, and P. P. Tans, "An atmospheric perspective on North American carbon dioxide exchange: CarbonTracker," Proc. Natl. Acad. Sci. USA **104**, 18925–18930 (2007).
18. C. W. Rella, H. Chen, A. E. Andrews, A. Filges, C. Gerbig, J. Hatakka, A. Karion, N. L. Miles, S. J. Richardson, M. Steinbacher, C. Sweeney, B. Wastine, and C. Zellweger, "High accuracy measurements of dry mole fractions of carbon dioxide and methane in humid air," Atmos. Meas. Tech. **6**, 837–860 (2013).
19. P. Ciais, P. Rayner, F. Chevallier, P. Bousquet, M. Logan, P. Peylin, and M. Ramonet, "Atmospheric inversions for estimating CO_2 fluxes: methods and perspectives," Climatic Change **103**, 69–92 (2010).
20. F. Keilmann, C. Gohle, and R. Holzwarth, "Time-domain mid-infrared frequency-comb spectrometer," Opt. Lett. **29**, 1542–1544 (2004).
21. A. Schliesser, M. Brehm, F. Keilmann, and D. van der Weide, "Frequency-comb infrared spectrometer for rapid, remote chemical sensing," Opt. Express **13**, 9029–9038 (2005).
22. I. Coddington, W. C. Swann, and N. R. Newbury, "Coherent dual-comb spectroscopy at high signal-to-noise ratio," Phys. Rev. A **82**, 043817 (2010).
23. A. M. Zolot, F. R. Giorgetta, E. Baumann, J. W. Nicholson, W. C. Swann, I. Coddington, and N. R. Newbury, "Direct-comb molecular spectroscopy with accurate, resolved comb teeth over 43 THz," Opt. Lett. **37**, 638–640 (2012).
24. T. Ideguchi, A. Poisson, G. Guelachvili, N. Picqué, and T. W. Hänsch, "Adaptive real-time dual-comb spectroscopy," Nat. Commun. **5**, 3375 (2014).
25. B. Bernhardt, A. Ozawa, P. Jacquet, M. Jacquey, Y. Kobayashi, T. Udem, R. Holzwarth, G. Guelachvili, T. W. Hänsch, and N. Picqué, "Cavity-enhanced dual-comb spectroscopy," Nat. Photonics **4**, 55–57 (2009).
26. J. Roy, J.-D. Deschênes, S. Potvin, and J. Genest, "Continuous real-time correction and averaging for frequency comb interferometry," Opt. Express **20**, 21932–21939 (2012).
27. S. Boudreau, S. Levasseur, C. Perilla, S. Roy, and J. Genest, "Chemical detection with hyperspectral lidar using dual frequency combs," Opt. Express **21**, 7411–7418 (2013).

28. S. Potvin and J. Genest, "Dual-comb spectroscopy using frequency-doubled combs around 775 nm," Opt. Express **21**, 30707–30715 (2013).
29. E. Baumann, F. R. Giorgetta, W. C. Swann, A. M. Zolot, I. Coddington, and N. R. Newbury, "Spectroscopy of the methane ν_3 band with an accurate midinfrared coherent dual-comb spectrometer," Phys. Rev. A **84**, 062513 (2011).
30. D. A. Long, A. J. Fleisher, K. O. Douglass, S. E. Maxwell, K. Bielska, J. T. Hodges, and D. F. Plusquellic, "Multiheterodyne spectroscopy with optical frequency combs generated from a continuous-wave laser," Opt. Lett. **39**, 2688–2690 (2014).
31. T. Ideguchi, S. Holzner, B. Bernhardt, G. Guelachvili, N. Picqué, and T. W. Hänsch, "Coherent Raman spectro-imaging with laser frequency combs," Nature **502**, 355–358 (2013).
32. S. Houweling, F.-M. Breon, I. Aben, C. Rödenbeck, M. Gloor, M. Heimann, and P. Ciais, "Inverse modeling of CO_2 sources and sinks using satellite data: a synthetic inter-comparison of measurement techniques and their performance as a function of space and time," Atmos. Chem. Phys. **4**, 523–538 (2004).
33. L. C. Sinclair, I. Coddington, W. C. Swann, G. B. Rieker, A. Hati, K. Iwakuni, and N. R. Newbury, "Operation of an optically coherent frequency comb outside the metrology lab," Opt. Express **22**, 6996–7006 (2014).
34. A. Karion, C. Sweeney, G. Pétron, G. Frost, R. Michael Hardesty, J. Kofler, B. R. Miller, T. Newberger, S. Wolter, R. Banta, A. Brewer, E. Dlugokencky, P. Lang, S. A. Montzka, R. Schnell, P. Tans, M. Trainer, R. Zamora, and S. Conley, "Methane emissions estimate from airborne measurements over a western United States natural gas field," Geophys. Res. Lett. **40**, 4393–4397 (2013).
35. A. Schliesser, N. Picqué, and T. W. Hänsch, "Mid-infrared frequency combs," Nat. Photonics **6**, 440–449 (2012).
36. F. Adler and S. A. Diddams, "High-power, hybrid Er:fiber/Tm:fiber frequency comb source in the 2 μm wavelength region," Opt. Lett. **37**, 1400–1402 (2012).
37. T. J. Kippenberg, R. Holzwarth, and S. A. Diddams, "Microresonator-based optical frequency combs," Science **332**, 555–559 (2011).
38. A. Hugi, G. Villares, S. Blaser, H. C. Liu, and J. Faist, "Mid-infrared frequency comb based on a quantum cascade laser," Nature **492**, 229–233 (2012).
39. Z. Zhang, T. Gardiner, and D. T. Reid, "Mid-infrared dual-comb spectroscopy with an optical parametric oscillator," Opt. Lett. **38**, 3148–3150 (2013).
40. N. Leindecker, A. Marandi, R. L. Byer, K. L. Vodopyanov, J. Jiang, I. Hartl, M. Fermann, and P. G. Schunemann, "Octave-spanning ultrafast OPO with 2.6–6.1 μm instantaneous bandwidth pumped by femtosecond Tm-fiber laser," Opt. Express **20**, 7046–7053 (2012).
41. A. Ishimaru, *Wave Propagation and Scattering in Random Media* (Academic, 1978).
42. L. C. Sinclair, F. R. Giorgetta, W. C. Swann, E. Baumann, I. Coddington, and N. R. Newbury, "Optical phase noise from atmospheric fluctuations and its impact on optical time-frequency transfer," Phys. Rev. A **89**, 023805 (2014).
43. L. S. Rothman, I. E. Gordon, Y. Babikov, A. Barbe, D. Chris Benner, P. F. Bernath, M. Birk, L. Bizzocchi, V. Boudon, L. R. Brown, A. Campargue, K. Chance, E. A. Cohen, L. H. Coudert, V. M. Devi, B. J. Drouin, A. Fayt, J.-M. Flaud, R. R. Gamache, J. J. Harrison, J.-M. Hartmann, C. Hill, J. T. Hodges, D. Jacquemart, A. Jolly, J. Lamouroux, R. J. Le Roy, G. Li, D. A. Long, O. M. Lyulin, C. J. Mackie, S. T. Massie, S. Mikhailenko, H. S. P. Müller, O. V. Naumenko, A. V. Nikitin, J. Orphal, V. Perevalov, A. Perrin, E. R. Polovtseva, C. Richard, M. A. H. Smith, E. Starikova, K. Sung, S. Tashkun, J. Tennyson, G. C. Toon, V. G. Tyuterev, and G. Wagner, "The HITRAN 2012 molecular spectroscopic database," J. Quant. Spectrosc. Radiat. Transfer **130**, 4–50 (2013).
44. L. S. Rothman, I. E. Gordon, A. Barbe, D. C. Benner, P. E. Bernath, M. Birk, V. Boudon, L. R. Brown, A. Campargue, J. P. Champion, K. Chance, L. H. Coudert, V. Dana, V. M. Devi, S. Fally, J. M. Flaud, R. R. Gamache, A. Goldman, D. Jacquemart, I. Kleiner, N. Lacome, W. J. Lafferty, J. Y. Mandin, S. T. Massie, S. N. Mikhailenko, C. E. Miller, N. Moazzen-Ahmadi, O. V. Naumenko, A. V. Nikitin, J. Orphal, V. I. Perevalov, A. Perrin, A. Predoi-Cross, C. P. Rinsland, M. Rotger, M. Simeckova, M. A. H. Smith, K. Sung, S. A. Tashkun, J. Tennyson, R. A. Toth, A. C. Vandaele, and J. Vander Auwera, "The HITRAN 2008 molecular spectroscopic database," J. Quant. Spectrosc. Radiat. Transfer **110**, 533–572 (2009).
45. J.-M. Hartmann, H. Tran, and G. C. Toon, "Influence of line mixing on the retrievals of atmospheric CO_2 from spectra in the 1.6 and 2.1 μm regions," Atmos. Chem. Phys. **9**, 7303–7312 (2009).
46. V. M. Devi, D. C. Benner, L. R. Brown, C. E. Miller, and R. A. Toth, "Line mixing and speed dependence in CO_2 at 6227.9 cm–1: constrained multispectrum analysis of intensities and line shapes in the 30013 ← 00001 band," J. Mol. Spectrosc. **245**, 52–80 (2007).
47. A. Predoi-Cross, A. R. W. McKellar, D. C. Benner, V. M. Devi, R. R. Gamache, C. E. Miller, R. A. Toth, and L. R. Brown, "Temperature dependences for air-broadened Lorentz half-width and pressure shift coefficients in the 30013 ← 00001 and 30012 ← 00001 bands of CO_2 near 1600 nm," Can. J. Phys. **87**, 517–535 (2009).
48. R. A. Toth, L. R. Brown, C. E. Miller, V. M. Devi, and D. C. Benner, "Spectroscopic database of CO_2," J. Quant. Spectrosc. Radiat. Transfer **109**, 906–921 (2008).
49. G.-W. Truong, K. O. Douglass, S. E. Maxwell, R. D. van Zee, D. F. Plusquellic, J. T. Hodges, and D. A. Long, "Frequency-agile, rapid scanning spectroscopy," Nat. Photonics **7**, 532–534 (2013).
50. D. A. Long, A. Cygan, R. D. van Zee, M. Okumura, C. E. Miller, D. Lisak, and J. T. Hodges, "Frequency-stabilized cavity ring-down spectroscopy," Chem. Phys. Lett. **536**, 1–8 (2012).